Localized surface plasmon and phonon polaritons investigated by mid-infrared spectroscopy and near-field nanoscopy

Abeer Al Mohtar

Thèse
de doctorat
de l'UTT

Abeer AL MOHTAR

Localized Surface Plasmon and Phonon Polaritons Investigated by Mid-infrared Spectroscopy and Near-Field Nanoscopy

Spécialité :
Optique et Nanotechnologies

2015TROY0014 **Année 2015**

Thèse en cotutelle avec l'Université Libanaise - Beyrouth - Liban

Université Libanaise
École Doctorale
Sciences et Technologies

utt
université de technologie
Troyes

THESE

pour l'obtention du grade de

DOCTEUR de l'UNIVERSITE DE TECHNOLOGIE DE TROYES

Spécialité : OPTIQUE ET NANOTECHNOLOGIES

présentée et soutenue par

Abeer AL MOHTAR

le 8 juin 2015

Localized Surface Plasmon and Phonon Polaritons Investigated by Mid-infrared Spectroscopy and Near-Field Nanoscopy

JURY

M. A. BOUHELIER	DIRECTEUR DE RECHERCHE CNRS	Président
M. A. BRUYANT	MAITRE DE CONFERENCES	Directeur de thèse
M. Z. HERRO	ASSOCIATE PROFESSOR	Examinateur
M. M. KAZAN	ASSISTANT PROFESSOR	Examinateur
M. A. KHOURY	FULL PROFESSOR	Directeur de thèse
M. M. TABBAL	FULL PROFESSOR	Rapporteur
M. T. TALIERCIO	PROFESSEUR DES UNIVERSITES	Rapporteur

Thesis to get the degree of a doctor of philosophy

Localized Surface Plasmon and Phonon Polaritons Investigated by Mid-infrared Spectroscopy and Near-field Nanoscopy

Al Mohtar Abeer

8 June 2015

Université de Technologie de Troyes
Laboratoire de Nanotechnologie et Instrumentation Optique (LNIO) and
Ecole Doctorale des Sciences et de la Technologie
Université Libanaise

Contents

1. Introduction

"There is plenty of room at the bottom", The famous Richard Feynman's lecture in 1959 talking about nanoscience and nanotechnology. With his original thinking, he was able to predict that "we will get an enormously great range of properties that substance can have, and of different things that we can do", if we can arrange the atoms and molecules the way we want. However pointing back to Feynman's lecture gives nanotechnology an early date of birth despite the emergence of semiconductor industry at this time. Due to the lack of dedicated nano-characterization tools, the real take-off of nanotechnology dates back to about only 25 years with the idea of Scanning Tunneling Microscopy (STM) and Atomic Force Microscopy (AFM) put in practical use by G. Binnig and H. Rohrer in 1981 rewarding them a Nobel prize for physics in 1986. With the use of piezoelectric elements highly precise scanning was enabled and the door for nanotechnology was wide open.
The 20th century has been called the century of physics where the Quantum Mechanics helped understanding the nature of atoms, molecules and solids state physics while microelectronics industry precipitated the exploitation of semiconductor science and engineering. Integrated circuit, lasers and magnetic disks are of indispensable use in our daily life.
The word "nanostructure" refers to a system with characteristic size in the range of 1-100 nm in a certain dimension. At this scale the intrinsic properties (electrical and thermal conductivities, chemical reactivity,...) are no more rigidly fixed by the material nature and quality but become critically dependent on the structure geometry such as size, shape, and roughness. As new physical properties or resonant behavior can be obtained by scaling down the structures, a huge work is done recently on tailoring and characterizing the properties of such nanostructures. Various applications beyond microelectronics are targeted and notably in optics, like data storage [100], biosensing [18, 138, 8], coherent thermal emission [47], Surface Enhanced Raman Spectroscopy (SERS) [96, 72], Surface-Enhanced Infrared Absorption Spectroscopy (SEIRA) [7, 6, 23],... All the said applications rely on the fact that the electric field could be enhanced greatly by the nanoparticles.

There is no exact theory for describing the field enhancement for irregularly shaped particles; however to grasp the main phenomena let us consider, the optical field enhancement at the surface of a small sphere (sphere diameter much smaller than the illumination wavelength). Based on an electrostatic approach, the enhancement factor, defined as the ratio of the surface field E_{loc} to the far-field illumination E_{in},

is proportional to the polarizability of the small sphere α [42, 24]:

$$\frac{E_{\text{loc}}}{E_{\text{in}}} \propto \alpha \qquad \text{with} \qquad \alpha = 4\pi a^3 \frac{\epsilon_p - \epsilon_m}{\epsilon_p + 2\epsilon_m}$$

Where a denotes the diameter of the particle, ϵ_p is its dielectric function, and ϵ_m is the dielectric function of the surrounding medium. As one can notice, the maximum field enhancement happens at $\text{Re}(\epsilon_p(\omega)) = -2\epsilon_m$, this is referred to as Frohlich resonance frequency. A more detailed calculation show that the Frohlich resonance is shifted depending on the shape of the particle as well as the dielectric function of the surrounding medium.
When the permittivity of the particle satisfies the Frohlich resonance condition, a strong coupling occurs between the surface modes and the illuminating electromagnetic wave. This strong coupling is called surface polariton. Phonons, plasmons, excitons can fulfill this condition:

- Surface plasmon polaritons occur on metal or highly doped semiconductors surfaces. The resonance could happen for all frequencies below a limiting plasma frequency ω_p:

  $$\omega_p = \sqrt{\frac{e^2 N_{\text{eff}}}{\epsilon_o m_{\text{eff}}}}$$

  The physical quantities appearing are N_{eff}, the average electron density in the unit cell, and m_{eff}, the effective mass of the electron, e is the electron charge. This plasma frequency lies in the ultraviolet for some metal and in the visible for others; however it can be largely tuned in highly doped semiconductors, by adjusting the doping level we can go up far infrared wavelengths down to about $5\,\mu m$.
- Surface phonon polaritons occur in polar crystals at frequencies between the longitudinal and transverse phonon resonances, lying in the infrared. Surface phonon polaritons have attracted much less attention than surface plasmon polaritons from the research community, even though their optical resonance can be stronger and sharper because they have weaker damping than surface plasmon polariton [55].
- Surface exciton polaritons occur in semiconductors for frequencies below the fundamental electronic excitation, ranging from the infrared to the ultraviolet depending on the material.

1.1. Overview

In the present work, the surface phonon and plasmon modes in SiC nanostructures were investigated as well as the occurrence of Localized Surface Plasmons Resonances (LSPR) in a grating of highly doped InAsSb on GaSb. After an introduction

on some of the fundamental aspects of this thesis (part I), two approaches were followed in order to study these phenomena:

- Far-field approach to have a collective response from the whole sample (part II);
- Near field approach to study the resonance behavior at the nanoparticle level (part III).

Part II is divided in theoretical part and experimental part. Two theoratical models exploiting the far-field reflectivities are presented in order to obtain information on the effective permittivity of the nanostructured samples. Both methods requires Kramers-Kronig analysis to provide sufficient information, namely the phase of the reflection coefficient. Within the first model, the transfer matrix method was then used to determine the effective dielectric function. This is a suitable method to extract physical properties of a multilayered material without any prior knowledge of its characteristics except for the thickness. The second model is based on a modified Lorentz model for the permittivity with adjustable parameters to fit the complex reflectivity spectra. The crystal is viewed as consisting of coupled damped oscillators, with a damping coefficient function of the frequency and temperature. The anisotropicity is taken into account as well. Although it requires more information on the sample, this approach also provide quantitative information on the damping modification due to the surface structures.

Part III consists in a first chapter describing the methodology developed in this thesis to extract the near-field signal, then the method is applied to the characterization of test samples and the LSPR-sample investigated in part II. The experimental method consists of a novel detection method for extracting the phase and amplitude in interferometry experiments. It is developed, tested and applied on several systems. Then the approach is implemented in a Near-field Scanning Optical Microscope (NSOM) equiped with a Quantum Cascade Laser (QCL) continuously tunable from 10 μm to 10.5 μm. A spectroscopic study is then made on the highly doped semiconductor grating in order to investigate the LSPRs. The probe sample interaction is discussed using simple analytic model and based on Finite Difference Time Domain (FDTD) simulations. The thesis concludes with a summery of the work and future prospectives

Part I.

Fundamental Aspects

2. Phonon and Plasmon Characteristics

In this chapter we give a general introduction about the infrared response of solid materials which is mainly determined by the lattice vibrations (phonon modes) and free charges oscillations (plasmon modes). First, basic ideas about phonons and the characteristics of their harmonic normal modes are given. Then we present the Lorentz equation that models the crystal dielectric function as damped oscillators. The phononic resonant behavior in the infrared region is illustrated compared to that of Localized Surface Plasmons (LSP) in highly doped semiconductors is made. The dielectric function and the dispersion relation for plasmon gas in a bulk material is presented. Then the dispersion relation of surface phonon/plasmon polariton is explained, focusing again on the similarities existing between both types of excitations.

2.1. Phonon Behavior

The importance of understanding the phonon behavior comes from the fact that phonons are responsible for the infrared response in most solids; thus controlling the possible applications in this spectral range. This phonon response is expressed as a function of the wavelength λ by the dielectric function of the material $\epsilon(\lambda)$, that can be determined using infrared spectroscopy. This function strongly depends on material quality indeed; however it can exhibit drastic change if the material is structured at sizes smaller than the phonon mean free path [63]. Obtaining $\epsilon(\lambda)$ is therefore of utmost importance not only for optical application (field-enhancement), but also because impact most of the physical properties of materials; notably their thermal conductivity κ, which is found to be strongly affected and sometimes dramatically reduced by material nano-structuration. Materials with high thermal conductivity are of critical use for heat dissipation in chips for circuit industry [67], but on the other hand materials with low thermal conductivity are good candidates for power-generation applications[1]. In this context, many of the IR spectroscopic investigations of $\epsilon(\lambda)$ are currently performed on nano-structured materials in order

[1]The thermoelectric effect is a well known phenomenon, where the conversion efficiency depends on the dimensionless thermoelectric figure of merit $ZT = (S^2\sigma/\kappa)T$, where S, σ, κ and T are the Seebeck coefficient, electrical conductivity, thermal conductivity, and absolute temperature, respectively[135].

to determine the phonon transport properties, motivated by the application in the renewable energy domain. For both optical and heat transport applications, quantitative study of the phonon harmonicity and anharmonicity in the infrared regime is essential to gain insight into the effect of size on the harmonic and anharmonic terms of the interatomic forces and potentially tailor novel nanoscale devices.

2.1.1. Lattice vibration of an infinite crystal

In order to attain a realistic picture, the assumption that ions in a crystal are fixed to a site of a Bravais lattice has been relaxed long time ago. However it is still assumed that the mean equilibrium position of each ion is a Bravais lattice site R. It is assumed as well that the typical oscillation of each ion, u, about the equilibrium position is small compared to the interionic spacing [13]. We may express the ion position $r(R)$ at any time as:

$$r(R) = R + u(R)$$

Then the dynamic potential energy of the system is:

$$U = \frac{1}{2}\sum_{RR'}\Phi(r(R) - r(R')) = \frac{1}{2}\sum_{RR'}\Phi(R - R' + u(R) - u(R')) \tag{2.1}$$

The Hamiltonian of the system:

$$H = \sum_{R}\frac{P(R)^2}{2M} + U$$

Where $P(R)$ is the momentum of the atom whose equilibrium position is R and M is the atomic mass. Following the assumption that the atoms will not deviate substantially from their equilibrium positions, the potential energy U could be expanded using the three-dimensional form of Taylor's theorem:

$$f(r + a) = f(r) + a.\nabla f(r) + \frac{1}{2}(a.\nabla)^2 f(r) + \frac{1}{3!}(a.\nabla)^3 f(r)$$

Applying this to equation(2.1) with $r = R - R'$ and $a = u(R) - u(R')$. We get at equilibrium, as first non-vanishing correction to the equilibrium potential, the quadratic term:

$$U^{harm} = \frac{1}{2}\sum_{\substack{RR'\\ \mu\nu}} u_\mu(R) D_{\mu\nu}(R - R') u_\nu(R')$$

With

$$D_{\mu\nu}(R - R') = \delta_{R,R'}\sum_{R"}\Phi_{\mu\nu}(R - R") - \Phi_{\mu\nu}(R - R')$$

The harmonic approximation is the basic building block in understanding the lattice dynamics; however the unharmonic terms especially the third and forth terms in the potential energy are needed to explain a lot of physical phenomena. They are considered as first and second perturbation to the Hamiltonian of the system. This will be considered in more detail in chapter 4.

2.1.2. Normal Modes of a Diatomic Lattice

Solving the lattice dynamic equations of motion, upon assuming that only neighboring ions interact, and applying periodic boundary conditions, we obtain the relations of ω, the angular frequency, as function of k, the wavevector. These relation are usually referred to as dispersion relation. The periodic boundary conditions imply there will be N non equivalent values of allowed wavevector k satisfying:

$$k = \frac{n_1}{N_1}b_1 + \frac{n_2}{N_2}b_2 + \frac{n_3}{N_3}b_3, \qquad n_i \text{ integers}$$

Where b_i are the reciprocal lattice vectors, and N_i large integers satisfying $N = N_1N_2N_3$. The allowed wave vector values can be chosen to be in any primitive cell in the reciprocal lattice. This cell is referred to as the first Brillouin zone.

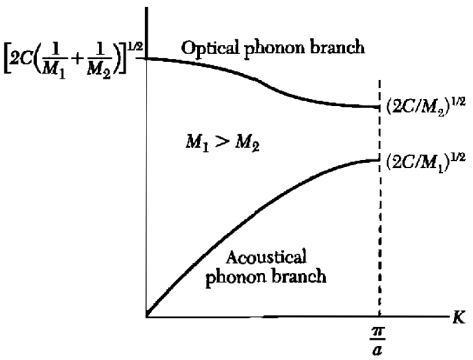

Figure 2.1.: Optical and acoustic branches of the dispersion relation for a diatomic linear lattice, showing the limiting frequencies at k=0 and k=k_{max}=π/a. The lattice constant is a. Taken from "Introduction to Solid State Physics" for C. Kittel [71].

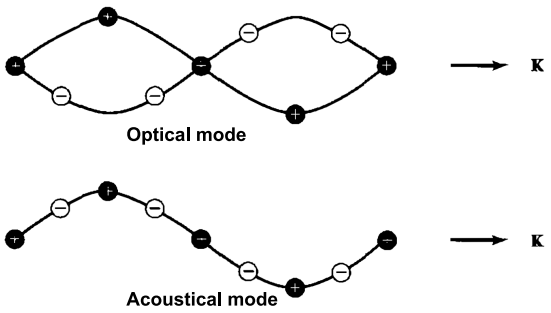

Figure 2.2.: Transverse optical and transverse acoustical waves in a diatomic linear lattice, illustrated by the particle displacements for the two modes at the same wavelength. Taken from "Introduction to Solid State Physics" for C. Kittel [71].

Fig. 2.1 is taken from chapter 4 in the "Introduction to Solid State Physics" for C. Kittel [71]. It shows the dispersion relation of a diatomic lattice with two different-mass ions of masses M_1 and M_2, C being the force constant.

Optical modes are atomic vibrations where two different atoms on the unit cell vibrate out of phase to set up a polarization effect through a dynamical oscillating dipole moment which couples to an external oscillating electric field; thus these modes are responsible for much of the optical behavior of a crystal. They are Infrared active modes. They absorb IR light at their resonance frequencies. The phonon modes can be though of as the lattice degrees of freedom. Lets consider a lattice with p atoms in the primitive cell, then we have $3p$ normal modes: with 3 of these modes acoustic and $3p-3$ optical. These normal modes split into *transversal* optical/acoustical modes or *longitudinal* optical/acoustical modes depending on the displacement of atoms in a direction perpendicular or parallel to the wave propagation respectively. Fig. 2.2 is an illustration of transversal optical and acoustic modes, taken from "Introduction to Solid State Physics" for C. Kittel [71]. Since electromagnetic waves are transverse, photons can only apply driving forces to the transverse vibrations of the crystal. Longitudinal phonons in bulk crystals have no effect since they induce an electric field in a direction perpendicular to that of the light wave. Hence, resonant absorption occurs when the incoming frequency of light ω matches with the TO phonon modes ω_{TO}. However, LO modes do in fact play an important role in the infrared properties of crystals. The photon-phonon coupling occurs by the driving force exerted by the electric field of the incoming light. Therefore, the crystal must have some ionic character for its TO phonons to be IR active.

2.1.3. Light matter interaction

When an electromagnetic wave passes through a polarizable medium it couples to the induced polarizability of the medium. When the effect of the medium is significant we call them hybrid modes, since their properties depend on both the electromagnetic wave and the medium itself. When the acoustic and plasma waves interact with the incident electromagnetic wave we add the postfix "polariton" and they transform from the classic acoustic and plasma waves to "phonon polariton" and "plasma polariton" respectively. We shall later distinguish as well between the bulk plasmon and phonon polariton that propagate in a homogenous medium and the surface plasmon and phonon polariton. Let us consider an external electric field excitation of the form: $\mathbf{E} = E_o \exp(i\omega t)$ applied along the x-axis to a harmonic oscillator representing vibrations of electrons around positively charged ion or phonons:

$$m^* \frac{d^2\mathbf{x}}{dt^2} + m^*\Gamma \frac{d\mathbf{x}}{dt} + \beta\mathbf{x} = -e^*\mathbf{E} \tag{2.2}$$

with $\mathbf{x}$ is the displacement of the oscillator with respect to its equilibrium position, β is the restoring force per unit displacement, Γ is the damping force per unit mass and per unit velocity or the damping constant, m^* and e^* are the reduced

mass and the effective charge respectively. The dipole resonance frequency $\omega_{TO} = \sqrt{(\beta/m^*)}$. Looking for solutions of the form of $x = x_o e^{-i\omega t}$ gives the the displacement amplitude:

$$x_o = \frac{eE_o}{m^*(\omega_{TO}^2 - \omega^2 - i\Gamma\omega)}$$

Recalling that the dipole moment $\mathbf{P}$ induced by the external electric field is $\mathbf{P} = -e^*\mathbf{x}$. The electric displacement, with the appearing physical quantities have their known indications, is:

$$\mathbf{D} = \epsilon_o\mathbf{E} + \epsilon_o\chi\mathbf{E} + \mathbf{P} = \epsilon_o\epsilon_{latt}\mathbf{E}$$

The lattice dielectric function follows:

$$\epsilon_{latt}(\omega) = 1 + \chi + \frac{Ne^2}{m^*\epsilon_o}\frac{1}{(\omega_{TO}^2 - \omega^2 - i\Gamma\omega)}$$

Here N is the number of effective oscillators per unit volume. In order to have the so called Lorentz damped oscillator model, we have to substitute for the high and low frequency limits of the dielectric function. The high-frequency dielectric constant comes from the deeply bound valence electrons whose frequency response is flat in the infrared, its limit is given by:

$$\epsilon_{latt}(\infty) = \epsilon_\infty = 1 + \chi$$

for the low frequency limit,

$$\epsilon_{latt}(0) = \epsilon_{st} = 1 + \chi + \frac{Ne^2}{\mu\epsilon_0}\frac{1}{\omega_{TO}^2}$$

Then we get the well-known Lorentz equation of the lattice dielectric function, in the case of independent damped oscillators:

$$\epsilon_{latt}(\omega) = \epsilon_\infty + \frac{S\omega_{TO}^2}{(\omega_{TO}^2 - \omega^2 - i\Gamma\omega)} \tag{2.3}$$

S represents the oscillator strength, given by $S = \epsilon_{st} - \epsilon_\infty$. In equation (2.3), we see that we have a resonant behavior at $\omega = \omega_{TO}$[2]. For $\epsilon_{latt}(\omega) = 0$ we have

[2]It becomes clear if we consider an ideal case with zero damping.

longitudinal modes at longitudinal optical frequencies ω_{LO}. This condition gives the Lyddane-Sachs-Teller (LST) relation:

$$\frac{\omega_{LO}^2}{\omega_{TO}^2} = \frac{\epsilon_{st}}{\epsilon_\infty}$$

An interesting interpretation of this relation is that when $\epsilon_{st} = \epsilon_\infty$ the LO and TO modes are degenerate and we have no infrared resonance ($S = 0$). This is the case of non-polar crystals such as silicon and germanium.

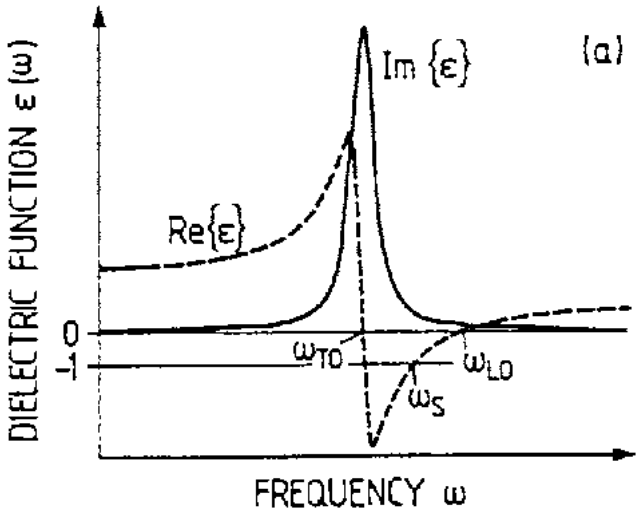

Figure 2.3.: Dielectric functions $\mathrm{Re}\{\epsilon(\omega)\}$ and $\mathrm{Im}\{\epsilon(\omega)\}$ for a harmonic oscillator. In the case of an IR-active crystal, the resonance frequency is the frequency (ω_{TO}) of the transverse optical (TO) bulk phonon; ω_{TO} is the frequency of the longitudinal optical (LO) bulk phonon, ω_S that of the surface phonon polariton (we'll talk about this in the following section). (Adapted from [87])

Fig. 2.3 shows the permittivity as function of the frequency. As can be seen, the region where the real part of the permittivity is negative is comprised between the TO and LO phonon modes resonance. This zone is named reststrahlen band. This region is characterized by high reflection at normal incidence. To summarize the behavior of the dielectric function:

- $\epsilon \rightarrow$ the most positive/negative values[3] $\qquad \omega = \omega_{TO}$.
- $\epsilon = 0 \qquad \omega = \omega_{LO}$
- $\epsilon \rightarrow \epsilon_\infty \qquad \omega \rightarrow \infty$

[3]The moderate negative/positive values corresponds to high damping.

In order to better understand Fig. 2.3, let us recall the dispersion relation of electromagnetic wave propagating in a non-magnetic medium:

$$\mu_o \frac{\partial^2 D}{\partial t^2} = \nabla^2 E$$

Recalling that we are searching solutions having the form:$E \propto \exp(-i\omega t)\exp(ik.r)$ and the displacement $D = \epsilon(\omega, k)E$. Then:

$$k^2 c^2 = \omega^2 \epsilon(\omega) \tag{2.4}$$

A lot of information can be extracted from this relation, for real ω:

- ϵ is real and > 0, k is real and a transverse electromagnetic wave propagates.
- ϵ is real and < 0, k is imaginary, the incident wave does not propagate in the region. We call these waves evanescent waves with characteristic damping length $\frac{1}{|k|}$.
- ϵ is complex, k is complex and the electromagnetic wave is damped.
- $\epsilon = \infty$, in the undamped case, the poles of the $\epsilon(\omega, k)$ dictate the frequencies of the free oscillation of the medium.
- $\epsilon = 0$, this corresponds to longitudinally polarized waves, these waves are possible only at the zeros of ϵ.

2.2. Plasmonics in Bulk and Nanostructured Materials

The unique properties of plasmonics have made them the subject of interest to a lot of researchers recently; in addition to them being simply quite fascinating. Their ability to enhance the electric field made them useful in Surface Enhanced Raman Spectroscopy (SERS), laser antennas and fibers [96, 72, 77] as well as trapping and manipulation of micro/nano-sized particles [110]. The tunability of plasmon resonance coupling enabled the plasmonics for biosensing [133]. The enhanced absorption property of plasmonics helped their integration in controlled drug delivery applications, cancer therapy [49] and microfluidic mixing [94]. The enhanced scattering promoted the use of plasmonics in contrast agent imaging [40]. The confinement in sub-wavelength regime coupling made the application of plasmonics in guiding and manipulation of light possible [90]. The strong field enhancement due to the coupling between the electromagnetic wave and the free carrier oscillations is of great use in the technological field. In this section we'll present Drude model that we will use afterward to determine the dielectric function of the highly doped semiconductor. Then we will talk about the Surface Polaritons and the existing analogy between SPPs and SPhPs.

2.2.1. Bulk plasmon polariton: The Drude model

The most basic description of the electron behavior in a material is modeled by Drude theory. The model, which is an application of kinetic theory, treats classically the electrons in a solid look much like a pinball machine, as detailed in many references [13, 25]. In a lossless isotropic medium in the presence of a current, this free electron gas model gives:

$$\epsilon = 1 - \frac{\omega_p^2}{\omega^2}$$

With ω_p the bulk plasma frequency:

$$\omega_p^2 = \frac{e^2 N_{\text{eff}}}{\epsilon_o m_{\text{eff}}} \tag{2.5}$$

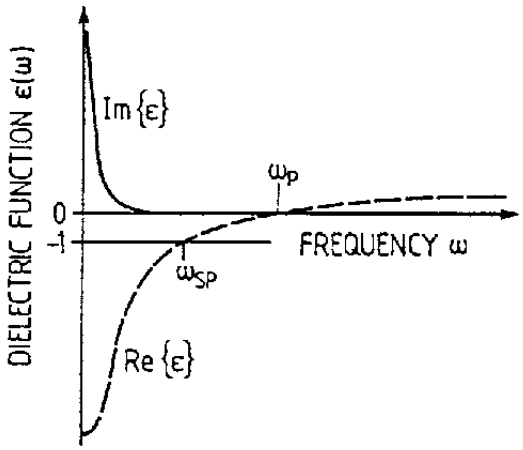

Figure 2.4.: Dielectric function $\text{Re}\{\epsilon(\omega)\}$ and $\text{Im}\{\epsilon(\omega)\}$ for a free electron gas. ω_P is the frequency of the bulk plasmon ω_{SP} is that of the surface plasmon. (Adapted from [87])

The physical quantities appearing are N_{eff}, the average electron density in the unit cell, and m_{eff}, the effective mass of the electron, e is the electron charge. The simple lossless expression of $\epsilon(\omega)$ suppose that the frequency is much higher than the relaxation rate γ_p and has a limited range of validity. It shows however that $\epsilon(\omega)$ becomes highly negative for large wavelength ($\omega < \omega_p$). The unavoidable presence of losses in the complex dielectric function for the free electron oscillators is accounted by considering γ_p:

$$\epsilon(\omega) = 1 - \frac{\omega_p^2}{\omega(\omega + j\gamma_p)} \tag{2.6}$$

Where the relaxation time $\gamma_p = 1/\tau$, and τ is the collision time. Fig. 2.4 is a plot of the dielectric function of a plasmon gas modeled by equation (2.6).

To some extend, the lossless expression is sufficient to describe the general properties of plasmon polariton. It follows from equation (2.4), that if an electromagnetic wave is propagating in such a medium, we'll have this dispersion relation:

$$\omega^2 k_o^2 = \omega^2 k^2 + \omega_p^2 k_o^2 \tag{2.7}$$

The behavior of the plasmon-polariton is more plasmon-like at low frequencies and light-like at high frequencies.

2.2.2. Harmonic oscillator and free electron gas analogy

Plasma waves and acoustic waves interact in a very similar way to an electromagnetic excitation. These similarities are dictated by their similar dielectric functions, that must have the same form if we consider that the restoring force β vanishes. Having a closer look on Fig. 2.3 and Fig. 2.4 we see that actually the plasmon polariton can be seen as a special case of the phonon polariton with:

- $\epsilon_\infty = 1$
- $\omega_{LO} = \omega_p$
- $\omega_{TO} = 0$

2.2.3. Surface Phonon (or Plasmon) Polariton

As light propagates in a medium, the photons interact with other excitations. In fact unless a photon propagates in vacuum, it is usually coupled with other particles such as excitons, phonons or electrons (free or linked). This coupling can produces small or large deviations from the linear dispersion curve $\omega = \hbar k$ with the apparition of low group velocities and even anti-crossings with the dispersion curves of the considered particle. The coupled system particle-photon is then often referred to as polariton to emphasize the existence of a strong coupling, although the notion of polariton can be invoked at some level as soon the photon is embedded in a medium. In electromagnetics, such coupling is described by the dielectric function of the material.

Under some conditions, the polarization wave associated to the polariton can be efficiently confined at the interface between two media. When we deal with free electronic excitations, the surface mode is named surface plasmon polariton (SPP) and it is named surface phonon polariton (SPhP) for phononic excitations. Commonly such modes are also split into two categories: the surface mode localized at the surface of subwavelength particle and the surface modes able to propagate over a distance comparable or bigger than the wavelength.

2.2.4. Plasmonic surface modes

These modes have been known from the work of Sommerfeld in radio wave propagation in 1909, and investigated for optical waves by Fano in 1941 [43]. For a plane interface separating two media (n_1, n_2) in $z = 0$, a surface mode is characterized by an exponential decay of the field on both sides of the surface. Usually an exponential decay is observed in dielectrics when passing from a high to a low refractive index $(n_2 \to n_1 < n_2)$ as shown in Fig. 2.5 a), and three waves are involved in this process: an incident wave, a reflected one and a transmitted (evanescent) one.

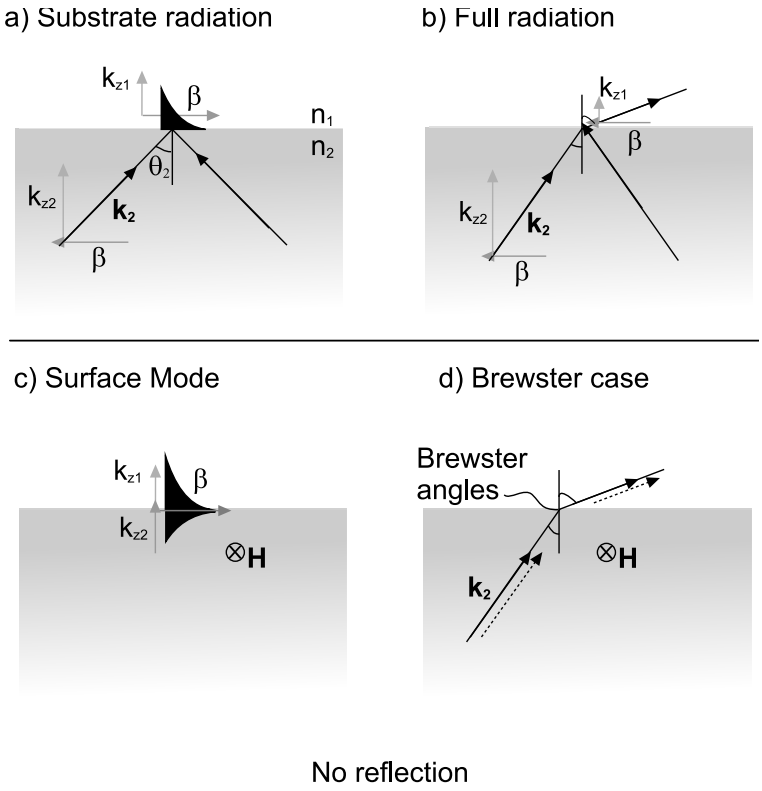

Figure 2.5.: Representation of different modes at the interface: (a) Substrate radiation mode, confined in the upper medium only. (b) Full radiation mode, in the case of a plane wave comming from n_2. (c) Fully confined surface mode. (d) Brewster case, represented in the case of two plane waves propagating in one or the other direction.

Assuming a plane wave illumination from n_2, such exponential decay occurs when the angle from the normal θ_2 is above a critical angle, to prevent the refracted solution represented in Fig. 2.5 b) to exist. In Fig. 2.5 a), the parallel component of the wavevector, which is conserved across a plane interface, exceeds the wavevector value $k_1 = n_1 k_o$ in the low refractive index material. This can be seen from the expression of k_1 as a function of its parallel (β) and vertical (k_{z1}) components given by $k_1 = \sqrt{\beta^2 + k_{z1}^2}$. It is clear that k_{z1} is imaginary for $\beta = n_2 sin\,(\theta_2) > k_1$, leading to an exponential decay of the transmitted plane wave in the z direction.

In the case of the confined mode represented in Fig. 2.5 c), there are two evanescent waves, one in each medium. The situation is therefore analogous to the Brewster incidence represented in Fig. 2.5 d): *there is no reflected wave.*

Inspection of the Fresnel coefficient r shows that a zero reflectivity can only be meet at Brewster angle for TM polarization[4], whatever the impinging field (evanescent

[4]TM polarization: Transverse Magnetic. The magnetic field is perpendicular to the incident plane defined by the incident beam and the surface normal.

or not). The Brewster angle corresponding to zero of r^{TM} in the medium 1 is given from the normal by:

$$\theta_B = \arctan\left(\frac{n_2}{n_1}\right) = \arctan\left(\sqrt{\frac{\epsilon_2}{\epsilon_1}}\right) \tag{2.8}$$

The dispersion relation $\beta(\omega)$ of such mode is then obtained by inserting θ_B in $\beta = k_1 \sin(\theta_B)$. We obtain[5]:

$$\beta = \frac{\omega}{c}\sqrt{\frac{\epsilon_1\epsilon_2}{\epsilon_1+\epsilon_2}} \tag{2.9}$$

This dispersion relation shows that parallel wavector β cannot exceed $k_1 = \frac{\omega}{c}\sqrt{\epsilon_1}$ and $k_2 = \frac{\omega}{c}\sqrt{\epsilon_2}$ if pure dielectrics (real and positive ϵ) are considered; this is the Brewster mode, fully radiating, which is said to be above the "light cones" defined by the plot of $k_1(\omega)$ and $k_2(\omega)$. However, the situation is different if we consider that ϵ_i can have opposite sign: *i.e.* if one of the material has a metallic behavior (negative ϵ)[6]. The same relation shows that large β values and therefore a strong vertical confinement can be reached if $\epsilon_2 \to -\epsilon_1$.

More precisely, comparing equation (2.9) to equation (2.4) we can formally define an interface dielectric function $\epsilon_s(\omega)$:

$$\frac{1}{\epsilon_s(\omega)} = \frac{1}{\epsilon_1(\omega)} + \frac{1}{\epsilon_2(\omega)} \tag{2.10}$$

In the case of bulk phonon equation, the resonance at ω_{TO} results from the pole of the dielectric function. Similarly, the resonant frequency of the interface waves is obtained from the pole of equation (2.10) defining the "effective" dielectric function $\epsilon_s(\omega)$. This results in:

$$\epsilon_1(\omega) = -\epsilon_2(\omega)$$

[5] using the identity: $\sin(\arctan(x)) = \sqrt{\frac{x^2}{1+x^2}}$ and $k_1 = n_1 k_o = \sqrt{\epsilon_1}\frac{\omega}{c}$

[6] In fact, to maintain electric oscillations at the interface of an horizontal surface, the electric field must have a vertical component and change sign across the interface. This can be seen from the continuity of $D_z = \epsilon E_z$. We can note also that the dispersion relation is often derived by writing the two TM fields in the superstrate (region 1) and the substrate (region 2) as two harmonic plane waves with complex wavector components:

$\mathbf{H}(x,z)_{1,2} = A_{1,2}e^{ik_{z_{1,2}}z/}e^{i\beta x}e^{i\omega t}\mathbf{u_y}$, where A_i corresponds to the maximum amplitude. The continuity of this tangential field gives, beside the conservation of β across the interface, an equality for the two amplitudes A_i. The continuity of the tangential component E_x (obtained from $\mathbf{H}$ via the Ampere-Maxwell law $\mathbf{D} = \epsilon\mathbf{E} = \frac{curl(\mathbf{H})}{i\omega}$) then gives the relation $\frac{k_{z1}}{k_{z2}} = -\frac{\epsilon_1}{\epsilon_2}$. The dispersion relation is then obtained by substituting the k_{zi} by $\sqrt{k_i^2 - \beta^2}$

In real systems, where both ϵ_2 and β are complex, this condition becomes $|\epsilon_1 + \epsilon_2| =$ min, moreover the surface mode propagating along an interface has length of $L_x = 1/\mathrm{Im}(\beta)$. The meaning of this condition is discussed nicely in [17]. The surface mode is sustained through the accumulated charges at the boundary between the material with negative permittivity (ϵ_{m1}) and that with positive permittivity (ϵ_{m2}). The negative permittivity condition is met in the reststrahlen region for the phonon case (between $\omega_{TO} < \omega < \omega_{LO}$) and for $0 < \omega < \omega_P$ in the plasmon case. The electric field distribution associated with the surface polariton mode are schematically shown in Fig. 2.6 where ϵ_{m1} has a negative real part and ϵ_{m2} corresponds usually to a slightly dispersive dielectric.

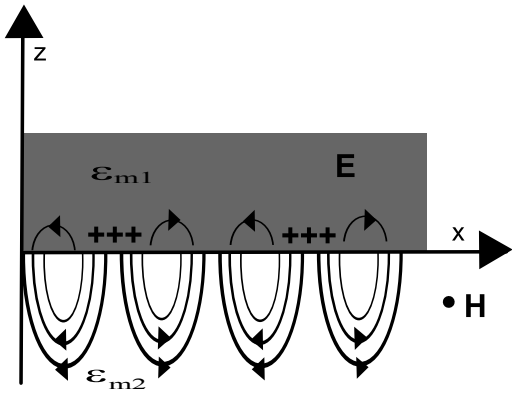

Figure 2.6.: A schematic distribution of the electric field at the boundary between a material with negative relative permittivity (ϵ_{m1}) and a material with positive permittivity (ϵ_{m2}).

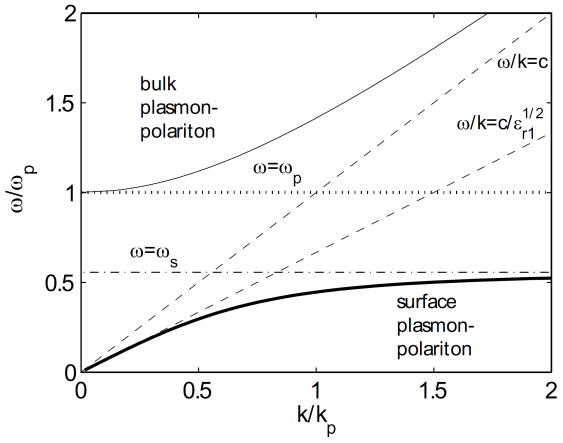

Figure 2.7.: Dispersion of SPPs (solid line) at the boundary vacuum metal. Also shown is the dispersion curve of the bulk mode with ky = kz = 0 (thin solid line), the light line in vacuum and in the dielectric (dashed lines), the dispersions of bulk (dotted line) and surface plasmons (dashed-dotted line)-taken from [121].

To plot the dispersion relation of a plasmon polariton or a phonon polariton the dielectric function must be used. The simplest expression is obtained by considering the lossless expression of the Drude permittivity. If we substitute the dispersion relation for ϵ_1 in equation (2.9) and if we take, for simplicity, ϵ_1=1, we get the following dispersion relation for SPP:

$$\omega^2 = \omega_p^2/2 + c^2\beta^2 \pm \sqrt{\frac{\omega_p^4}{4} + c^4\beta^4} \tag{2.11}$$

Fig. 2.7 is a plot of a similar dispersion relation taken from literature, considering $\epsilon_1 = \epsilon_{r1} > 1$. The solution obtained above the light cone is propagating and

referred to as bulk plasmon polariton and that below the light cone is fully confined and corresponds to the SPP. It can be seen that for low frequencies, SPPs have light-like behavior while at high frequencies they attain a cutoff value ω_s. ω_s is a characteristic value for SPP and equal $\omega_p/\sqrt{1+\epsilon_1}$. The condition to have this surface polariton is[7]:

$$\epsilon_2(\omega) = -\epsilon_1$$

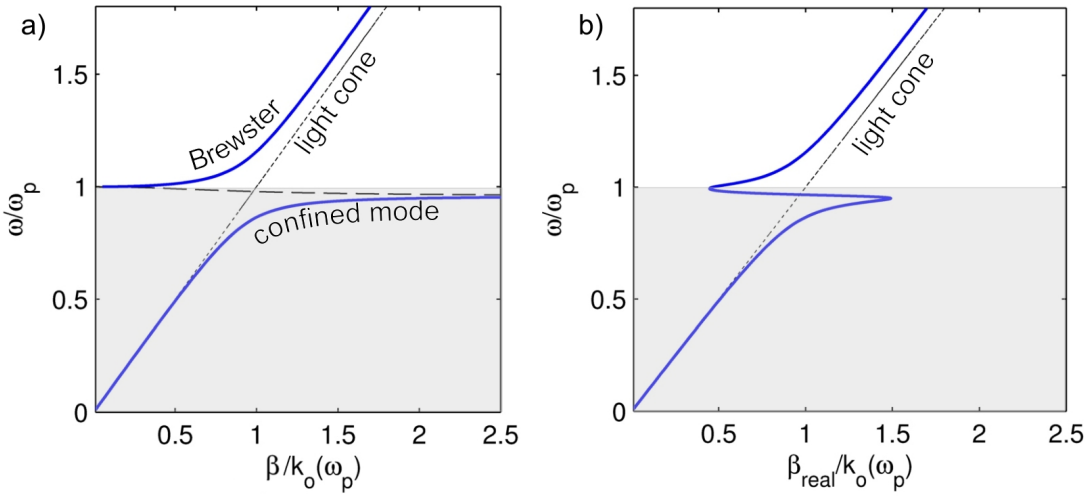

Figure 2.8.: Dispersion relation of the plasmon polariton mode in highly doped InAsSb using Drude model: $\epsilon_{InAsSb}(\omega) = \epsilon_\infty\left(1 - \frac{\omega_p^2}{\omega(\omega+j\gamma_p)}\right)$ with a plasma frequency corresponding to a wavelength of 5.5 µm , $\epsilon_\infty = 11.7$ and $\gamma_p = 10^{13}s^{-1}$. a) The imaginary part of the permittivity ε_2 of the highly doped SC is ignored. The solution between the confined mode and the radiative Brewster mode (dashed) corresponds to purely imaginary values of β and are not considered (purely evanescent modes). b) The complex dielectric function is taken into account. The dispersion relation is plotted as a function of the real part of β.

The analysis of the surface phonon polariton is the same of that of surface plasmon polariton, the only difference is that for the first case we use the dielectric function for a damped Lorentz oscillator while in the latter we use that of a free electron gas (filling the second half space).

In this thesis, both highly doped semiconductors having plasma frequency in the infrared have been considered as well as undoped semiconductor having phonon resonance . The dispersion relations for such material are plotted in Fig. 2.8 and Fig. 2.9 respectively.

[7]In practice, the dielectric function $\epsilon_2(\omega)$ is complex, while ϵ_1 is often dielectric (air). The condition $|\epsilon_1 + \epsilon_2| = \min$ for having a surface polariton is then $real(\epsilon_2(\omega)) = -\epsilon_1 = -1$.

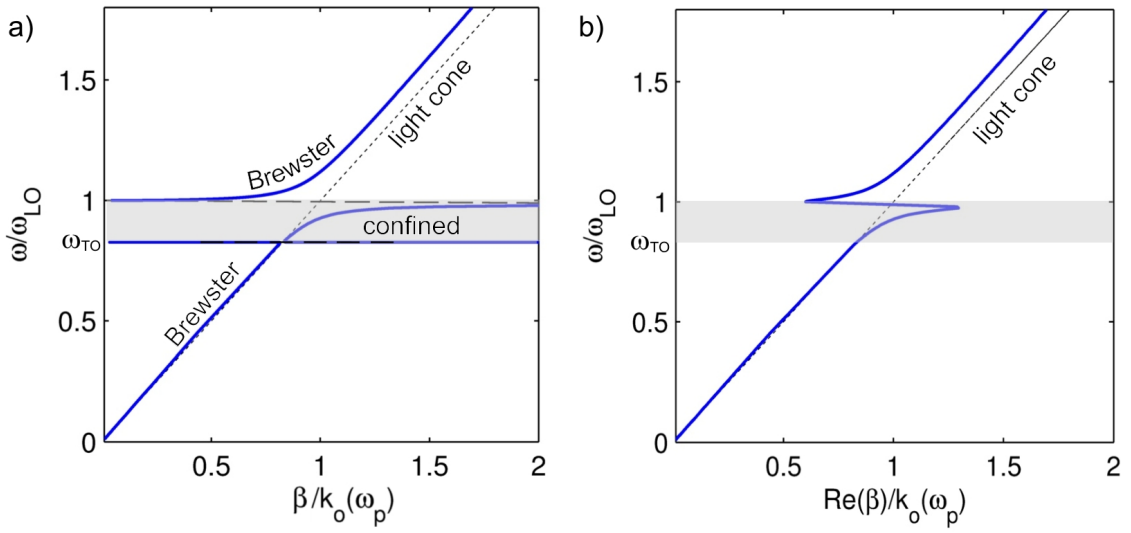

Figure 2.9.: Dispersion relation of the phonon polariton mode in a polar crystal ($\omega_p = \omega_{LO}$) of SiC, using Lorentz oscillator model. a) The imaginary part of the permittivity ε_2 of SiC is ignored: in consequence the TO resonance appears. b) The complex dielectric function is taken into account with large losses at the TO frequency. The dispersion relation is plotted as a function of the real part of β.

We note that while using the dispersion relation with complex permittivities, the dispersion relation change markedly although the main characteristics remain the same. Still, near the plasma frequency we see that the slope of the curve changes which is the sign of a negative phase velocity. We can point out that a similar behavior is obtained for a bulk material with a TO resonance where the permittivity resonance produce such phase velocity change, this analogy will be pursued in the second part of the manuscript. Confined modes also exist in this region but the losses are very strong and these modes are referred to as "quasi-bounded" modes [37].

Mode confined in a slab The mode confined in a metal-like slab can be obtained as previously, i.e by searching for the minimum of reflectivity of the multilayer system. Fig. 2.10 shows the dispersion relation for a system that consists of 1-micron thick layer of highly doped InAsSb over semiconductor GaSb at two interfaces. The first interface is SC/highly doped SC, the second is highly doped SC/ air. Where we see that these are two separate dispersion curves for a relatively thick layer. These two curves will couple as we reduce the thickness.

2.2.5. Localized Surface Plasmon Resonances

Localized surface plasmon resonance (LSPR) is, by definition, an optical phenomena generated by light when it interacts with conductive nanoparticles that are

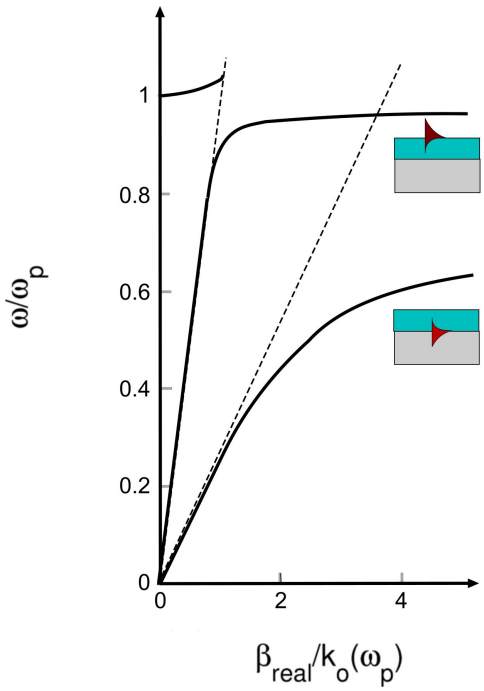

Figure 2.10.: Dispersion relation of the plasmon polariton mode for a slab of highly doped InAsSb using the same Drude parameter as in Fig. 2.9, the substrate is lossless. Here, the imaginary part of the permittivity ε_2 of the highly doped SC is ignored.

smaller than the incident wavelength. In other words, it is the charge density oscillations confined to conductive nanoparticles. The excitation of LSPs at resonance wavelengths results in strong light scattering, in the appearance of intense surface plasmon (SP) absorption bands, and an enhancement of the local electromagnetic fields.

The coherent localized plasmon oscillations have a resonant frequency that depends on the composition, size, geometry, dielectric environment and separation distance of NPs. The origin of LSPR comes from the oscillating electric field that causes coherent oscillation of conduction electrons thus accumulating the polarization charges on the surface of a NP [134, 9]. The optical properties of NPs differ strongly from those for bulk material, if we consider Mie's solution for Maxwell's equations, where only dipole oscillations contribute to the extinction spectrum C_{ext}[8] [103, 134]:

$$C_{ext}(\lambda) = \frac{24\pi^2 R^3 \epsilon_m^{\frac{3}{2}} N}{\lambda \ln(10)} \frac{\epsilon_i(\lambda)}{(\epsilon_r(\lambda) + \chi\epsilon_m)^2 + \epsilon_i^2(\lambda)}$$

Here ϵ_m is the medium dielectric function, $\epsilon = \epsilon_r + i\epsilon_i$ is the complex dielectric function of the material of the NP, R is its radius, N is the density of free carriers.

[8]Extinction spectrum: is the absorption plus elastic light-scattering spectrum

χ is a factor that accounts for the shape of the particle and its aspect ratio, it varies from 2 for a spherical particle to 20 for nanorods [83].

In order to illustrate this more clearly we have made 2D FDTD simulations for geometrically identical nanostructures. The structures geometry is rounded trapezoidal with sub-micron dimensions (see Fig. 2.11); this geometry was chosen to match the up coming experimental studies that were performed in this thesis. In the first case, we used SiC as material for the nanostructures and SiC as substrate, while in the second case we used highly doped InAsSb (doping level $5 \times 10^{19}\text{cm}^{-3}$) for the nanostructures and GaSb as substrate. Fig. 2.11 shows on logarithmic scale the scattered field intensity map:

$$I_{\text{scat}}(x, y) = |\mathbf{E_{scat}}|^2, \text{ with } \mathbf{E_{scat}} = \mathbf{E_{total}} - \mathbf{E_{bg}}$$

The incident Field $\mathbf{E_{bg}}$ corresponds to a plane wave illumination from above, which is subtracted from the total field to obtain the scattered intensity maps. The incident field map is computed in the absence of the nanostructures.

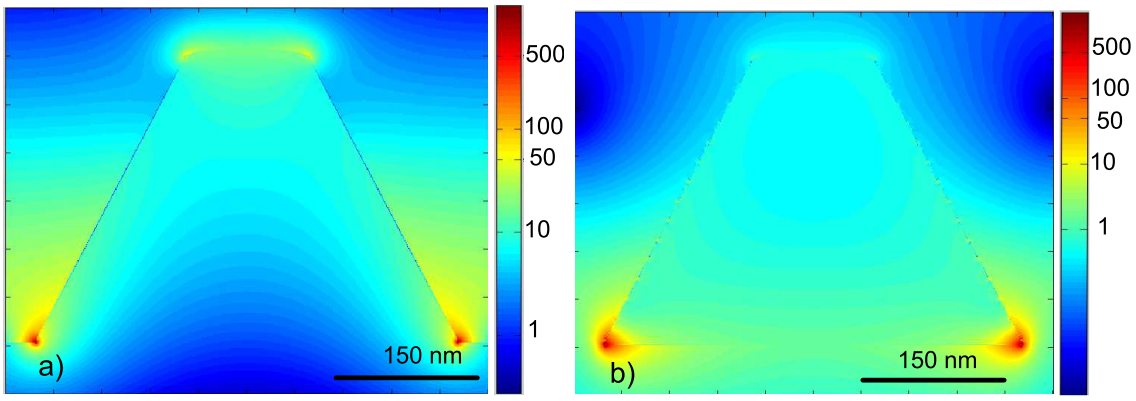

Figure 2.11.: Periodic boundary conditions are set in 2D FDTD simulations, p-polarized plane wave illumination is used. Structures are with base length 430 nm, top length 130 nm and topography of 300 nm. a) SiC nanostructure over SiC at its resoance frequency $\lambda = 10.5\,\mu$m, b) highly doped InAsSb over GaSb at strongest resonace ($\lambda = 13.57\,\mu$m).

Fig. 2.11 a) presents the scattered electric field intensity in the case of SiC, this structure exhibits a sharp resonant behavior at wavelength of 10.5 μm. The image is shown at the resonance frequency, for a polarization along horizontal x direction. A strong field enhancement is occurring at the bottom and top of the structure. This happens when the real dielectric function is slightly negative, about -1 in this case, with a weak imaginary part equal to 0.2. A similar behavior is remarked for the second case, highly doped InAsSb on GaSb, Fig. 2.11 b). Where we see very strong confined field enhancement, localized at the intersection between the highly doped semiconductor and the semiconductor. For this structure we see three sharp resonance wavelengths at: 8.79 μm, 10.24 μm, 13.57 μm. The shown image in

Fig. 2.11 b) is taken for the strongest peak, which is at 8.79 μm. The real dielectric function at the resonance wavelengths is more negative than the previous case where it is -17.6 for the first resonance wavelength, -28 for the second and -59 for the last. The imaginary part is more pronounced where it is equal to 1.4 for the first resonance, 2.19 for the second and 5.1 for the last. This could explain that for the same structure the plasmonic resonance is strong however the phononic resonance is sharper. Studying these two cases covers the whole field of application in the infrared regime.

2.3. Summary

In this chapter we have presented the basic principles of phonon behavior and the laws dictating the surface phonons. We discussed the role of phonons and free carriers in the response of a material to an electromagnetic excitation. We talked about bulk plasmons and surface plasmons. We introduced the origin of SPRs and similarities they exhibit SPhRs. We have discussed the LSPRs phenomena and the differences between the bulk and NP plasmon resonances. In short, this chapter provided the basic concepts behind the phenomena we will be investigating in this work.

3. Characterization Tools

This chapter is dedicated to present a brief background about the characterization techniques used; in the far-field and near-field interaction regime.

3.1. Far-field Characterization Tool

In order to investigate the optical properties of the studied samples we have used the far-field approach to gain access to knowing the collective response of the material. Fourier Transform Infrared Reflectivity (FTIR) is an anciently known nondestructive optical characterization tool [28, 44]. In principle, IR spectroscopy is based on a Michelson interferometer working with a very broadband optical source. It allows the detection of infrared absorption and reflection properties over a broad spectral range, giving information about the vibrations between the bonds of the atoms making up the material; thus resulting in an infrared absorption spectrum that is like a molecular "fingerprint" of the sample, since each different material is a unique combination of atoms. Therefore, infrared spectroscopy is a very reliable technique for several types of qualitative analysis to examine intrinsic and extrinsic properties of semiconductor thin films. One of the advantages of FTIR spectroscopy is the use of the interferometer that results in fast measurements. Because all the frequencies are measured simultaneously, most FTIR measurements are made in a matter of seconds. Besides, the signal-to-noise ratio (SNR) is proportional to the measurement time and the number of scans.

However the reflectivity spectra obtained through FTIR are only imperfect signatures of the considered material because the phase information giving the lag between reflected and incident fields is missing. For example, considering a normal reflectivity spectrum on a semi-infinite medium characterized by a complex refractive index n, the reflectivity in the air is given by the well known relation:

$$r = \frac{n-1}{n+1}$$

It appears clearly that the complex value of r must be determined to evaluate the complex dielectric function $\epsilon = n^2$.

A first step in the analysis of FTIR measurement is then to determine the phase information from the amplitude response $R = |r|^2$. Such analysis can be performed

with Kramers-Kronig relations. In order to extract quantitative information embedded in the dielectric function of the material, the obtained complex reflectivity can then be compared with physical models able to fit the FTIR spectrum. For this purpose two models have been developed at the American University of Beirut by the research group of prof. Michel Kazan. These models have been considered and used in this work.

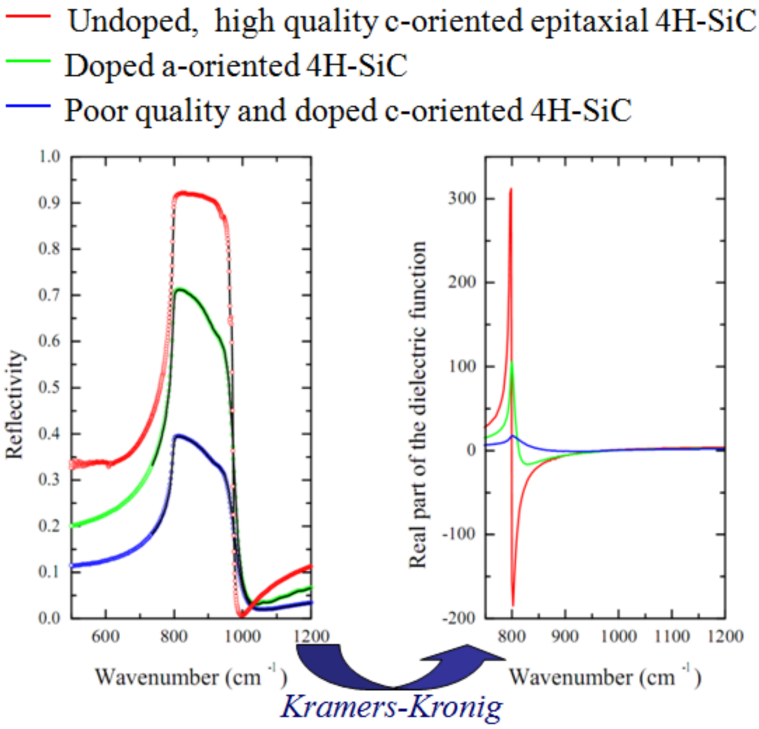

Figure 3.1.: Reflectivity and dielectric function of three samples of 4H-SiC versus wavenumber [117].

Fig. 3.1 illustrates the efficiency of the first model where the reflectivity spectra of SiC were fitted based on a physical model of the permittivity. This enables the accurate determination of the permittivity function that contains information about the crystalline quality of the material as well as the free carrier concentration. This is held through measuring the reflectivity spectra of three samples made of 4H-SiC versus wavenumber [117]. The difference between the three samples is their quality, orientation and doping. It is important to point out that this analysis was conducted in the infrared regime where we are sensitive to the phonon response that is affected by the crystalline quality and point defects. The dielectric function of samples versus the frequency calculated by the Kramers-Kronig relations, is shown in Fig. 3.1 b), from which we can conclude that in the visible range, the dielectric function of all the three samples is the same; but in the mid-IR range there is a big modification.

The principles of these models as well as other models that were used/developed for far-field analysis will be further discussed in chapter 4.

3.2. Near-field Characterization Tool

While far-field spectroscopic tools such as FTIR are highly valuable, they typically suffer from a limited spatial resolution preventing the local analysis of the dielectric function. In other word only average or effective values of ϵ can be directly determined which is problematic when submicronic structures are investigated. The near-field approach was followed so that the study the optical properties of each nanostructures individually is enabled.

Near-field Scanning Optical Microscopy (NSOM) is a unique tool to investigate surface waves. Its high spatial resolution as well as its ability to detect the localized surface modes made it the best choice to investigate the localized surface plasmon resonances as well as the phonon modes. In order to have a more practical and fast NSOM images with optimum signal to noise ratio, we have developed a new detection method that will be discussed in chapter 6. In this section, we provide a historical background of the idea of NSOM and its development. Then we talk about its types and the common used detection methods.

3.2.1. A Historical Overview

The idea of NSOM dates back to 1928, where it was proposed by Synge [124] that it is possible to surpass Abbe diffraction limit [1]. He thought of its feasibility via a tiny, local illumination of the sample. He proposed to do this through a small aperture (small compared to the wavelength) inside a screen, thus any collected light should originate from the specific illuminated region of the sample. Or following Babinet's principle of complementary screens, instead of a hole in an opaque screen we can put a scatterer [61]. This brilliant idea stayed unproven experimentally till about 50 years later due to technical difficulties. Since during that period it was hard to manufacture a nanometric-sized hole and it was ever harder to bring a nano-scatterer close enough to the sample.

The first result on overstepping the diffraction limit was reported by Ash and Nicholls in 1972 [12]. They were able to achieve a resolution of $\lambda/60$ by using microwave radiation ($\lambda = 3$ cm) with aperture size $a = \lambda/20 = 1.5$ mm. The real NSOM experimental application was not enabled until 1984 with the advent of STM [22, 21]. The discovery of piezoelectric material allowed nanometric control of the sample-scatterer/aperture distance. This drastically improved the scanning precision; since then results on beating the diffraction limit in the visible regime were reported [80, 105]. Later on several major improvements were made including tip modulation in order to suppress the background light [58, 139]. The first reported results of NSOM operating in the mid-IR (10.6 μm) was in 1996, where a resolution of 17 nm was claimed [76]. It was then understood that the resolution of NSOM does not depend on the wavelength but rather on the diameter of the used tip. It took long before understanding the basic physics of the the near-field interaction

and how to interpret NSOM images notably due to the presence of artifacts related to the sample topography [52]. Nowadays, with the increased interest in surface waves and high resolution optical microscopy, NSOM is a demanded characterization technique entering into an industrial area with the emergence of companies manufacturing commercial NSOM [84, 45, 46, 128]. Three major interests include: the eigenmode imaging of plasmonic or photonic stuctures (waveguides, dielectric and metal resonators) [26, 113], local infrared spectroscopy [104] and raman spectroscopy [123].

3.2.2. NSOM Types

Since the idea of NSOM has emerged, researchers thought of its applicability in different modes. Some groups applied the principle of NSOM through an aperture (applying the idea of a hole in a screen). It is typically based on tapered optical fibers with or without metal coating. This type of near-field microscopy was historically the first to appear. Other groups replaced the hole by a scatterer in other words instead of an aperture they used a tip. The latter type usually referred to as apertureless or scattering-type Scanning Near-field Optical Microscopy, sSNOM or aSNOM. The third type of NSOM is the hybrid one, where a tip is deposited besides having an aperture. In this section, we will give head-lines about the advantages and inconveniences of each type.

3.2.2.1. Aperture NSOM

The main principle of aperture NSOM is illustrated in Fig. 3.2. Usually this type of NSOM is achieved by using optical fibers with or without metal coating [20]. Fig. 3.2 d) shows a metal coated, aperture probe manufactured by Focus Ion Beam taken from [36]. This type of NSOM operates via different modes:

- Illumination mode, Fig. 3.2 a): Where light is transmitted through the fiber and the extremity of the fiber works as nano-source [95].
- Collection mode, Fig. 3.2 b): The sample is illuminated from the far-field and the scattered near-field is collected by the fiber [19].
- Simultaneous illumination and collection mode, Fig. 3.2 c): Where the same probe is used to illuminate and collect the scattered signal [57].

The sample in this type of NSOM is illuminated very locally; thus, the imaging is essentially background-free, which makes the aperture probes excellently suited for imaging low-intensity objects like biological samples. One of the inconveniences is that it is difficult to fabricate reproducible aperture probes. However, the major drawback of aperture NSOM is the poor resolution. It is well known that NSOM resolution is dictated by the diameter of the aperture (or tip). However the aperture size is limited by two parameters. The first parameter is the skin depth of

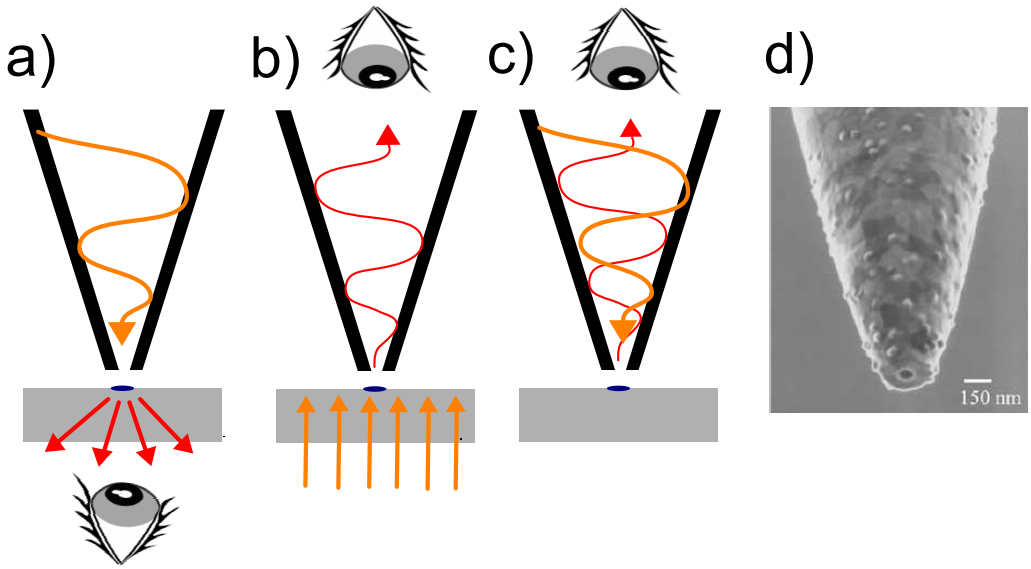

Figure 3.2.: Modes in aperture SNOM: a) illumination mode, b) collection mode and c) similtanous illumination and collection mode. d) SEM images of metal coated, aperture probe manufactured by Focus Ion Beam. Taken from [36].

the used metal coating, where the aperture diameter should be at least twice the material skin depth; because the light is extremely attenuated in the proximity of metal. The second limiting parameter is the transmission efficiency; as apertures are made smaller, the efficiency worsens [97]. Suggestions were made on alleviating this problem by engineering the nanoaperture, so we find shapes such as bowtie-antenna-shaped apertures [129] or C-shaped apertures [92]. Moreover careful cutting of the fiber probe may result in extraordinary transmission offering an improved coupling through the aperture [38], and specfic aperture shapes offer a way to detect more selectively a field component.

3.2.2.2. Apertureless/Scattering NSOM

This type of NSOM was first proposed by H.K. Wickramasinghe in 1994 [139], where a scattering tip is used as a nano-antenna re-emitting in far-field part of the local optical power. The nano-tip typically consists in an AFM probe locally interacting with the sample. Several illumination/collection modes are of course possible. Examples are shown in Fig. 3.3. The first two modes Fig. 3.3 a) and Fig. 3.3 b) correspond to reflection back-scattering mode while the mode Fig. 3.3 c) can be used in transmission mode. The transmission illumination type can be compatible with the use of high numerical aperture objective lens which reduces the so called “background” problem [89] discussed later in this section; however image interpretation can be difficult since light is already modified by the sample before being scattered by the the probe. This type is recommended for thin transparent samples.

In our setup we have used the side illumination as shown in Fig. 3.3 a) with the backward-scattered light collection, where the alignment require a fine focus adjustment.

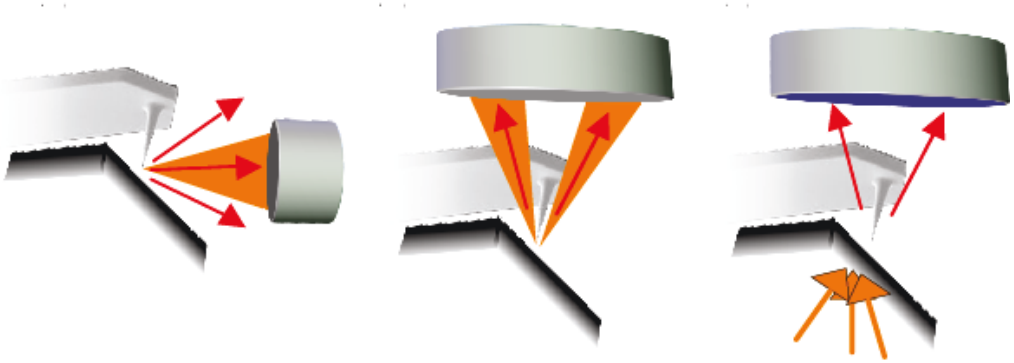

Figure 3.3.: Illumination types, a) Side illumination, b) Top illumination, c) Illumination through the sample in transmission mode.

A description of the probe-sample interaction and the nature of the measured signal in this mode is described in [114] and is given in appendix (Appendix B) .

Usually Scattering type NSOM is based on Scanning Probe Microscope [15], either an AFM [53] or STM [132]. Here the key issue of maintaining nanometric distance between the tip and the sample is addressed. This type of NSOM is robust and provides good topographic and optical resolution.

The resolution of NSOM depends on the diameter of the probe[1], so we have tendency to use sharp tips with very small diameter; however using a small probe means small scattered signal as well. The properties of the used tip are crucial in NSOM. The most used tips are the commercial Si and silicon nitride (Si_3N_4) tips. Some groups use metal coated dielectric tips in order to enhance the scattered signal [41]. Some other groups use metallic tips such as tungsten, silver, gold and platinum. A lot of groups tried to enhance the signal while maintaining small tip diameter through the deposition of a metal sphere on the top of a dielectric tip or by using fluorescent probes. A whole discussion of the probes used in NSOM and their fabrication processes can be found in this review [41].

In the present work we have used tungsten tips fabricated by electrochemical etching since they provide good electric field enhancement in the mid-IR as well as mechanical hardness. Compared to commercial cantilevered probe the body of the probe is much smaller due to the elongated shape. This represents a real advantage as we are not interested in the response of the probe body but only its extremity.

[1]The notion of optical resolution in NSOM differs from the definitions found in classical microscopy (typically given by the numerical aperture of the objective lens). The reason is that the imaging process in NSOM results from a probe-sample interaction which is, by definition, probe and sample dependent. However the evanescent field produced by a decananometric have an extension which is typically in the order or a bit smaller than the tip diameter.

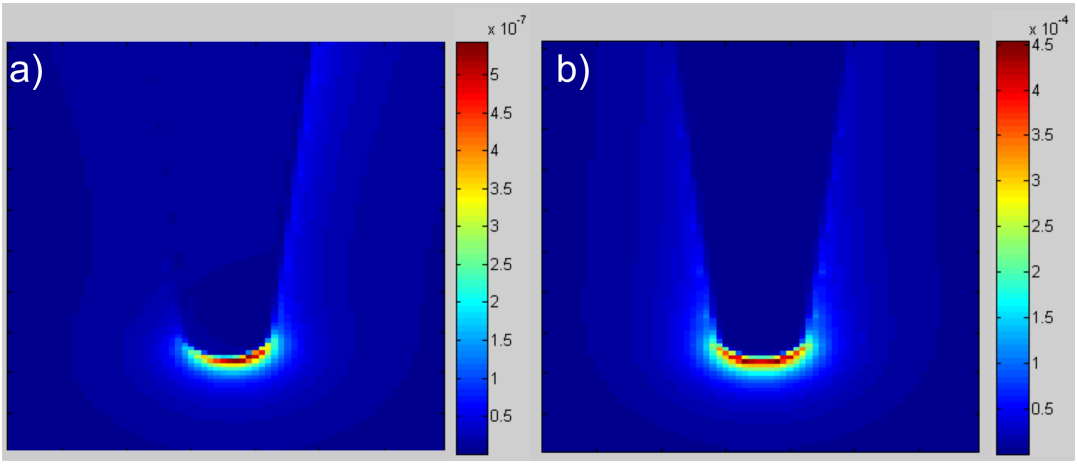

Figure 3.4.: Tip field enhancement at $\lambda = 10\,\mu$m, a) Si tip, b) Tungsten tip.

Fig. 3.4 presents 3D FDTD calculation of field enhancement intensity for two tips, Silicon tip Fig. 3.4 a) and Tunsten tip Fig. 3.4 b) of radii 10 nm, illuminated by a plane-wave of wavelength 10 μm at an angle of incidence of 45^o (in order to imitate our setup). As we can notice the field enhancement intensity for a tungsten tip is about three orders of magnitude more intense than that of silicon; moreover the field is more localized. More details on the probe fabrication and properties are given in chapter 7.

The major advantages of apertureless NSOM are the topographical precision, robustness and high resolution. One of the major drawbacks is the high "background". The "background" represents the field which is not back-scattered by the probe apex but by the sample itself or the probe body. Since the collection of the field scattered by the point-like probe happens in the far-field, we are subject to high background coming from the whole, diffraction-limited, detection spot. In order to address this issue, usually the scanning is made in tapping mode so that the useful scattered signal is modulated at the tip frequency. The measured signal is then demodulated at the tip frequency to recover the signal related to the probe. Such approach is necessary but is not sufficient to cancel out the background: even if the collected background is not modulated by the tip apex, it interferes on the detector with the collected signal field from the probe which is modulated. However, specific interferometric techniques can be implemented to help in strongly filtering out the background light. The interferometric techniques, their advantages and use will be the subject of the following section.

For groups working with commercial Si tips with cantilevers, a major background is coming from the tip shaft. In these configuration the tip oscillation is in the order of 20 nm or more. In order to address this problem these groups demodulate the collected signal at higher tip's harmonic frequencies (Demodulation of the signal at nΩ with n>2, where Ω is the tip angular oscillation frequency) [54, 14]. The technique is based on the fact that the background field has mainly a linear spatial

variation so it modulated at the first harmonic only while the non linear near-field interaction variation is spread over more tip frequency harmonics. The problem with this technique is that we lose part of the useful signal and the NSOM struggles already with low signal. The way this problem was addressed in discussed in section.

3.2.2.3. Hybrid-probe NSOM

To combine the advantages of aperture and apertureless technique, few hybrid-probes have been proposed [91, 68]. An example of hybrid-probe developed at the University of Troyes [116] is shown in Fig. 3.5. It is called hybrid probe since it is a hybridization between a tip and an aperture. The idea of this type of NSOM came for the sake of benefiting from the almost background-free aperture-type NSOM and in the same time having the topographic and optical resolution of aperture type NSOM . In this approach, a metallic nanorod (or carbon nano-tip Fig. 3.5b) is positioned next to the edge of the aperture of a standard aperture probe. This antenna ameliorates the topography as well as the scattering efficiency. The intense near-field spots at the nanorod tip that are created this way are used for imaging.

The general drawback is that the small aperture used to illuminated the nanotip (or to detect) adds an unavoidable additional transfer function [108]. Also, as for aperture probe, the aperture probe material will restrains the spectral bandwidth and should be probably avoided for broadband spectroscopy imaging. In the present context of mid-IR NSOM, the use of hybrid probe where a scattering tip is mounted on an aperture probe is particularly difficult to implement. Indeed, fibered aperture probe made of transparent IR material are really uncommon although single mode IR fibers are now commercially available.

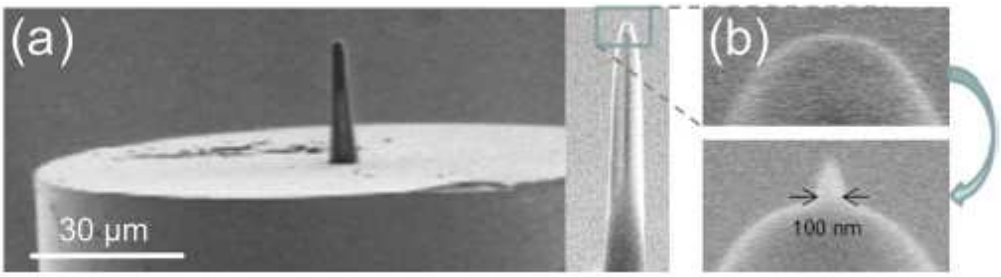

Figure 3.5.: a) Example of polymer-tipped optical fiber. b) SEM images of the probe apex without and with a carbon nanoprobe. Taken from [116].

3.2.3. Common Detection Methods

NSOM main challenges are the low scattered signal and the high background. Interferometric setups were implemented in order to enhance the near-field signal as

well as to help filtering out the unwanted background signal. The major used interferometric setups are the heterodyne and pseudo-heterodyne. These setups main advantage is separating the near-field optical amplitude and phase. Like for FTIR measurements, more information about the sample can be retrieved with the phase information. In this work we have developed a new detection method, that we call Generalized Lock-In Amplifier detection method (GLIA). It provides phase and amplitude information with optimum signal to noise ratio. It will be discussed in detail in chapter 6.

3.2.3.1. Homodyne Detection Method

In interferometry, the term homodyne means that only one optical frequency is used in the interferometer. Such interferometric setup can then referred to the "natural" scattering-type NSOM which is intrinsically interferometric without any additional splitter or mirrors. As we mentioned the collected background field $\mathbf{E}_{\mathrm{bg}}$ interferes with the collected signal field $\mathbf{E}_{\mathrm{scat}}$ coming from the probe. Therefore the phase information of the tip-scattered field is coded in the detected signal in presence of a background field. This can be understood by considering the expression of a two-field interference intensity:

$$I = |E_{\mathrm{scat}}|^2 + |E_{\mathrm{bg}}|^2 + 2\,|E_{\mathrm{scat}}|\,|E_{bg}|\cos(\Delta\omega t + \Phi_{bg} - \Phi_{\mathrm{scat}})$$

which is similar to that produced on detector by the two collected fields.

However such basic setups are not desirable as the background is not a "clean" reference field. The background field is not controlled in amplitude and polarization and it will usually vary as the sample is scanned. Thus we can not have information about the phase of the scattered field.

Homodyne detection sometimes refers to NSOM embedded in one arm of an interferometer without phase or frequency shifter in the reference arm. Basically, the setup is then a Michelson interferometer with the NSOM scattered signal at the place of one mirror; thus the phase between the scattered signal and the reference signal depends on the optical path length difference only.

3.2.3.2. Heterodyne Detection Method

This detection method was first exploited by Hillenbrand and Keilmann in 2000 [53]. The main principle is presented in Fig. 3.6 a). In this setup we shift the reference frequency by a small frequency $\Delta\omega$ then upon interfering with the near-field signal we have what is called "beating phenomena", corresponding to a sine modulation in time of the detected intensity. The interference intensity:

$$I = |E_{\mathrm{scat}}|^2 + |E_{\mathrm{ref}}|^2 + 2\,|E_{\mathrm{scat}}|\,|E_{\mathrm{ref}}|\cos(\Delta\omega t + \Phi_{\mathrm{ref}} - \Phi_{\mathrm{scat}})$$

E_{scat} still denotes the collected electric field scattered by the probe, E_{ref} is the reference electric field, Φ_{ref} is the phase introduced by the reference mirror (it is

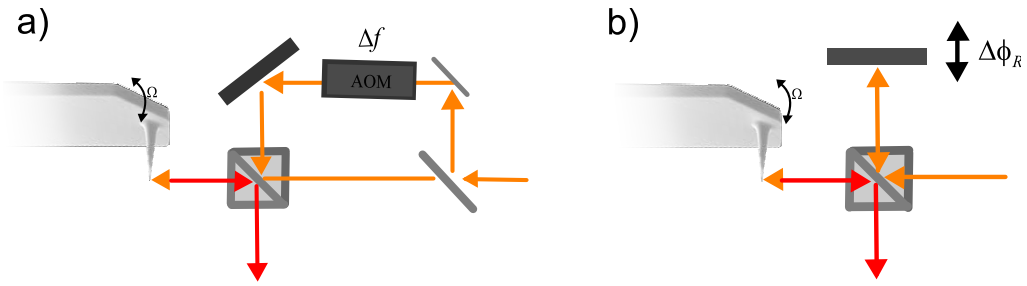

Figure 3.6.: Schematic sketches of common detection methods in NSOM, a) Heterodyne detection method, b) Pseudo-heterodyne detection method.

constant, equal to 0 in the case of equal arms Michelson interferometer), Φ_{scat} is the unknown phase of the scattered signal. Detecting the signal at the beating frequency $\Delta\omega$ using lock-in amplifier we can have direct information about the phase and the amplitude of the scattered field with good signal to noise ratio.

The real situation is a bit more complex if we consider that a background field E_{bg} exists in addition to E_{scat} and E_{ref}. As already mentioned, it is then necessary to work in tapping mode at an angular frequency Ω. Then, the scattered field amplitude will be modulated at Ω and possibly at higher harmonics $n\Omega$. If we look back in the previous expression for I corresponding to the intensity term describing the interference between the two fields (E_{scat}, E_{ref}) , we see that the modulated amplitude $|E_{scat}|$ will act as a carrier frequency shifting the information from $\Delta\omega$ to $n\Omega \pm \Delta\omega$. So, in practice the demodulation is performed at one of the two frequencies $n\Omega \pm \Delta\omega$. A simple analysis of the other interference terms (E_{scat}, E_{bg}) and (E_{scat}, E_{bg}), where E_{bg} is supposed to be unmodulated shows that E_{bg} does not contribute to any signal at the frequency $n\Omega \pm \Delta\omega$. Therefore, this approach very satisfactorily suppress the contribution of unmodulated background light.

This method works well, however it is restricted in term of spectral bandwidth, since it necessitates the usage of Acoustic-Optical-Modulators (AOM) that are often expensive and not available over a large spectral range. In addition, the implementation of AOM is not really possible in the interesting Michelson configuration which is generally more stable than a Mach-Zehnder configuration. These issues are solved using a pseudo-heterodyne method.

3.2.3.3. Pseudo-Heterodyne Detection Method

In this method instead of shifting the frequency of the reference arm, the phase is being shifted as function of time. Fig. 3.6 b) is a schematic of the main principle of this method. Because a phase modulation can be described as a Doppler frequency modulation, such methods are often referred to as pseudo-heterodyne although this term was initially used to describe a detection scheme where the optical source itself is swept in frequency [59, 33] or in phase [70] in unbalanced interferometers.

This concept has been applied to NSOM by Ocelic et al. in 2006 [101], where the reference mirror is mounted on a piezoelectric material and driven by a sinusoidal signal. We have $\Phi_{\text{ref}} = a\sin(\omega_M t)$, where ω is the frequency of the signal driving the piezoelectric. The main advantage of this method is it allows distinguishing between the amplitude and phase of the complex near-field signal over the whole spectral range (mostly used visible and mid-infrared).

The drawback of this method is that the sinusoidal phase variation of the reference phase signal creates several harmonics in the detected signal[2]; thus we either have to do individual lock-in detections at each harmonic or we lose a part of the useful signal. In order to address this issue GLIA has been developed and implemented in this work [4]. The detailed explanation of the method and its practical implementation is given in chapter 6.

3.3. Summary

In this chapter, we presented the characterization techniques used in this work, with an emphasis on the advantages of detecting the signal phase both in far-field and near-field approach. We went through the basic principles, history, types and detection methods in Near-field Scanning Optical Microscopy since it is a relatively new technique; where a lot of research and improvements have been conducted lately.

[2]Instead of an interferometric term like $|E_{\text{scat}}|\,|E_{\text{ref}}|\cos(\Delta\omega\text{t}+\Phi_{\text{ref}}\text{-}\Phi_{\text{scat}})$ with $\Phi_{\text{ref}} = cte$ in the expression of I, we now have $|E_{\text{scat}}|\,|E_{\text{ref}}|\cos(\Phi_{\text{ref}} - \Phi_{\text{scat}})$ with $\Phi_{\text{ref}} = a\sin(\omega t)$. This generates frequency components at ω but also at higher harmonics especially a is large.

Part II.

Far-field Analysis

4. Developed Methods

Far-field analysis was conducted in this work in order to determine the collective response of an array of nanostructures; to have a clear macroscopic view. This study is split into two parts. The first part deals with a two-layer systems. This approach involves the use of Kramers-Kronig relations to determine the complex part of the measured real part of Fresnel reflection coefficient of the system. The properties of the top layer is determined by Transfer Matrix Method (TMM), where the precise properties of the substrate is known. We have made use of this method to characterize a sub-wavelength grating of highly doped semiconductor (considered as an effective layer), Fig. 4.1 a) depicts the approach. The advantage of this approach is that we can determine the properties of the top layer without any prior knowledge of its optical properties. This is particularly useful in the case of strong coupling between resonant structures, where simple theories fails to predict its behavior. In the second part, we treat slightly corrugated substrates. The corrugation was made through the introduction of nano-pillars in a polar crystal of SiC. We need to consider that these nanopillars modify the phonon spectrum through creating new hybrid modes; this is illustrated in Fig. 4.1 b). A model for the dielectric function with adjustable parameters was used to fit the reflectivity spectrum so that we can have quantitative information. This approach is applicable when the corrugated surface change the underlying substrate and cannot be treated separately as an effective layer. In this chapter a brief description of these two approaches is presented.

4.1. Why Considering Nanostructured Surfaces?

In the approach of Fig. 4.1 b), we will study the effect of nanostucturing the surface on the phonon behavior. Since the phonons are responsible for the infrared response and account for the transmission of sound and heat, controlling their properties is of quite importance. Beside optics, the major interests are making use of natural heat to induce electricity, thermally isolate buildings/reduce environmental noise...The second application comes as a consequence of controlling the sound waves by engineering the material bandgap through phononic crystals [75, 118]. These are artificial periodic structures of two elastic materials. However the first application is more tricky because usually while trying to decrease the thermal conductivity of the material, the amelioration of the figure of merit is hindered by unwanted decrease of the electrical conductivity. One of the interesting recent work [34] to avoid this problem was made on introducing pillars on the surface so it will couple with the

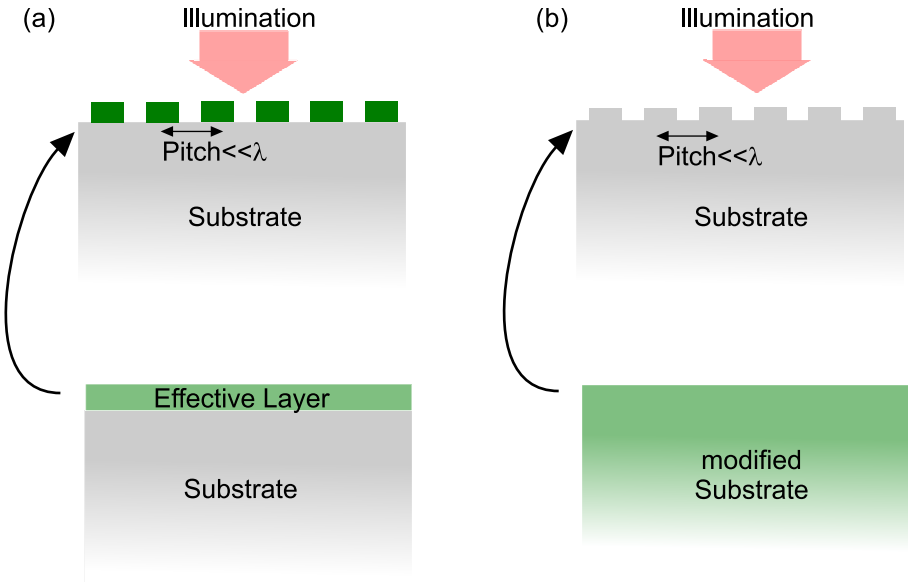

Figure 4.1.: Determination of the infrared response of nanostructures following two approaches: a) TMM based approach, b) a model for the permittivity with adjustable parameters to fit the new reflectivity

underlying atomic-level phonon. This will create new channels for the phonon decay process without actually affecting the electrical conductivity.

In the approach of Fig. 4.1 b), no change in the underlying substrate is invoked which is found to be correct in many situation. Here, we will investigate the plasmonic response in a sub-wavelength grating of highly doped semiconductor on a lattice-matched semiconductor. In general, metals are the most used materials for plasmonics; this is subject to several drawbacks. The major drawback is that the plasma resonance frequency is a property of the material, and there is no available metals whose resonance is in the near or mid-IR regime (1-10 μm), where molecules exhibit marked signatures. Another related drawback of the usage of plasmonics in metals is the huge losses in the mid-infrared regime caused by their large negative permittivity values [79]. Since mid-IR range is quite interesting regime for a lot of applications especially in detection and sensing [122], the study of plasmonics in highly doped semiconductors is recently gaining momentum. One of the biggest advantages of using plasmonics in highly doped semiconductors is the tunablity of the resonance frequency over a very large spectral range [48, 81] in the mid-IR via the doping level, and there is little doubt that plasmonics in metal-free systems will impact all the previously mentioned applications.

4.2. Kramers Kronig Method

For both methods (a) and (b), Kramers Kronig (KK) method was used as a first step following the FTIR reflectivity measurement. Such approach is used to study the phonon behavior and charge carriers related properties in semiconductor materials [32, 140, 65]. Experimentally, we determine the intensity of the reflected field $R = R(\omega)$; however in order to retrieve the full information about a system we should know the phase as well. The KK conversion technique was employed to deduce the phase θ of the reflection amplitude $\rho = \sqrt{R}$ as in reference [109]. The relations are based on the Cauchy's residue theorem for complex integration and often used to calculate the imaginary part of response functions in physical systems from the imaginary part of the response, and vice versa. The theoretical aspects of KK relations are discussed elsewhere [62, 107]. However, as a result, for any function $\alpha(s)$ with real and imaginary parts $\alpha_1(s)$ and $\alpha_2(s)$ respectively, the KK relation is given by:

$$\alpha_1(\omega) = \frac{2}{\pi} P \int_0^{+\infty} \frac{s\alpha_2(s)}{s^2 - \omega^2} ds$$

$$\alpha_2(\omega) = \frac{-2\omega}{\pi} P \int_0^{+\infty} \frac{\alpha_1(s)}{s^2 - \omega^2} ds$$

P denotes the Cauchy principal part of the integral[1]. The application of Kramers-Kronig relations requires some conditions to be satisfied, fortunately the reflectivity function meets these conditions [109]. It is imperative to point out that these KK relations involve an integration from 0 to infinity. However it is experimentally impossible to do that, so it is highly recommended to have the wider spectrum possible to reduce errors. To minimize the error due to the the finite spectral range, we have to extrapolate at the limits. For this purpose a fit with 5 Lorentzians was made at each extremity for each measurement. To apply KK, the Fresnel reflection coefficient is written in the following form:

$$r(\omega) = \frac{E_{\text{ref}}}{E_{\text{inc}}} = \rho(\omega)\exp(i\theta(\omega)) \rightarrow \ln r = \ln(\rho) + j\theta \tag{4.1}$$

Where our measured reflectivity is:

$$R(\omega) = rr^* = \rho^2$$

Then the missing phase $\theta(\omega)$ can be obtained using:

$$\theta(\omega) = -\frac{1}{2} P \int_0^{\infty} \ln\frac{|\Omega + \omega|}{|\Omega - \omega|} \frac{d}{d\Omega}[\ln R(\Omega)] d\Omega \tag{4.2}$$

[1] This is the limit for $\delta \rightarrow 0$ of the sum of the integrals over $-\infty < s < \omega - \delta$ and $\omega + \delta < s < \infty$ [85].

Then, as already briefly mentioned, the complex reflectivity enables the determination of the complex optical constant via:

$$r(\omega) = \frac{n + jk - 1}{n + jk + 1} \tag{4.3}$$

in the case of a normal incidence where n is the refractive index k is the extinction coefficients. The relations between, n, k, the real and imaginary parts of the dielectric functions are as follows:

$$\epsilon_1 = n^2(\omega) - k^2(\omega)$$
$$\epsilon_2 = 2nk$$

So careful application of the Kramers Kronig conversion of the unpolarized reflectivity spectrum enables getting the experimental complex dielectric function.

4.2.1. Kramers Kronig method demonstration

In order to validate the KK approach, the method was numerically tested on semi-infinite Drude metal with a refractive index n_l. The Drude model parameters corresponding to the available highly doped semiconductor of InAsSb was used with doping level of $5 \times 10^{19}\,\mathrm{cm}^{-3}$. Second, the reflectivity from a homogenous substrate of index of refraction n_l was calculated using a FDTD[2] solver. Fig. 4.2 shows the reflectivity determined by FDTD along with that obtained by using the formula[3] $R = \left|\frac{\sqrt{\epsilon}-1}{\sqrt{\epsilon}+1}\right|^2$.

The complex reflectivity then has been calculated using equation (4.2), where from the simulated $\rho = \sqrt{(R)}$ we obtain θ [4]. The obtained real and imaginary parts of the index of refraction (from equation (4.3)) are plotted along with the real implemented ones in Fig. 4.3 and Fig. 4.4 respectively.

A good agreement is observed especially in our region of interest which is above the plasma frequency in the mid-infrared. However a small, constant correction factor of about -0.01 rad is added to the obtained phase of the reflectivity to obtain the best agreement. One reason causing the discrepancies is that, as mentioned previously, the integration of the used equation (4.2) goes from zero to infinity.

[2]FDTD: Finite Difference Time Domain. FDTD refers to a well known electromagnetic simulation method able to solve Maxwell's equations in their time-dependant partial differential form [50, 125].

[3]The FDTD simulation is not necessary here as the reflectivity is analytic. However, for the more complex structures that will be considered, there is no simple analytic form, and FDTD was used alone or together with another other simulation method.

[4]For this purpose, the spectrum is fitted on both extremities of the spectrum and extrapolated, and the Fresnel reflection coefficient is written in the form: $\ln r = \ln(\rho) + j\theta$, as it was highlighted previously.

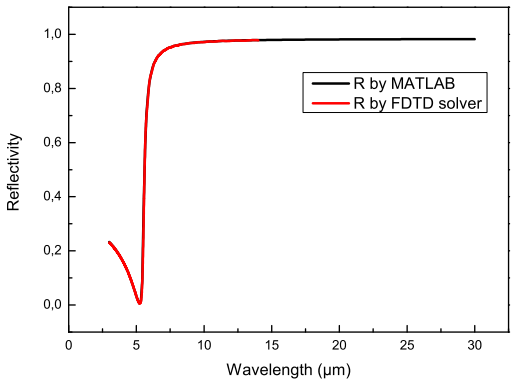

Figure 4.2.: Numerical (FDTD) and analytical reflectivity obtained for a homogenous layer of InAsSb at doping level of $5 \times 10^{19}\text{cm}^{-3}$.

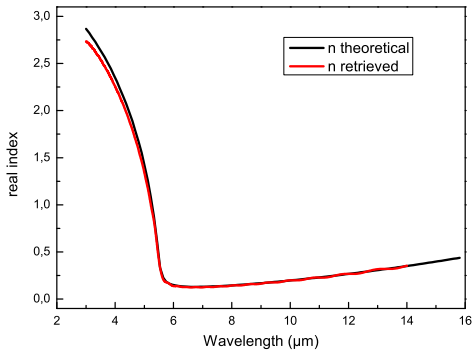

Figure 4.3.: The calculated real part of the index of refraction along with the real one.

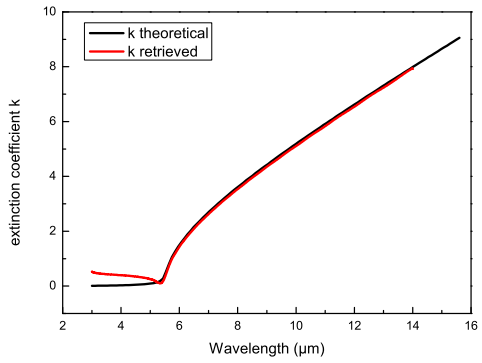

Figure 4.4.: The calculated complex part of the index of refraction along with the real one.

Indeed, it is experimentally impossible to measure R over the wavelengths. So extrapolation at the extremities has been performed. The most accurate region is in the middle of spectrum where the impact of extrapolation is least. Even if the reflectivity stabilizes at the end so no strong variation in R to contribute to the integral; reasonably small errors are present on our calculations. As long a simulation is concerned the spectrum limit can of course be extented, but we can note also that the employed expression for the medium permittivity (Drude model), does not rigorously follow KK as explained [106] and that correction should be added to make it KK compatible. This problem do not exist with a Damped Lorentz Oscillator (DLO) dispersion which is causal without correction.

4.3. Transfer Matrix Model

This model is used to determine the phenomenological LSPR properties in nanostructed array of highly doped semiconductor. It is used in order to obtain quantitative information from complex infrared response without any physical assumption. In order to study the plasmon coupling between the structures and to determine the plasmon modes, a simple Transfer Matrix Method (TMM) was implemented. This model is used to determine the effective dielectric function of a sub-wavelength grating of highly doped semiconductor. We consider the { highly doped InAsSb lines + air } system forms a layer with an effective index of refraction n_l, and this complex index is varied until we recover the experimental complex reflectivity.

Here we used the TMM, which is designed to deal with the propagation of electromagnetic waves in a layered medium. It is based on boundary continuity conditions of Maxwell's equations. In practice, the reflection of light when crossing the interface between two media is described simply by the Fresnel's equations. The TMM method utilizes a simple matrix operation to relate the electric fields which enables handling of a multiple-layer-sample simply and elegantly. This can be found in many textbooks such as [51, 137]. However for clarity it is presented briefly in appendix (Appendix A). We proceed with an illustration of the implementation of TMM in the case of our sample.

In a multilayer system a suitable notation is appreciated to indicate the medium of propagation, wave direction as well as the polarization; here we follow the notation used in [51]. Fig. 4.5 presents a schematic of light propagation through our system. In order to differentiate between mediums and light propagation direction, we denoted the positive and negative light traveling direction. The subscripts 0, l, 2 denote light propagation in medium 0 with index of refraction n_0 (air), medium 1 (effective medium of InAsSb+air with index of refraction $n_l = n + jk$) medium 2 (GaSb, semi-infinite[5]) with complex index of refraction n_t respectively. Fresnel reflectivity and transmission coefficients are denoted by r and t respectively.

The effective Fresnel reflection coefficient:

$$r = \frac{E_0^+}{E_0^-} = A + jB \tag{4.4}$$

Further more, Snell's law has been used to relate the angles of reflection and transmission to that of incidence:

$$n_0 \sin\theta_0 = n_1 \sin\theta_1 = n_2 \sin\theta_2 \tag{4.5}$$

[5]This is quite reasonable since our substrate thickness is$\ggg$ than the penetration depth of infrared excitation.

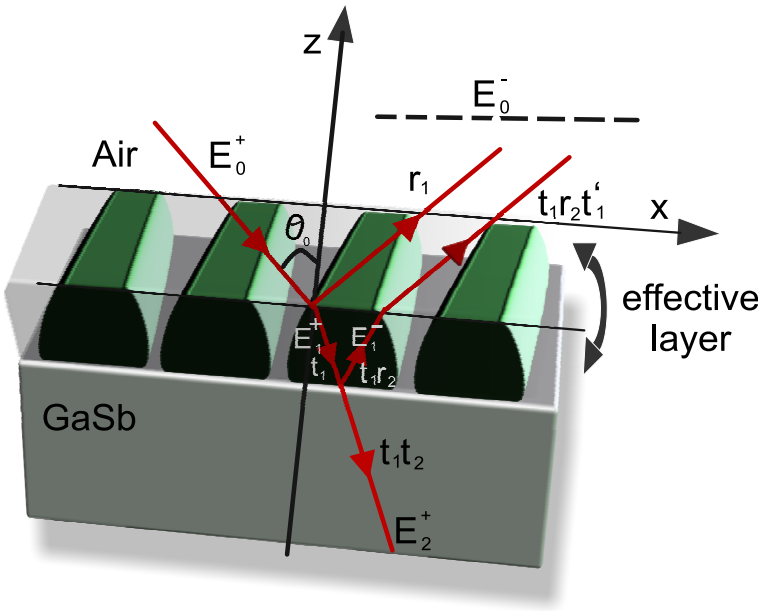

Figure 4.5.: Reflection and transmission at interfaces of our sample. Considering the highly doped semiconductor grating as "effective layer"

Then the substitute equation (4.5) in equation (4.4), leads to a complex expression of Fresnel reflection coefficient as function of the refraction index of medium 0 (air), the incidence angle θ_0, the thickness of the film d (which is usually known), the complex refraction of the film n_1 and the index of refraction of the substrate n_2. The point is to be able to find the complex refraction index of the film n_l. For this purpose we did FTIR measurements so that we get experimentally the reflectivity R and consequently $\rho = \sqrt{R}$ and then we use Kramers-Kronig method discussed in section (sec. 4.2) to determine the complex part θ of Fresnel reflection coefficient given in equation (4.1). As a summary we equate the real and complex parts of Fresnel coefficient given in equation (4.4) to be equal to the real and imaginary parts of Fresnel coefficient given in equation (4.1) respectively:

$$A - \rho \cos\theta = 0 \tag{4.6}$$
$$B - \rho \sin\theta = 0 \tag{4.7}$$

In A and B the only unknown parameters are the properties of the thin film, $n_1 = n + ik$. We end up having two equations with two unknowns. However their dependence is complicated to be solved analytically so a numerical code was developed.

Computational code: We input the fixed/known parameters in the code namely:

- Angle of incidence θ_0

- Index of refraction for air n_0
- The wavelength range λ
- The thickness of the film d_1
- Reflectance values, R, ρ and θ
- The complex refraction index of the substrate, usually if it is known we can use values found in literature; however for more precise measurements it is highly recommended to measure the reflectivity on the substrate alone and use the model discussed in section (sec. 4.5) to get all the information about the substrate.

Then in order to get the complex index of refraction of the film, we give a range of values for both n and k. For example, from $n_{\min} = 0.01$ to $n_{\max} = 30$ with a step of $(n_{\max} - n_{\min})/600$. We search for the set $N_1 = n_1 + k_1$ that satisfies equation (4.6) and $N_2 = n_2 + k_2$ that satisfies equation (4.7). Then we apply the condition that the difference between $N_1$and N_2 must be zero or close to zero. The step that we impose specifies the precision as well as the computational time required.

4.3.1. Slab reflectivity: simple comparison

In order to verify the accuracy of the TMM that we have developed and assess its validity several demonstration tests were performed. As a first test, we have chosen the simplest case where a straightforward comparison between the simulated results and the theoretically expected ones is possible. We have used a 1-micron homogenous layer of highly doped InAsSb (doping level of $5 \times 10^{19}\text{cm}^{-3}$) on GaSb substrate. In the following sections the same level of doping was used as well as the GaSb substrate. The used substrate is GaSb complex dielectric function is taken from literature [2]. The reflectivity of the system is calculated using a commercial-grade simulator based on the finite-difference time-domain method "Lumerical" [86], reflectivity shown in Fig. 4.6. The highly doped InAsSb complex dielectric function fed to the FDTD electromagnetic solver was obtained by Drude model (section (sec. 2.2.1)) through:

$$\epsilon = \epsilon_\infty - \frac{\omega_p^2}{i\gamma\omega + \omega^2}$$

with the following parameters:

- The high frequency dielectric limit: $\varepsilon_\infty = 11.7$
- Plasma wavelength: $\lambda_p = 5.5\,\mu\text{m}$
- Scattering rate: $\gamma = 1 \times 10^{13}\,\text{rad/s}$

The complex part of the reflectivity was then obtained using Kramers-Kronig technique. We have used the TMM described in sec. 4.3 to retrieve the complex index

of refraction of the layer. Fig. 4.7 shows the obtained index of refraction along with the extinction coefficient compared to the real implemented ones obtained by Drude model.

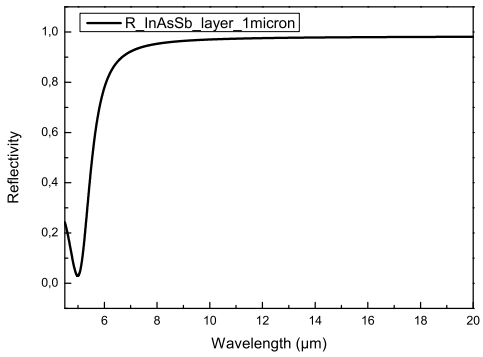

Figure 4.6.: Reflectivity of the system made of 1 micron of highly doped InAsSb over GaSb, calculated by a FDTD electromagnetic solver.

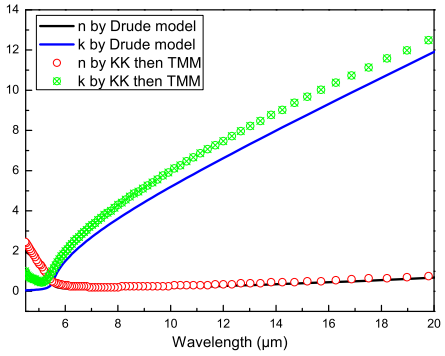

Figure 4.7.: Real and imaginary parts of the index of refraction calculated by TMM along with the implemented ones calculated by Drude model.

A satisfactory agreement is obtained despite the noticed discrepancies. These discrepancies are supposed to be related not only to the limit extrapolation, but also to the usage of Kramers Kronig model with a non-causal material (the absolute Drude permittivity endlessly increases with small frequency). This introduces errors on the calculated values especially at the extremities. Mostly, the value of k is a bit overestimated which is common in KK approach. However we are able to retrieve the basic features, and such problem should disappear in the resonant structure where resonant, DLO-like behavior is observed .

4.3.2. Rectangular nanostructures array response

In this section we used periodic rectangular structures of highly doped InAsSb on GaSb substrate. The idea behind choosing this type of structures is to have nanostructures so that we can see the plasmon coupling or the LPSRs and in the same time having an object with reduced symmetry. Moreover, having simple geometry allows the investigation of the behavior of the effective permittivity in the case of single strong LSPR, instead of multiple peaks. The structures have a width of 426 nm, topography of 120 nm, 540 nm pitch with periodic boundary conditions. Fig. 4.8 a) depicts the adopted system of rectangular structures over the GaSb substrate. Fig. 4.8 b) presents the calculated complex Fresnel coefficient. The numerical calculation was made using FMM[6] also known as rigorous coupled wave analysis (RCWA),

[6]FMM: Fourier Modal method

which is a model to solve rigorously Maxwell equations in the frequency domain. It is based on the Fourier series expansions of the dielectric function and the electromagnetic field [11, 29]. The same results were reproduced using Lumerical FDTD and KK relations[7].

Then the TMM was applied in order to obtain the effective index of refraction of the top layer. A reminder is that an effective layer of the nanostructures and air is assumed, which is chosen to be the topographical height. The input to our code consists of the thickness of the top layer. The complex index of refraction of the substrate as well as that of the air, in addition to the angle of incidence and the polarization[8]. Fig. 4.9 a) shows the real part of the effective permittivity Fig. 4.9 b) presents its complex part, calculated using the obtained real refraction index, n, and the extinction coefficient, k following:

$$\epsilon = \frac{1}{\mu}(n + ik)^2 \approx (n + ik)^2$$

Upon considering $\mu \approx 1$[9]. The verification of our procedure was validated through back calculating the reflectivity. In Fig. 4.9 c) we see the quite satisfactory agreement between the reflectivity and the back calculated reflectivity, obtained with the retrieved complex index of refraction values.

Once we have accurate representation of the dielectric function we can determine all the properties of the material; thus the way it behaves. It is particularly interesting to point out the similar behavior of the dielectric function shown in Fig. 4.9 to that shown in Fig. 2.3 for phonons in polar crystal. Where, in both, we see the real part of the dielectric function becomes negative while the complex part is still weak permitting having a strong resonance. The strong analogy between the effective permittivity of LSPR system and dielectric resonances is pointed out in recent studies such as [93].

In order to clearly show the TO and LO like resonance, it is useful to introduce the two "loss functions" often used in thin films analysis and expressed in detail in [127]. The first one is called "TO energy loss function":

$$\text{TO energy loss function}(\omega) = \text{Im}(\epsilon(\omega)) \tag{4.8}$$

The maxima of this function corresponds to the resonance frequencies of TO vibrations. Fig. 4.9 b) represents this function where we see one dominant resonance

[7] RCWA was used to cross compare the result of FDTD computation, but it also provides the phase of the reflection coefficient more straightforwardly.

[8] However here we are at normal incidence so we have equivalent Fresnel reflection coefficients for both s and p polarization.

[9] Considering $\mu = 1$ is not a rigorous approach since even if we started with a non-magnetic material the structuration may introduce some magnetic behavior; however the variation of μ is expected to be small for the investigated structures, that were not designed to produce a magnetic resonance related to a current loop (as in some thick metallic nano-rings for example [120]).

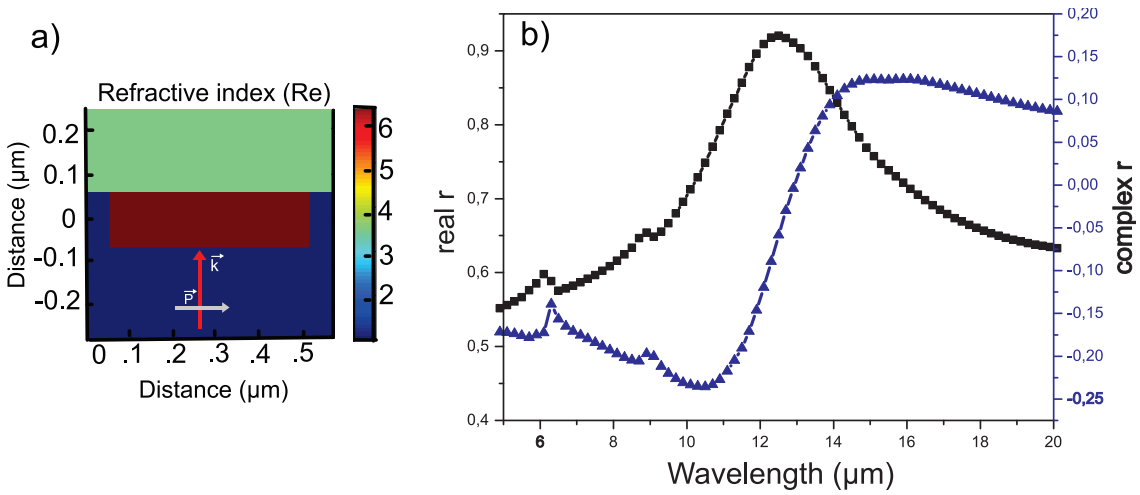

Figure 4.8.: a) Adopted structures of highly doped InAsSb on GaSb. b) Complex Fresnel reflection coefficient calculated by RCWA.

corresponding to a maximum in the reflectivity spectrum. Another quantity that is defined known as "LO energy loss function":

$$\text{LO energy loss function}(\omega) = \text{Im}(-\frac{1}{\epsilon(\omega)}) = \frac{\epsilon^{"}(\omega)}{\epsilon'^{2}(\omega) + \epsilon^{"2}(\omega)} \tag{4.9}$$

Where $\epsilon^{'}(\omega)$ and $\epsilon^{"}(\omega)$ are the real and imaginary parts of the permittivity respectively. By definition, the maxima of this function occur at the resonance frequencies of the LO vibrations of the medium. Fig. 4.9 d) shows this loss function, where we see two resonance frequencies in the vicinity of the plasma frequency of the doped material of our structures $\omega_p = 5.5$ μm. We notice that we have a minimum in the reflectivity in the vicinity of ω_{LO}, while we have a maximum close to ω_{TO}.

4.3.3. More realistic picture

A second more sophisticated test was made. Trapezoidal structures with rounded edges as shown in Fig. 4.10, were built numerically with an InAsSb material at same doping level. Periodic boundary conditions in the electromagnetic solver were imposed. The pitch of the system is 540 nm. This geometry was selected because it gives the closest resemblance with the shape of the experimental ribbons to be studied. The

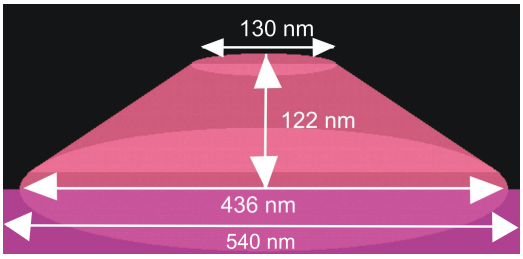

Figure 4.10.: Schematic of the built nanostructures made of highly doped InAsSb on GaSb

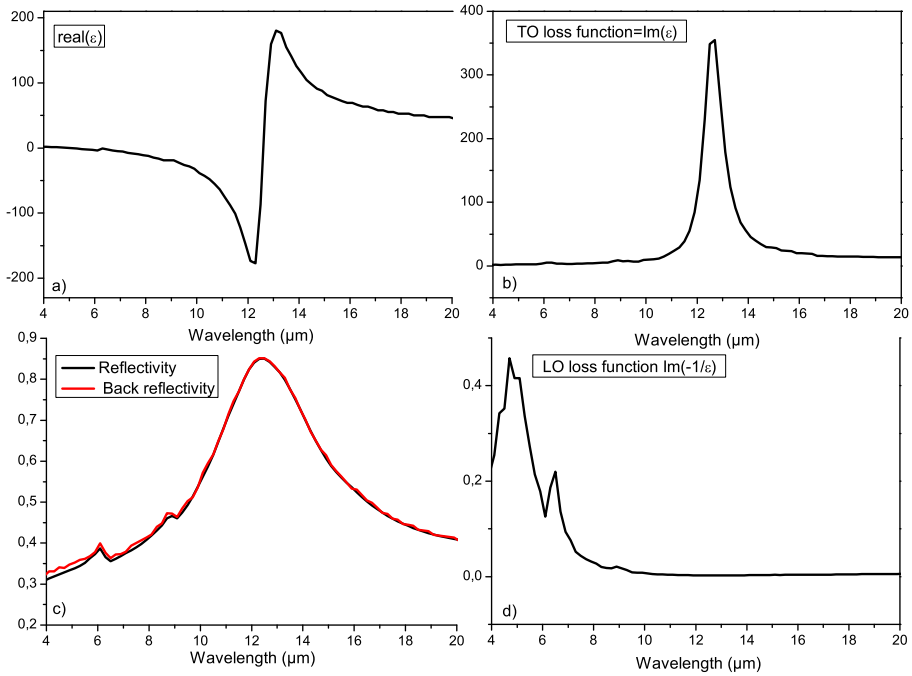

Figure 4.9.: Numerical simulation for rectangular structures. a) The real part of the permittivity, b) the imaginary part of the permittivity which denotes as well the TO loss function, c) the back-reflectivity is plotted along with the obtained one, d) the LO loss function which is calculated via the function by the imaginary part of $-1/\varepsilon$.

actual sample has been fabricated at Institut d'Electronique et des systèmes, Université de Montpellier, where the under-etching during the technological process had resulted in non-vertical side walls[48, 99]. In the simulation setup, the ribbon corners were rounded for two reasons, the first again it is more realistic and the second is to avoid numerical instabilities or divergence.

The reflectivity of this system was recorded upon illuminating with a plane wave source. The complex part θ of the reflectivity was then calculated by KK.

Fig. 4.11 shows the obtained values of the real and the imaginary parts of the permittivity, of the top layer. We notice a resonant behavior at wavelengths of (11-13 μm), where the real part is slightly negative and the imaginary part is small as explained in section (sec. 2.2.3). This resonant behavior comes from the plasmon response and it is tuned to be in the mid-IR by the doping level. The reflectivity of a homogenous layer of the obtained effective permittivity, of the same topographic thickness, on GaSb substrate was calculated. Fig. 4.12 compares the reflectivity ob-

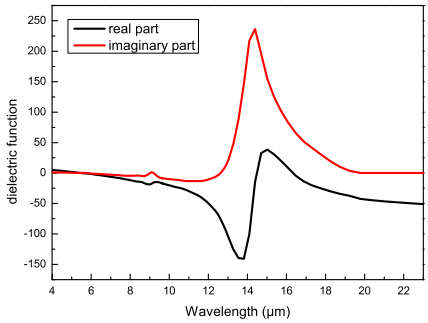

Figure 4.11.: Real and imaginary parts of the effective dielectric function obtained by TMM.

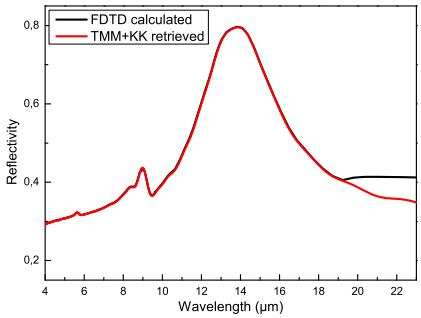

Figure 4.12.: Reflectivity of the system shown in Fig. 4.10, along with the reflectivity re-obtained using the effective dielectric function in Fig. 4.11.

tained for the system shown in Fig. 4.10 along with the reflectivity of a homogenous layer of the effective permittivity shown in Fig. 4.11. A very good agreement was obtained giving further assesment to the validity of our approach. Discrepancies are observed at high wavelength which most probably are due to the extrapolation in KK calculations.

4.3.4. LSPR angle dependence

In this section we study a resonant system at different excitation angles. For this purpose numerical simulations on a simple configuration were performed. The system is the same as Fig. 4.8 a), where the incident angle varies from 0 to 85°. RCWA numerical method was used to calculate the complex reflectivity at each angle of incidence then TMM was applied to determine the effective complex permittivity of the top layer. Fig. 4.13 and Fig. 4.14 show the real and imaginary parts of the dielectric function of the effective layer as function of wavelength and angle of incidence respectively.

As we see the resonant behavior is seen for all angles of incidence. It is more pronounced for normal incident angle, which is expected since this corresponds to base modes resonances that are most efficiently excited at normal incidence. However we were able to excite the system at all angles confirming that LSPR is a special case of SPP that does not require special configuration to be excited.

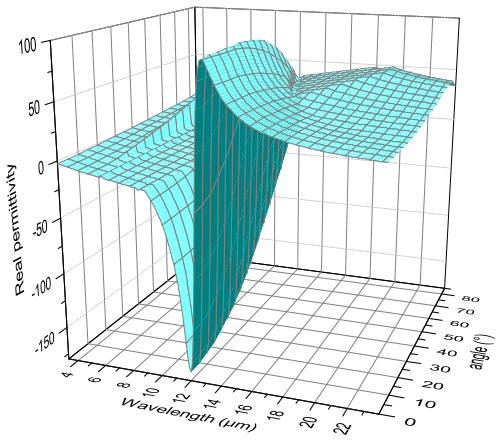

Figure 4.13.: Real part of the permittivity of the effective layer as function of wavelength and angle of incidence

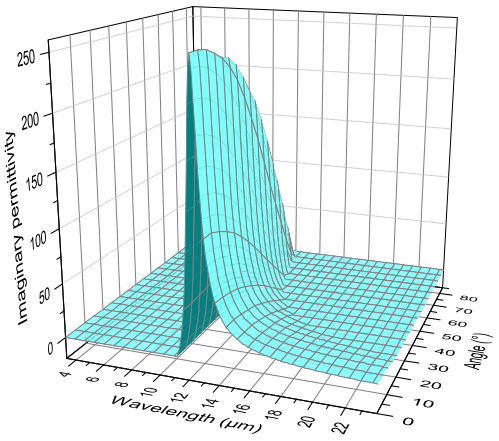

Figure 4.14.: Complex part of the permittivity of the effective layer as function of wavelength and angle of incidence

4.4. Effective Dielectric Function for the Surface Modes: case of a single interface

In the first part of this manuscript we have introduced the dispersion relation of the surface modes, when we consider a metal-like material in an external lossless medium. In the case of a simple interface, we obtained $\beta = \frac{\omega}{c}\sqrt{\epsilon_s}$ via the Brewster condition , where $\epsilon_s = \frac{\epsilon_1\epsilon_2}{\epsilon_1+\epsilon_2}$. By analogy with the dispersion relation in a bulk material, ϵ_s can be considered as the effective dielectric function seen by the radiation Brewster mode and the confined surface mode.

It is instructive to plot this permittivity in the case of interest, i.e. for an incident medium corresponding to the air $\epsilon_1 = 1$ and for a sample having a metal like permittivity. For highly doped semiconductor this behavior is observed below the plasma frequency (above the plasma wavelength), while the negative permittivity can also be obtained below the LO frequency for undoped polar crystal. Fig. 4.15 represents ϵ_s in case where ϵ_2 is modulated by the Drude model. The model parameters given in the figure caption correspond to doping levels and damping achieved in highly doped InAsSb [99, 48]; a similar trend is obtained for a polar material considering λ_{LO} instead of λ_p.

As can be observed in the presented case, ϵ_s behaves as a dielectric function corresponding to a single damped Lorentzian oscillator (DLO) with a LO like frequency at $\omega = \omega_p$, where the permittivity vanishes. This is an interesting result showing that the presence of the surface creates the restoring force responsible for a Lorentzian oscillation. In order to fully characterize this oscillator, we need to determine the

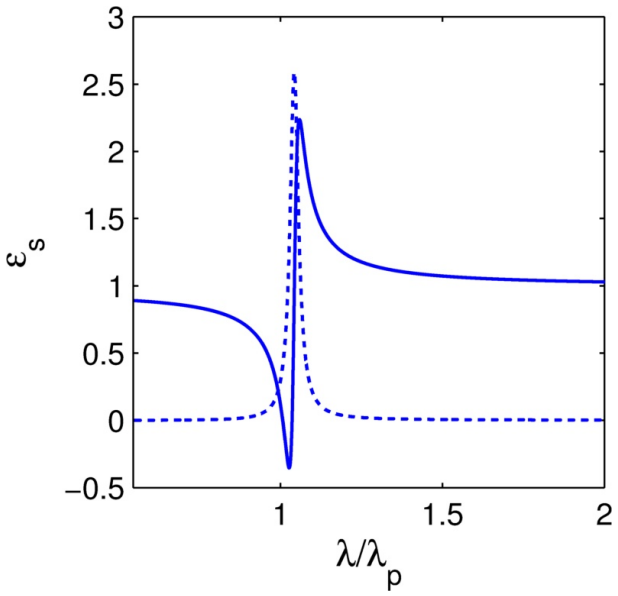

Figure 4.15.: Plot of the effective dielectric function ϵ_s perceived by the radiation Brewster mode and the SPP. We used $\epsilon_2 = \epsilon_{InAsSb}(\omega) = \epsilon_{2\infty}\left(1 - \frac{\omega_p^2}{\omega(\omega + j\gamma_p)}\right)$ with a plasma frequency corresponding to a wavelength of 5.5 µm , $\epsilon_{2\infty} = 11.7$ and $\gamma_p = 10^{13} s^{-1}$. This curve can be perfectly fitted by a Lorentzian function.

ingredients appearing in the dielectric function given by equation (2.3) that we can express here as:

$$\epsilon_s(\omega) = \frac{\epsilon_1 \epsilon_2(\omega)}{\epsilon_1 + \epsilon_2(\omega)} = \epsilon_{s\infty} + \frac{S\omega_{TO}^2}{(\omega_{TO}^2 - \omega^2 - i\Gamma\omega)}$$

These ingredients are: the high frequency limit $\epsilon_{s\infty}$, the oscillator strength $S = \epsilon_{s\,st} - \epsilon_{s\infty}$, the damping Γ, and the transversal resonance frequency ω_{TO} . This is obtained straightforwardly by considering the limit values of ϵ_S, and using the LST relation. We find:

- $\epsilon_s^\infty = \frac{\epsilon_2^\infty \epsilon_1}{\epsilon_2^\infty + \epsilon_1}$, and[10] $\epsilon_s^{st} = \epsilon_1$, $\Gamma = \gamma_p$
- $\omega_{TO}^2 = \frac{\epsilon_s^\infty}{\epsilon_s^{st}} \omega_{LO}^2 \rightarrow \omega_{TO} = \sqrt{\frac{\epsilon_2^\infty}{\epsilon_2^\infty + \epsilon_1}}\omega_p$

We recover the Fröhlich frequency $\omega_{TO} = \frac{\omega_p}{\sqrt{2}}$ in case of plasma/air interface. For a real material ϵ_2^∞ representing the deep electron contribution can be large and the TO frequency is close to the LO frequency (ω_p). The obtained result is exact in the case of a Drude-like material; it is a valid approximation in the metal-like region of a polar crystal.

[10]For a polar crystal: $\epsilon_{s\,st} = \frac{\epsilon_{2\,st}\epsilon_1}{\epsilon_{2\,st} + \epsilon_1}$,

Effective permittivity of metal-like inclusions

We have seen that the SPP of a dielectric-metal interface described by a Drude model experiments an effective permittivity corresponding to a DLO; a similar behaviour being obtained for a SPhP in the metal-like region. An effective permittivity can also be determined for the confined eigenmode of a metal or metal-like slab embedded in a dielectric, although there is no analytical solution in this case. As can be inferred from the dispersion relation plotted in chapter 1, the numerical analysis of the dispersion relation in a slab mode shows that $\epsilon_{eff} = (\beta/k_o)^2$ has also a nearly DLO behaviour.

Based on these results, we can question if a DLO can also precisely accounts for the effective permittivity of certain LSP or LSPh. We can obtain a general idea by looking at the effective permittivities provided by effective medium theories [31, 78]. We consider here the effective permittivity of a medium consisting of small metal or metal-like inclusions in a dielectric host ϵ_h, homogeneously distributed. Such medium can be seen as an isotropic metamaterial with a permittivity correctly described by the Maxwell-Garnett formula:

$$\epsilon_{eff} = \epsilon_h \frac{2V(\epsilon_m - \epsilon_h) + \epsilon_m + 2\epsilon_h}{2\epsilon_h + \epsilon_m + V(\epsilon_h - \epsilon_m)}$$

where V is the volume fraction of the inclusion. If we describe the metal-like behavior of ϵ_m with a Drude model (ω_p, γ, ϵ_m^∞), then ϵ_{eff} presents maxima corresponding to LSP/LSPh but is clearly more complex than a pure Lorentzian. However, if we consider V small enough and that ϵ_m is much larger than ϵ_i, the expression reduces to:

$$\epsilon_{eff} = \frac{\epsilon_h \epsilon_m}{\epsilon_h(2+V) + \epsilon_m(1-V)} = \frac{1}{\alpha\beta} \times \frac{\alpha\epsilon_h \times \beta\epsilon_m}{\alpha\epsilon_h + \beta\epsilon_m}$$

with

$\alpha = (2+V)$ and $\beta = (1-V)$

In this case, the effective permittivity is still a DLO with $\omega_{LO} = \omega_p$ and can be expressed as:

$\epsilon_{eff}(\omega) = \epsilon_{eff}(\infty) + \frac{S\omega_{TO}^2}{(\omega_{TO}^2 - \omega^2 - i\Gamma\omega)}$

with

- $\Gamma = \gamma_p$
- $S = \epsilon_{eff}^{st} - \epsilon_{eff}^{\infty}$, where:

  - $\epsilon_{eff}^{\infty} = \frac{\epsilon_m^{\infty}\epsilon_h}{\alpha\epsilon_h+\beta\epsilon_m^{\infty}}$
  - $\epsilon_{eff}^{st} = \alpha\epsilon_h$

- $\omega_{TO}^2 = \frac{\epsilon_{eff}^{\infty}}{\epsilon_{eff}^{st}}\omega_{LO}^2 \rightarrow \omega_{TO} = \sqrt{\frac{\epsilon_m^{\infty}}{\alpha^2\epsilon_h+\alpha\beta\epsilon_m^{\infty}}}\omega_p$

Considering that V is small, we see that the TO resonance frequency is globally shifted toward low energy. For example, considering again hypothetical plasma inclusions in air, the Fröhlich frequency is $\omega_{TO} = \frac{\omega_p}{\sqrt{6}}$. As expected, this frequency also decreases as the permittivity of the host medium ϵ_h increases as we have obtained for the effective permittivity of the SPR mode. For small material inclusions in air, a maximum resonance frequency at $\omega_{TO} = \frac{\omega_p}{\sqrt{2}}$ is attained for a high ϵ_m^{∞} material in the air.

4.5. Coupled Damped Oscillators: Modified Lorentz Model

This model is most appropriate to know the exact information about bulk material, through fitting the FTIR reflectivity spectrum. The advantage of FTIR technique is that relatively simple theory exists between the reflectivity measurement and the material dielectric function.

$$R = \left|\frac{\sqrt{\epsilon}-1}{\sqrt{\epsilon}+1}\right|^2$$

In order to have quantitative information the obtained reflectivity spectra should be fitted to a theoretical model. The model used in this work has been developed and showed to give better agreement with experimental spectra [117] than the commonly used models [82]. To grasp the basic features of the model a brief description of the used theories is given below.

In this model, the classical picture of the lattice vibration described as purely independent harmonic oscillators described by equation (2.3) is unconstrained and coupled damped oscillators are considered. In the case of having two-mode system, detailed explanation could be found in [16], the dielectric function is expressed as follows:

$$\epsilon = \epsilon_{\infty} + \epsilon_1 + \epsilon_2$$

$$\epsilon_1 = \frac{4\pi z_1^2 + i4\pi z_1 z_2 \omega\Gamma_{1,2}/[\omega_{TO,2}^2 - \omega^2 + i\omega(\Gamma_2+\Gamma_{1,2})]}{\omega_{TO,1}^2 + \omega^2 + i\omega(\Gamma_1+\Gamma_{1,2}) + \omega^2\Gamma_{1,2}^2/[\omega_{TO,2}^2 - \omega^2 + i\omega(\Gamma_2+\Gamma_{1,2})]}$$

Where, ϵ_∞ denotes the high frequency limit of ϵ, Γ is damping coefficient. ω_1 is the resonance frequency of the first oscillator, this is usually taken from literature; however slight modification could be conducted to the values embedded in the numerical model to obtain the best fit. z_1 is related to S_1 (strength of the first oscillator) through $z_1 = \omega_1\sqrt{S_1/4\pi}$. In used numerical model, the oscillator strength was left as free parameter to adjust in a way to best fit the experimental data. Interchange of subscripts to gives ϵ_2. This could be generalized to any number of modes depending on the system, then we need to sum all the involved modes. For instance, for our SiC 6H, 6 modes are involved so our dielectric function is:

$$\epsilon = \epsilon_\infty + \epsilon_1 + \epsilon_2 + \epsilon_3 + \epsilon_4 + \epsilon_5 + \epsilon_6$$

where:

$$\epsilon_1 = \sum_{j=1}^{6} \frac{4\pi z_1^2 + i4\pi z_1 z_j \omega \Gamma_{1,,j}/[\omega_{TO,j}^2 - \omega^2 + i\omega(\Gamma_j + \Gamma_{1,j})]}{\omega_{TO,1}^2 + \omega^2 + i\omega(\Gamma_1 + \Gamma_{1,j}) + \omega^2\Gamma_{1,j}^2/[\omega_{TO,j}^2 - \omega^2 + i\omega(\Gamma_j + \Gamma_{1,j})]}$$

and:

$$\epsilon_2 = \sum_{j=1}^{6} \frac{4\pi z_2^2 + i4\pi z_2 z_j \omega \Gamma_{2,,j}/[\omega_{TO,j}^2 - \omega^2 + i\omega(\Gamma_j + \Gamma_{2,j})]}{\omega_{TO,2}^2 + \omega^2 + i\omega(\Gamma_2 + \Gamma_{2,j}) + \omega^2\Gamma_{2,j}^2/[\omega_{TO,j}^2 - \omega^2 + i\omega(\Gamma_j + \Gamma_{2,j})]}$$

and so on till ε_6. The first basic improvement involved in the used model is that the anisotropicity of the material is taken into account. Where two different solutions to the wave equation exist. Hence, two dielectric functions were considered. The ordinary (perpendicular) and extraordinary (parallel) to the plane defined by the material optical axis (c-axis) and the incident electromagnetic wave vector:

$$\epsilon_{1,\|(\perp)} = \frac{4\pi z_{1,\|(\perp)}^2 + i4\pi z_{1,\|(\perp)} z_{2,\|(\perp)} \omega \Gamma_{1,2}/[\omega_{TO,2,\|(\perp)}^2 - \omega^2 + i\omega(\Gamma_{2,\|(\perp)} + \Gamma_{1,2})]}{\omega_{TO,1,\|(\perp)}^2 + \omega^2 + i\omega(\Gamma_{1,\|(\perp)} + \Gamma_{1,2}) + \omega^2\Gamma_{1,2}^2/[\omega_{TO,2,\|(\perp)}^2 - \omega^2 + i\omega(\Gamma_{2,\|(\perp)} + \Gamma_{1,2})]}$$

Moreover, considering only the harmonic term in the lattice potential is a consequence of considering the normal modes as independent oscillators; however this is clearly unphysical since the unharmonic terms dictate the interaction between these oscillators. In other words, the harmonic term gives information about the energy and number of phonons carrying the heat, while the unharmonic terms describe the phonon-phonon interaction and scattering mechanisms. Considering the unharmonic terms are indispensable for explaining a lot of physical phenomena, for example, the temperature dependence of the specific heat [102], and the thermal conductivity[2] [66], the thermal expansion coefficient [88], and the temperature and pressure dependence of the elastic constants [56, 126], etc. Hence, the second improvement, that led to a remarkable fit amelioration, is that the damping "constant"

is no more constant but rather a function of the frequency and temperature. In order to calculate this dependency, Hamiltonian perturbation theory is used. These perturbations give information about the three-phonon and four-phonon decay processes, more detailed description could be found in [16, 117][11]. So the process is as follows:

photon l $\rightarrow$ optical phonon j $\rightarrow$ several phonons f

After interacting with a photon an initial optical phonon j could decay into several acoustic final phonons f. This transition depends on the phonon branches or in other words the available channels. The idea behind studying the nanopillars is to see the possibilities of making new channels in comparison to the bulk SiC. The net transition probability:

$$\left| \frac{\sum_j H_{lj} H_{jf}}{(\omega_l - \omega j)} \right|^2$$

$$H = H^{harm} + H_3^{an} + H_4^{an}$$

The frequency-dependent scattering rate, τ^{-1}, for three- and four-phonon processes is then obtained within the linear approximation of the first order perturbation to the cubic and quartic Hamiltonian. This lead to the decay rate with three-phonon process:

$$(\tau_3^{-1})_j = (A_3)_j \omega^5 \coth(\frac{\hbar\omega}{2k_B T})$$

Four-phonon process:

$$(\tau_4^{-1})_j = (A_4)_j \omega^9 [(\frac{3}{e^{\frac{\hbar\omega}{k_B T}} - 1})^2 + (\frac{3}{e^{\frac{\hbar\omega}{k_B T}} - 1}) + 1]$$

The frequency-dependent damping coefficient of the optical phonon j, that should have a wave number dimension and the meaning of a scattering rate is defined as:

$$\Gamma_j = (C_3)_j (\tau_3^{-1})_j + (C_4)_j (\tau_4^{-1})_j$$

$$(C_3)_j = \frac{1}{c(A_3)_j} \qquad (C_4)_j = \frac{1}{c(A_4)_j}$$

C_3, C_4 are frequency-independent constants, they are set as free adjustable parameters. Since in general we do not know the explicit functional dependence of the potential energy on the atomic displacement we have to regard the atomic force constants as parameters whose numerical values are determined from experimental data.

[11] This theory of lattice dynamics discussed here describes intrinsic effects since we are dealing with a relatively defect-free SiC material.

4.6. Conclusion

In this chapter we have presented the tools we are going to use to investigate the plasmonic response in highly doped semiconductor as well as the phonon behavior in polar crystals. We have demonstrated that the surface mode dielectric function corresponds to a damped Lorentzian oscillator; in other words, the presence of a surface creates a restoring force that is responsible for such a behavior. Also we have used numerical simulations to see the effect of angle of incidence of the LSPRs. In the first part, we have detailed a model based on the TMM, used specifically to determine the properties of a sandwiched layer without any prior knowledge of the material except for the thickness. This model is based on solving Maxwell equations with proper boundary conditions. In the second part, a modified Lorentz model was used to represent the permittivity. The used model takes into account the anisotropicity of the material as well as the anharmonic phonon decay. Some parameters were left as adjustable so that we can fit the experimental FTIR reflectivity spectra. The idea is to understand quantitatively the collective phonon response in the infrared regime. The common tool that we have utilized in both parts is the Kramers Kronig technique, these are relations that enable us to find the imaginary part of a function knowing its real part; of course the function should satisfy couple of conditions.

5. Results

In this chapter we present the results that were obtained via far-field interaction, where the collective response of the material has been studied. It is split into two parts: The first part characterizes the resonances in a sub-wavelength grating of highly doped semiconductor, the second part deals with the effect of nanostructuring the surface on the phonon response.

5.1. Experimental Setup

In our experiments, the FTIR system used is a Nicolet 4700 spectrometer from Thermo Electron Corporation with a DTGS detector and a KBr beam-splitter, in the mid-infrared range of 400-4000 cm^{-1}. Near normal incidence angle was fixed. We performed 200 scans on the samples while fixing the resolution to $1cm^{-1}$ in order to improve the signal-to-noise ratio. Because the sample compartment is not evacuated, there needs to be a relative scale for the absorption intensity. Thus, we use a gold coated mirror to collect a background spectrum before each measurement. The spectrum of the sample is then normalized to the background to remove the contribution of all of the instrumental and environmental characteristics to the infrared spectrum. Thus, all spectral features which are present in the obtained spectrum are strictly due to the sample. Parameters adjustment and data acquisition are made by OMNIC software.

5.2. Detecting Resonances in Highly Doped Semiconductor Grating

Our study concentrates on the material properties in the mid-infrared. In this section we will study the resonances induced by plasmonic behavior in highly doped semiconductor. In order to see the collective response of the material we have performed a spectroscopic far-field study through FTIR measurements. The index of refraction and the extinction coefficient were determined using a technique based on the combination of Kramers-Kronig theorem with the classical theory of electromagnetic wave propagation in a system of thin films.

5.2.1. Sample Fabrication

The studied sample is fabricated in Institut d′Electronique et des systèmes, Universit*é* de Montpellier, by Dr. T. Taliercio group [48]. It is made of highly doped lines of InAsSb on GaSb. (Fig. 5.1) shows a SEM image of the sample.

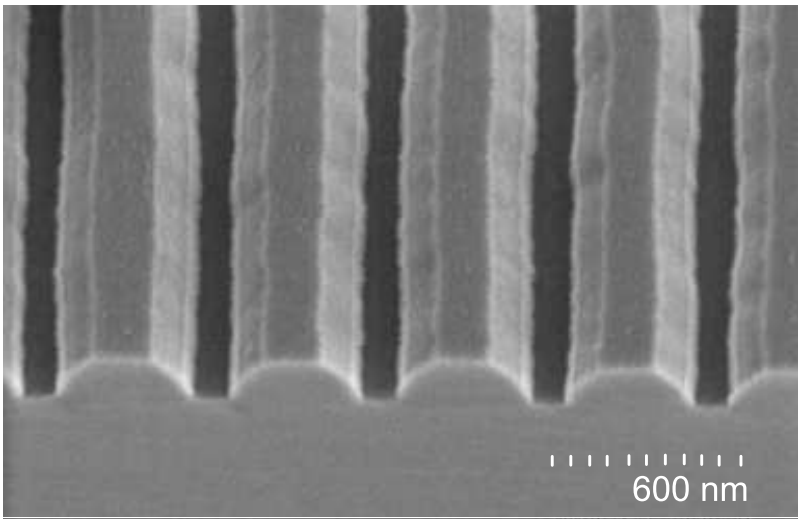

Figure 5.1.: SEM image of the studied InAsSb grating.

The InAsSb layer is n-doped with Si at doping level of $5 \times 10^{19}\text{cm}^{-3}$. It is deposited by molecular-beam epitaxy on GaSb doped with Te at doping level of $2 \times 10^{18}\text{cm}^{-3}$. A SiO_2mask is deposited on the top. The grating is then defined by holography using an AZMIR 701 positive photoresist, followed by reactive chemical etching. The final shape of the lines is trapezoidal with base length of 420 nm, top length 120 nm and height of 140 nm. The period of this grating is 520 nm. This system is made based on the prospective application in plasmonic devices. InAsSb material was used because of the impressive doping level it offers, giving the possibility to tune the bulk plasma wavelength down to values as low as 5 µm. The effective mass of electrons in InAs is also small in comparison to other highly doped semiconductors, the small effective mass promotes the ability to increase the plasma frequency (see equation (2.5)). Another reason for developing this specific system is that the InAsSb is lattice-matched with the GaSb substrate, this is quite important when it comes to the field of application.

5.2.2. Results and Discussion

FTIR was obtained at quasi-normal incident IR-beam with p-polarization. KK relations were applied to have the complex part θ in equation (4.1); extrapolation has been performed at the extremities (fitting the extremities by 5 Lorentzian). TMM (discussed in sec. 4.3) has been then applied to obtain the complex index of

refraction of the top layer. Fig. 4.5 is the schematic sketch of our system, where an effective layer of highly doped InAsSb + air was assumed, deposited on a GaSb substrate. (Fig. 5.2) shows the obtained complex permittivity. We see that the real part of the permittivity goes from positive to negative exhibiting a damped resonant behavior.

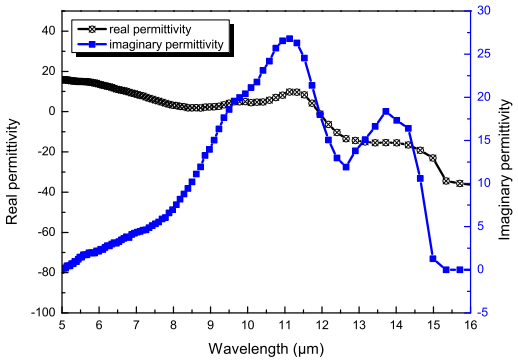

Figure 5.2.: Real part of the dielectric function of the effective layer (black) along with its imaginary part (blue).

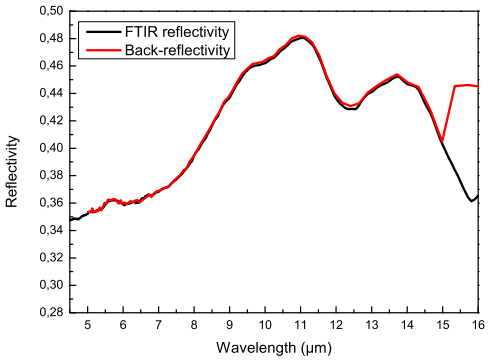

Figure 5.3.: FTIR reflectivity spectrum along with the back calculated reflectivity.

Fig. 5.3 shows the measured reflectivity along with the back calculated reflectivity. The back reflectivity was calculated using the complex permittivity shown is Fig. 5.2. A very satisfactory agreement is noticed where we were able to back map all the features in the reflectivity; however, as mentioned before, this model doesn't work properly at the extremities due to the extrapolation. Fortunately this is located outside our region of interest.

We must point out that a constant term of 0.4 rad was added to the values of θ so that the obtained back reflectivity is optimum. This term is regarded as a constant correction to KK relations. Two factors involved in our experiment might be the reason behind the necessity of this correction term. The first reason comes from the fact that the permittivity function for the substrate was used from literature, while the actual substrate is Te doped with plasma wavelength of 30 μm, this introduces a sharp non-accounted for decrease at wavelengths of 20 μm, more details is found in [48]. The second reason might be stemmed from overestimation or underestimation of the reflectivity while extrapolating at 0 frequency and at infinity.

In order to determine precisely the resonance frequencies and specify their nature, Fig. 5.4 presents the TO and LO loss functions given by equation (4.8) and equation (4.9) respectively .

As we can see we have three resonance frequencies corresponding to the TO vibrations, $\omega_{1TO} \approx 9.7\mu$m, $\omega_{2TO} \approx 11.1\mu$m, and $\omega_{3TO} \approx 13.8\mu$m. Let's have a look back on Fig. 4.9 b), that shows the TO loss functions for simulated rectangular structures

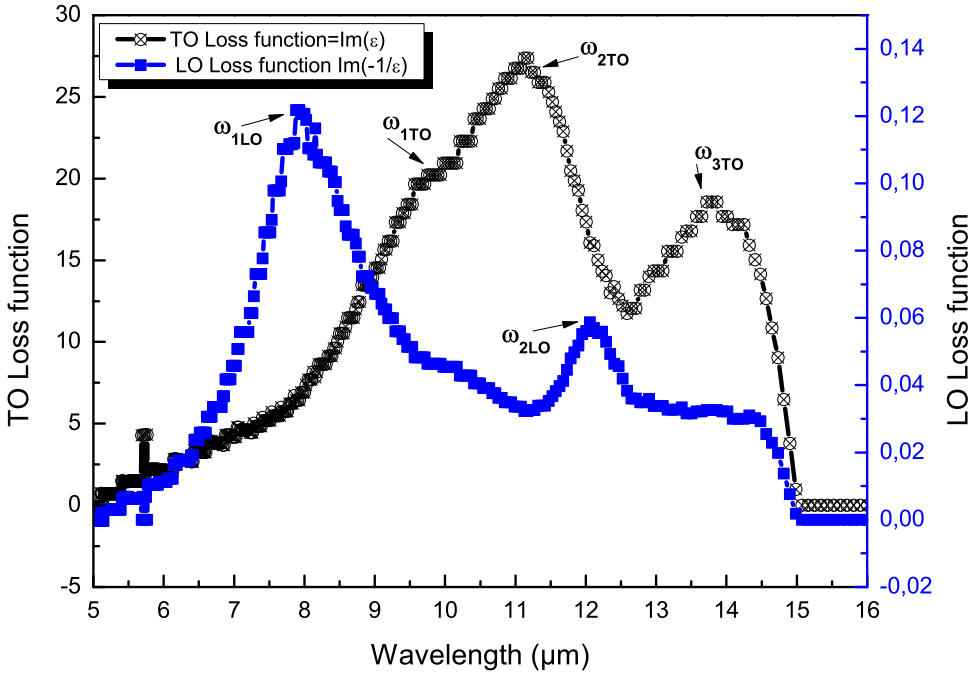

Figure 5.4.: TO loss function showing TO resonance frequencies as well as LO loss function showing the LO resonance frequencies.

of same doping level, where there is one TO resonance frequency ($\omega_{TO} \approx 12.5\mu$m). We notice that there is a marked splitting in the resonance frequency for our sample. This phenomena has been seen previously in [48], and is attributed to non rectangular shape of ribbons. The ribbons in our sample correspond more to a trapezoidal shape than a rectangular shape which is the reason behind multiple TO resonance frequencies: the symmetry reduction produce a degeneracy lifting of the TO resonance.

Having a look on the LO loss function shown in Fig. 5.4 gives us clear idea about the peak positions of LO vibrations. We notice two strong peaks $\omega_{1LO} \approx 7.9\mu$m and $\omega_{2LO} \approx 12\mu$m.

5.3. Conclusion on the first method

We have developed an approach to retrieve the optical properties of the top layer in a system. After proving its validity, through running couple of demonstration tests, our developed model was applied to study resonant systems. We were able to have a clear phenomenological, macroscopic image for a resonant highly doped InAsSb

grating. Using relatively simple theories we have extracted accurate information about the resonance frequencies in our system and specify their nature. The approach involved FTIR measurements, then KK relations were applied to determine the phase of the reflectivity (after measuring the real part $\ln\left(\sqrt{R}\right)$). The complex index of refraction were calculated based on the TMM. The resonance peaks were identified by finding LO and TO loss functions.

5.4. Effect of Nano-pillars on Phonon Behavior

Our goal in this part is to understand the phonon resonances, lifetime and scattering rates. Since this plays a major role in all the phonon-based applications. The infrared complex dielectric function of a crystal is determined by the harmonic characteristics of the phonon together with the intrinsic and extrinsic phonon scattering rates. In order to investigate the interplay between the phonon intrinsic scattering and the scattering of the phonon by a nanostructured surface, infrared reflectivity measurements from SiC nano-pyramids on SiC substrate have been analyzed using a Kramers-Kronig conversion technique to deduce the infrared complex dielectric function. Then, the real and imaginary parts of the dielectric function were fitted simultaneously by using a theoretical model for the dielectric constant that considers frequency-dependent phonon damping at the center of the Brillouin zone. It has been found that surface nanostructuring strongly enhances the overall scattering rate of the phonon at the Brillouin zone center [3].

5.4.1. Sample Fabrication

We have purchased good-crystalline quality SiC wafers from Cree, Inc. The sample was cut into two pieces, where the nanostructures were fabricated on one of them. The pattern of the structures was drawn by electron-beam lithography on a large surface (2.5×2.5 mm^2), preceded by the deposition of positive tone PMMA resist, followed by lift-off procedure. An Al layer was then deposited as a mask for Reactive Ion Etching (RIE) of the patterned SiC substrate. RIE was operated with the use of inductively coupled plasma in a mixture of 60% SF6 and 40% O_2 at 3 mTorr pressure. The residual mask was removed in aqueous solution of KOH.

5.5. Results and Discussion

Fig. 5.5 shows the fabricated nanostructured SiC with diameters ranging from 70 nm to 100 nm. We investigated the surface phonons in SiC and the effect of the structuring on their lifetime. We measured the intact surface SiC reflectivity and that of the surface with nanostructures. Fig. 5.6 is the unpolarized infrared reflectivity

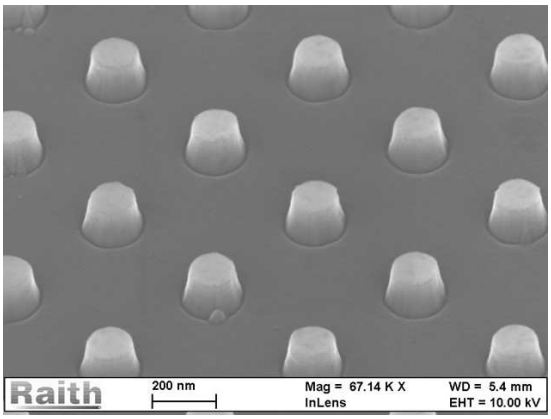

Figure 5.5.: SEM image of SiC Nanostructures on SiC substrate.

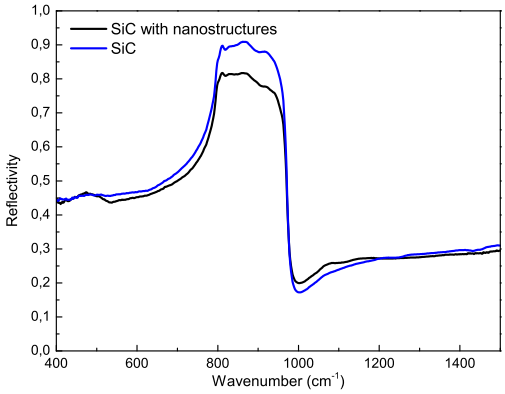

Figure 5.6.: Reflectivity measurements on SiC wafer and nanostructured SiC.

measurements made on SiC unmodified wafer and on the fabricated nanostructured SiC. A clear difference is noticed between the two reflectivity spectra. This difference can not be due to light diffusion because the size of the nanostructures is about two orders of magnitude smaller than the light wavelength. In order to understand quantitatively the process, we used the model discussed in sec. 4.5 to find the two complex dielectric functions of SiC and that of SiC nanostructures. Each complex dielectric function was calculated based on its isotropic and anisotropic components using the following relation:

$$\epsilon = \epsilon_{\text{iso}} \cos\phi + \epsilon_{\text{aniso}} \sin\phi$$

Where ϵ_{iso} and ϵ_{aniso} are the respective isotropic and anisotropic dielectric functions calculated based on 6 oscillators: 6 oscillator resonance frequencies, 6 oscillator strengths, 6 damping coefficients for the three phonon decay processes, 6 damping coefficients for the 4 phonon decay processes each. ϕ is the angle between the total electric field and the anisotropic plane, which is left as free adjustable parameter as well.

On the other hand, the reflectivity measurements have been converted into real and imaginary parts of the dielectric functions using Kramers-Kronig relations (sec. 4.2). Then the real and imaginary parts for the intact SiC were fitted simultanously with the previously discussed model. The adjustable parameters were changed so that the best fit is obtained. The same procedure was repeated for that of the SiC with structured surface. Fig. 5.7 and Fig. 5.8 show the obtained results. The data from the nanostructured SiC is plotted along with that of the intact SiC. The experimental real and imaginary functions (symbols) are fitted simultaneously with the coupled damped oscillator model (solid lines). Two main transverse extraordinary ($\|$) phonon modes at frequencies of 805 cm^{-1} and 820 cm^{-1} and one main transverse ordinary ($\perp$) phonon mode of frequency 800 cm^{-1} were found. The best fit is mostly

affected by considering the 3-phonon decays, which demonstrates that at room temperature the 3-phonon decay processes are the dominant mechanism. However no change in the resonance frequencies of the oscillators were observed.

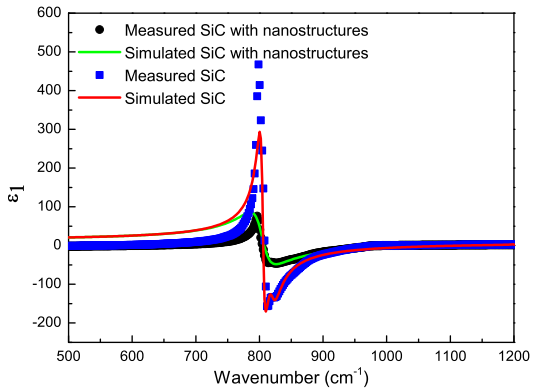

Figure 5.7.: Real part of the dielectric function for SiC (blue), and nanostructured SiC (black). The symbols correspond to the measured data, the smooth line to the fitted one.

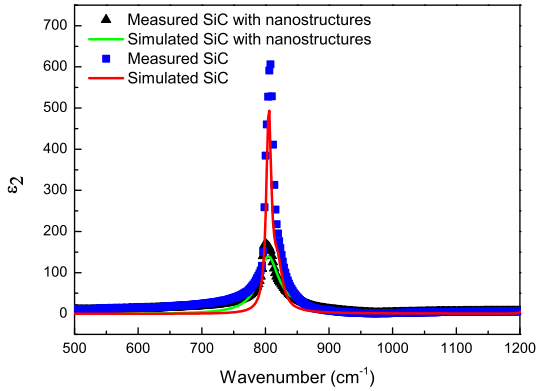

Figure 5.8.: Imaginary part of the permittivity for SiC (blue), and nanostructured SiC (black). The symbols correspond to the measured data, the smooth line to the fitted one.

A remarkable difference in the permittivity was observed due to the introduction of the nanostructures. From the fit we deduce that the presence of nanostructure has increased significantly the phonon damping. Fig. 5.9 compares the damping constants of the two investigated samples. We found that the damping constants related to the intact sample is ranging from 6 times to an order of magnitude smaller than that of the surface with nanostructures depending on the frequency range. The scattering rate is affected most towards high frequencies. Since the two measured samples come from the same epitaxial layer, we attribute the enhancement of the scattering rate to collisions between the surface phonons and the structures. In other words, the nanostructures exhibit local resonances that couple or hybridize with the underlying phonon dispersion of the film. These couplings drastically increase the phonon scattering rate, due to the increase number of channels for phonon decay. This consequently lower the thermal conductivity of the material towards attaining a better figure of merit (ZT).

A key advantage to point out here is that the desirable decrease in thermal conductivity is *a priori* attained without negatively impacting the electrical conductivity. Since the features (nanostructures) manipulating the phonon scattering rate are physically found outside the sample itself; hence the primary flow path of the electrons is uninterrupted[34]. This contrast with other methods like thin-film-based nano-phononic crystals, where the doping or the holes penetrate the whole sample and may alter both the phonon and electron scattering at the same time.

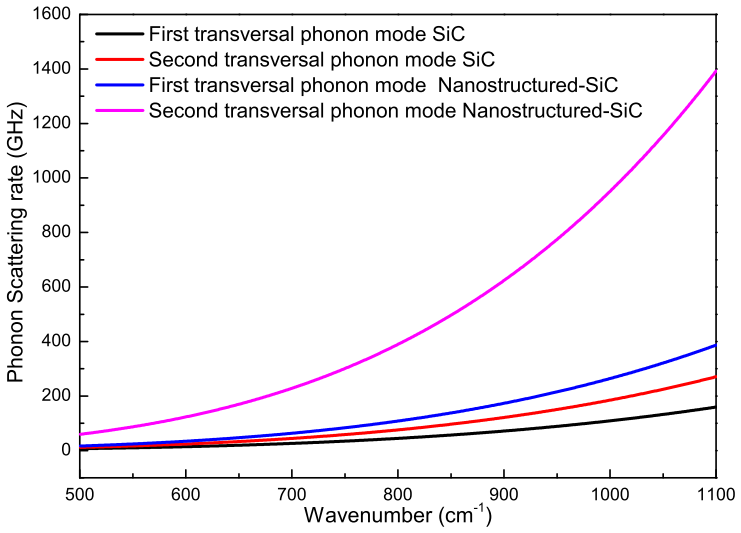

Figure 5.9.: Calculated phonon scattering rate from the experimental fit.

We would like to point out that the first step towards treating the SiC nanostructures was applying the TMM; while modeling the nanostructures + air as effective layer. The idea was similar to that followed with highly doped semiconductor: obtain a LSPh resonance in the nanostructured effective layer and deduce the effective permittivity of the layer. In addition the nano-structure were made small in order to eventually observe phonon confinement effect in SiC that would produce a change in the phonon density resulting in a change in the permittivity of SiC inside the layer. However upon having no successful findings with the TMM method, we ended up concluding that actually these nanopillars are altering the underling substrate; which can not be modeled by TMM. So we deviated towards modeling the reflectivity of the modified substrate as a whole with modified dielectric function.

The fact that the LSPhR is not distinguishable is not so surprising, considering that the dimensions of our fabricated structures are small to exhibit a strongly pronounced phononic resonance. In a recent work, S. A. Maier and his group [30], were able to see a strong phononic response in SiC; however this was observed for structures of diameters 0.5, 0.75, and 1 μm, height of 1 μm, with interpillar gap of 2 μm . In order to investigate this further, FDTD simulations were performed to confirm that the strong field enhancement is observed starting from a topographical height of 300 nm and diameter of 400 nm. In the same time these structures were too large to see phonon confinement effect and a drastic change in the phonon dispersion[64].

5.6. Conclusion on the Second Method

Phonon scattering by surface structuring is illustrated in the case of SiC. Infrared reflectivity measurements have been converted into real and imaginary parts of the material dielectric function. The results have been fitted to Lorentz model that considers coupled oscillators and frequency-dependent damping coefficient. We have found that the surface structuring enhances the phonon scattering mechanisms up to an order of magnitude depending on the frequency range. Thus a considerable decrease in the thermal conductivity could be attained. We hope that these results stimulate further experiments on tailoring the harmonicity and anharmonicity of the phonons for controlling the SiC infrared properties for the use in SiC-based devices. The proposed structure is particularly interesting since it does not influence the electric conductivity.

5.7. General Conclusion

In this chapter we have studied the global effective permittivity of a metamaterial. We were able to determine its complex dielectric function. In the case of highly doped semiconductor grating, that was modeled based on a TMM, i.e without any physical assumption; we have noticed that it has an inherent multiple Lorentz oscillator behavior. Couple of resonances were detected in the mid-IR region. Through our study we have used FTIR to measure the experimental reflectivity and then KK relations to determine its complex part. A model based on modified coupled Lorentz oscillator was used, in case of modifying the whole system. We have demonstrated the impact of nanopillars on a substrate.

Part III.

Near-field Optics Investigation

6. Near-field Developed Methods

In this chapter we present a novel phase and amplitude extraction method that can be implemented in many interferometry experiment[1]. In this chapter we present the theory of the approach, its test experiments and then its application to NSOM. The thought of this method emerged from the quest of the following properties in an interferometric detection method:

- Phase resolved interferometry: We need to extract phase and intensity of the scattered electric field in order to have complete information about the studied sample.
- Fast: As for many techniques, a slow scanning in NSOM may introduce a lot of problems, like deterioration of tip quality i.e lowering the resolution, thermal drift,...so having a fast detection response is highly recommended.
- Optimized signal to noise ratio: This means we want to exploit all the useful signal. This is a critical issue in low signal setups. For example, in our case, we are working with NSOM in the mid-IR we suffer further from the low scattered near-field signal due to the small scattering cross section (in comparison to the visible and near infra-red); thus we don't afford losing part of the useful signal.
- Removing unwanted signal component: This is extremely important in the case of high background like apertureless NSOM.
- Achromatic: The use of achromatic optical components is needed in spectroscopic studies. And since a lot of interferometric setups are integrated in spectroscopic experiments using mirror-based techniques is highly favored over AOM-based techniques [53, 35, 112].
- Cost-effective: It goes without saying that having a good quality to price ratio is highly favored and would facilitate the presence of technology in more research laboratories.

6.1. G-LIA Theory

The basic principle looks like the pseudo-heterodyne presented in (sec. 3.2.3.3), where the phase in the reference arm of an interferometer is being modulated by

[1] This approach has been the subject of a patent application and the technology is being transferred to an innovative company working in near-field optics (Molecular Vista inc.), in collaboration with H. K. Wikramasinghe, from UC Irvine.

adding a variable delay length and measuring the resulting interferences. In such a two-arm interferometer, we consider a monochromatic light of frequency ω. The interference intensity is:

$$I_{\text{det}} \propto \left\langle \left(E_S(t) + E_R(t)\right)^2 \right\rangle = {E_S}^2 + {E_R}^2 + 2E_R E_S \cos\left(\phi_S - \phi_R\right) \tag{6.1}$$

Here $E_S(t) = \sqrt{2}E_S \cos\left(\omega t + \phi_S\right)$ denotes the signal field with unknown amplitude E_s and phase ϕ_S. $E_R(t) = \sqrt{2}E_R \cos\left(\omega t + \phi_R\right)$ is the reference field with a constant amplitude and a time-modulated phase $\phi_R(t)$. In fact, $\phi_R(t)$ can be produced by either a phase, or an equivalent frequency modulation [59, 33]. In order to determine the unknown quantities $\phi_R(t)$ should be varied in time at a speed much faster then the expected variation of the unknown parameters (namely E_s and phase ϕ_S).

The intensity measured on a sufficiently short time can then be written as the sum of a constant or quasi-constant term and a modulated one :

$$I_{\text{det}} \quad \propto \quad I_0 + I_{\text{mod}}, \tag{6.2}$$

with $I_0 \simeq$ const. during a measurement, and

$$I_{\text{mod}} = 2E_R E_S \left[\cos\left(\phi_S\right)\cos\left(\phi_R\right) + \sin\left(\phi_S\right)\sin\left(\phi_R\right)\right]. \tag{6.3}$$

We see from equation (6.3) that the interesting term I_{mod} can be decomposed on the basis $\left(\cos\left(\phi_R\right), \sin\left(\phi_R\right)\right)$. An ideal way to determine amplitude and phase is then to achieve a linear phase variation $\phi_R = \Omega t$ and perform a synchronous detection by multiplying the detected signal by the two orthogonal harmonic references $\sin(\Omega t)$ and $\cos(\Omega t)$ and integrating over a sufficient time period. This process is the basic operation of a dual output LIA locked at the angular frequency Ω. The quantities (E_S, ϕ_S) are directly inferred from the two signal outputs (X,Y):

$$X_{\Omega t}\left(I_{\text{det}}\right) = \frac{1}{\Omega t_{int}} \int_0^{\Omega t_{int}} I_{\text{det}} \cos(\Omega t) d(\Omega t) = E_R E_S \cos\left(\phi_S\right) \tag{6.4}$$

$$Y_{\Omega t}\left(I_{\text{det}}\right) = \frac{1}{\Omega t_{int}} \int_0^{\Omega t_{int}} I_{\text{det}} \sin(\Omega t) d(\Omega t) = E_R E_S \sin\left(\phi_S\right). \tag{6.5}$$

where t_{int} is the integration time. Unfortunately, achieving a purely linear phase variation using phase modulators is not possible as they necessarily present a finite range of phase modulation. A well-known approach towards achieving a linear phase variation is to use serrodyne modulation, or in other words, to use a sawtooth modulation of the optical path in the reference arm. A quasi-harmonic modulation of I_{det} is then obtained if the full amplitude of the sawtooth corresponds to an integer number N times 2π (i.e. an optical path modulation of $N\lambda$).

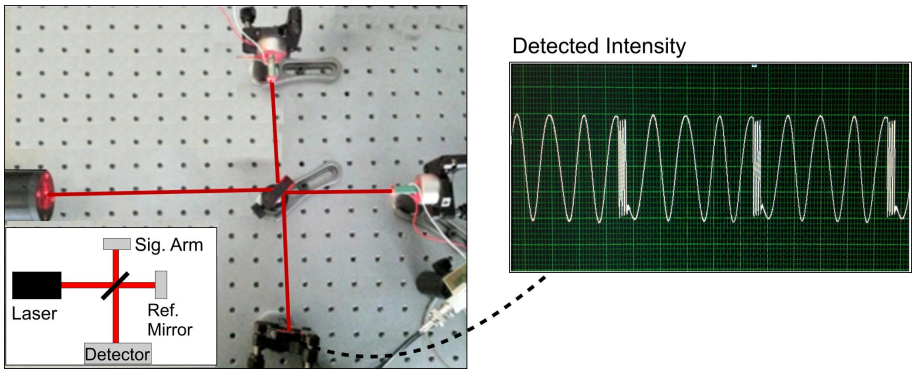

(a) The demonstration setup of Michelson interferometer, operating with λ =633 nm, along with interference pattern resulting in a quasi-harmonic pattern.

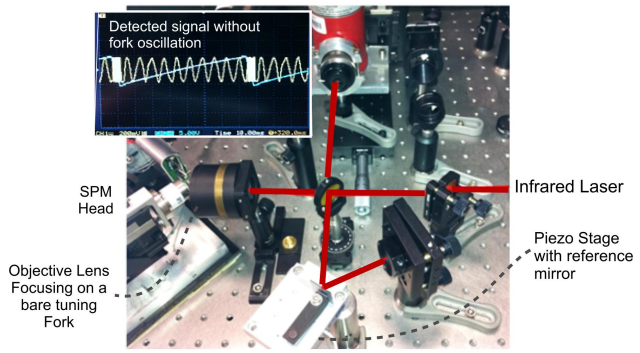

(b) NSOM demonstration setup operating in the mid-infrared regime (λ=10.6 μm). along with interference pattern obtained for a serrodyne excitation of the reference arm.

Figure 6.1.: Michelson setup with reference phase driven by saw-tooth modulation.

Fig. 6.1 a) shows a simple mounted Michelson interferometry operating with a He-Ne laser (λ=633 nm), with the obtained interference pattern detected by a photo-diode. Fig. 6.1 b) is our NSOM setup as well as the interference pattern obtained by an mid-IR operating CO_2 laser (λ=10.6 μm). A little precaution was taken in choosing the amplitude of oscillation of the driving signal. As we can see from Fig. 6.1, the obtained interference signal is quasi-harmonic however with a non-avoidable "flyback" time at the end of the sawtooth modulation. This introduces some noise and leads to a loss of information due to the "burned" pixels in the image. Therefore, serrodyne modulation is not highly recommended for fast or precise experiments, and a sinusoidal function $\phi_R = a \sin \Omega t$ is preferred.

As soon as a sinusoidal modulation is applied to the reference phase, the Fourier spectrum of I_{mod} is split into harmonic sidebands at radial frequencies $m\Omega$ see Fig. 6.2.

The amplitudes of these sidebands are obtained using Jacobi-Anger expansion of

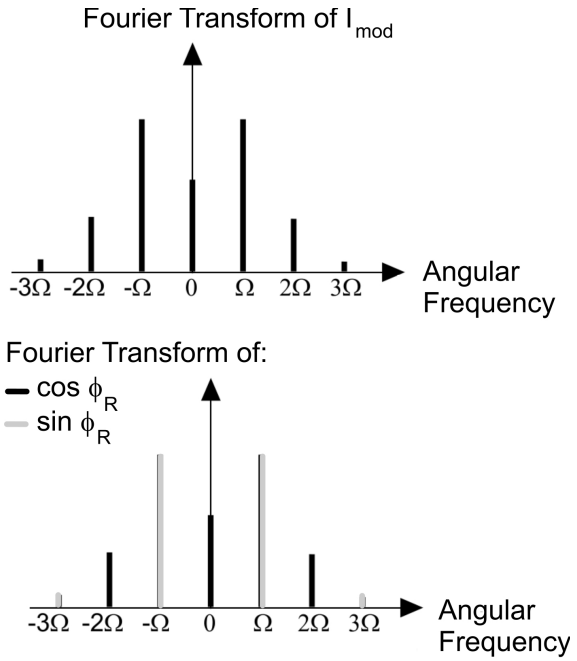

Figure 6.2.: Fourier transform of the modulated detected intensity when $\phi_R(t) = a \sin \Omega t$

$\cos(\phi_R)$ (where m is only even) and $\sin(\phi_R)$ (odd m only) [131]. Again, a synchronous detection at the harmonics $m\Omega$ provides:

$$X_{m\Omega t}(I_{\text{det}}) = 2E_R E_S \cos(\phi_S) \begin{cases} J_m(a) & \text{for m even} \\ 0 & \text{for m odd} \end{cases} \tag{6.6}$$

$$Y_{m\Omega t}(I_{\text{det}}) = 2E_R E_S \sin(\phi_S) \begin{cases} 0 & \text{for m even} \\ J_m(a) & \text{for m odd} \end{cases} \tag{6.7}$$

where J_m is the m-th Bessel function. As the signal is spread over several harmonics, we need to perform a lock-in detection on at least 2 harmonics (odd and even) to recover amplitude and phase information. We can note also that some care should be taken regarding the best value of a, as a given amplitude of modulation can lead to a large signal value of J_m for m odd, but a small value for m even, and *vice versa*.

This is the principle of multiple lock-in amplifier detection at selected harmonic references (M-LIA) [101]. Here we propose a novel approach where all the harmonic content is used to recover amplitude and phase with a single, modified lock-in detection, refered to as Generalised Lock-in Amplifier (GLIA).

Here, we propose another approach where the signal is multiplied by two orthogonal references having the same set of harmonic frequencies as I_{mod}, namely $\cos(\phi_R)$ and

$\sin(\phi_R)$; where $\phi_R(t) = a\sin(\Omega t)$. As for the serrodyne modulation, this operation can be performed with an electronic multiplier and integrator:

$$X_{\phi_R}(I_{\text{det}}) = \frac{1}{\Omega t_{int}} \int_0^{\Omega t_{int}} I_{\text{det}} \cos(\phi_R)\, d(\Omega t), \tag{6.8}$$

$$Y_{\phi_R}(I_{\text{det}}) = \frac{1}{\Omega t_{int}} \int_0^{\Omega t_{int}} I_{\text{det}} \sin(\phi_R)\, d(\Omega t). \tag{6.9}$$

As long as the two references do not contain a DC term[2] the contribution from I_o can be ignored. Otherwise the DC term in the detected intensity, can be simply filtered out using a high pass filter. In both cases, the two integrals (Equations (6.8) and (6.9)) have analytical solutions obtained through Bessel Integral representation [130]. Considering that I_o can be simply removed, we obtain:

$$X_{a\sin(\Omega t)} = \alpha E_R E_S \cos(\phi_S) \qquad \alpha = (1 + J_o(2a))$$

$$Y_{a\sin(\Omega t)} = \beta E_R E_S \sin(\phi_S) \qquad \beta = (1 - J_o(2a))$$

In order to retrieve the unknown parameters ϕ_S and E_S, the two proportionality constants α and β must be analytically or numerically evaluated for each modulation function ϕ_R. In this way, all the available modulated power is used to recover the signal field information. Moreover, many phase modulation functions can be considered: sinusoidal, symmetric or asymmetric triangular functions, etc., regardless of the phase modulation amplitude a. In practice, sinusoidal phase modulation is probably the most useful since phase-modulators such as a piezoelectric exhibit a faster and better operation when driven with a pure sine compared to other modulation functions. However, other modulations can be considered in some situations, and examples are given in (sec. 6.2).

To make things more practical, the phase modulation depth a can be wisely chosen to correspond to a Bessel's function node (e.g. $a = 2.405\,rad$). So $\alpha = \beta = 1$ and we are back to the perfectly serrodyne case output without the fly-back induced noise.

In order to have more accurate measurements, while doing an experiment, the actual phase modulation $\phi_R = \phi_{\text{real}}$ can deviate from the required drive excitation. To account for this, the real phase modulation induced by the modulator can be fed directly to the numerical integrator. Usually, the real phase could be measured during the experiment, for example, using piezoelectric modulator equipped with strain gauges or other displacement sensors. Empirically, the integrals (6.8-6.9) are numerically evaluated with the measured ϕ_R in order to determine the proportionality constants.

[2]This depends on the value of the phase modulation depth a

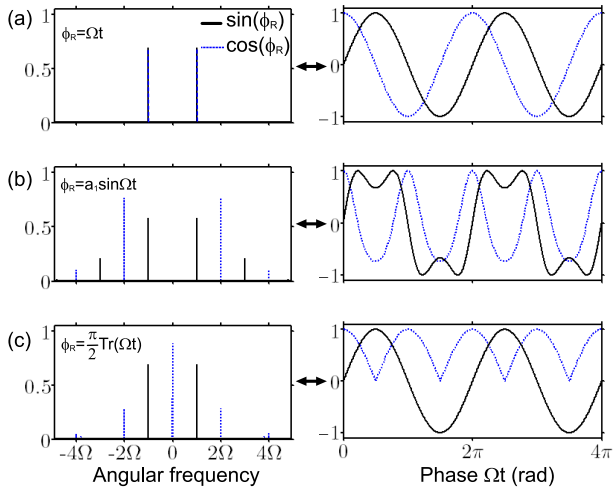

Figure 6.3.: Orthonormal reference signals ($\cos\phi_R$, $\sin\phi_R$) and their Fourier transforms for selected phase modulations $\phi_R(t)$: (a) Sawtooth with an amplitude 2π, (b) Sinusoidal with a phase amplitude a_1 corresponding to the first zero of J_0, and (c) Triangular with an amplitude of $\pi/2$ rad.

For any phase modulation amplitude a, the reference $\cos(\phi_R)$ may exhibit a non negligible DC component as can be seen in Fig. 6.3. Thus filtering the constant term I_0 by a simple DC filter can affect I_{mod}[3]. For this reason we evaluate the signal outputs for a filtered detected signal $\tilde{I}_{\text{det}}$:

$$X_{a\sin(\Omega t)}\left(\tilde{I}_{\text{det}}\right) = \tilde{k}_X E_R E_S \cos(\phi_S) \quad \text{with} \quad \tilde{k}_X = \left(1 + J_0(2a) - 2J_0^2(a)\right)$$
$$Y_{a\sin(\Omega t)}\left(\tilde{I}_{\text{det}}\right) = \tilde{k}_Y E_R E_S \sin(\phi_S) \quad \text{with} \quad \tilde{k}_Y = (1 - J_0(2a))$$

Where again the unknown parameters we are interested in, E_s and ϕ_s, can be determined directly, with:

$$E_s \propto abs\left(\frac{X\left(\tilde{I}_{\text{det}}\right)}{\tilde{k}_X} + i * \frac{Y\left(\tilde{I}_{\text{det}}\right)}{\tilde{k}_X}\right)$$
$$\phi_S = arg\left(\frac{X\left(\tilde{I}_{\text{det}}\right)}{\tilde{k}_X} + i * \frac{Y\left(\tilde{I}_{\text{det}}\right)}{\tilde{k}_X}\right)$$

Examples of orthonormal references $\cos(\phi_R)$ and $sin(\phi_R)$ are given in Fig. 6.3 for serrodyne Fig. 6.3 a), sinusoidal Fig. 6.3 b) and triangular Fig. 6.3 c) modulation in direct and frequency space.

[3]This is possible only if $< E_S^2 >$ is very small and we can consider $I_0 \simeq < E_R^2 >$.

6.2. Why it is Called G-LIA

We call the newly introduced method of detection "Generalized" Lock-in Amplifier because it is based on the lock-in amplifier detection principle (equations (6.8) and (6.9)); however it is generalized. In the sense that it does not restrict ϕ_R to single harmonic function, rather it could be an arbitrary modulation function. Here we present the G-LIA method in the case of triangle wave phase modulation:

6.2.1. Triangle Wave Phase Modulation

For a triangle wave modulation $\phi_R = aTr(\Omega t)$, the modified lock-in operation performed on the modulated intensity term $I_{mod} = 2E_R E_S \cos(\phi_S - \phi_R)$ (i.e. considering I_o is removed), the integral calculation give:

$$X_{aTr(\Omega t)}(I_{mod}) = k_X E_R E_S \cos(\phi_S) \quad \text{with} \quad k_X = \left(1 + \frac{\sin(a)\cos(a)}{a}\right)$$
$$Y_{aTr(\Omega t)}(I_{mod}) = k_Y E_R E_S \sin(\phi_S) \quad \text{with} \quad k_Y = \left(1 - \frac{\sin(a)\cos(a)}{a}\right)$$

where $Tr(\Omega t)$ is the triangle wave ranging from -1 to 1 in phase with $\sin(\Omega t)$. It is then convenient to choose a phase modulation a equals to a positive integer number times $\pi/2$ in order to obtain the same output as the ideal serrodyne given by (6.4-6.5), and simple reference signals cf. Fig. 6.3 c). Since generally I_{mod} can not be obtained by a DC filtering of the detected intensity I, it is more convenient to consider a modified lock-in operation on the filtered detected intensity $\tilde{I}_{det}$, we obtain:

$$X_{aTr(\Omega t)}\left(\tilde{I}_{\text{det}}\right) = \tilde{k}_X E_R E_S \cos(\phi_S) \quad \text{with} \quad \tilde{k}_X = \left(1 + \frac{\sin(a)\cos(a)}{a} - \frac{2\sin^2(a)}{a^2}\right)$$
$$Y_{aTr(\Omega t)}\left(\tilde{I}_{\text{det}}\right) = \tilde{k}_Y E_R E_S \sin(\phi_S) \quad \text{with} \quad \tilde{k}_Y = \left(1 - \frac{\sin(a)\cos(a)}{a}\right),$$

from wich amplitude and phase are also directly retrieved. The additional term $2\sin^2(a)/a^2$ is small for large values of the phase modulation amplitude a, or values close to an integer number times π, so that we can also have $\tilde{k}_X \simeq \tilde{k}_Y \simeq 1$.

6.3. Application Test on Monitored Movement

To assess the validity of our approach, a demonstration setup was built. Fig. 6.4 a) is a schematic of the mounted setup. In order to achieve a controlled phase modulation,

the reference mirror was mounted on a piezoelectric crystal. The reference mirror driving signal was set to be sinusoidal with angular frequency of 200 π rad/s and amplitude 2.4 rad.The signal arm was replaced by a movable mirror as well, this mirror was mounted on a piezoelectric material equipped with capacitive sensor in order to have the exact position (phase) as function of time.

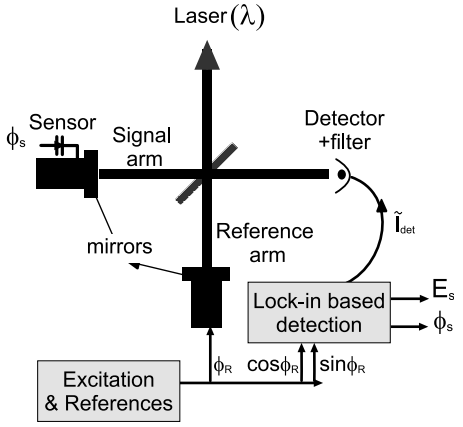

(a) A schematic Michelson interferometer operating with arbitrary phase modulation ϕ_R in the reference arm.

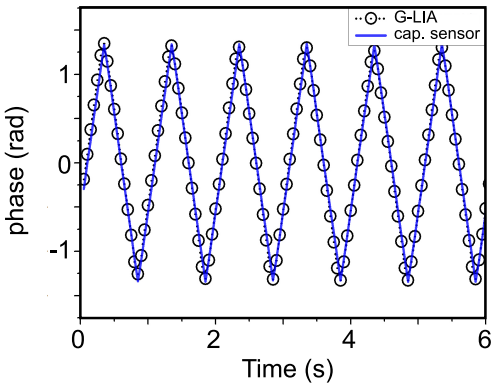

(b) Upon $\phi_R(t) = a\sin(\Omega)t$ The phase of the signal field follows a triangular function monitored by capacitive sensors (thick line) along with the instantaneous interferometric result in circles.

Figure 6.4.: Test and application of the G-LIA technique for measuring a displacement.

Fig. 6.4 b) shows the phase obtained by G-LIA method plotted in circles to that given by the gauge sensor plotted in a solid line. The phase given from the simultaneous interferometric measurements is obtained with an integration time of 0.05 s. A satisfactory agreement is noticed. Here we present the triangle phase modulation applied to the signal arm; however a remarkable agreement was observed for other modulations reasonnably achievable with the loaded piezoelectric actuator bandwidth. The used numerical integration was performed using LabVIEW [39], where the equations (6.8-6.9) were implemented. The detected signal I_{det} containing all the harmonics was filtered from its DC component by a high pass filter and the resulting signal $\tilde{I}_{\mathrm{det}}$ was sampled with a 16-bit acquisition card.

In NSOM imaging, the phase change ϕ_S in the signal field is not due to a displacement but is a due to a change in the field perceived by the tip apex. This can typically occur while the sample is scanned under the tip. A phase change can also occur if the illumination wavelength is changed: this results in a modification of the sample field or a change in the probe-sample interaction. In the next subsection we first consider a simple spectroscopic measurement using the G-LIA technique, by placing a gas cell in the signal arm.

6.4. Test and Application to Phase Resolved Spectroscopy

Reference cells contain vapors from specific atomic elements or molecular compounds, since each element has a well-defined absorption spectrum, these cells may be accurately used in spectroscopic applications such as tunable diode laser calibration, stabilization of laser frequencies, and calibration of wavelength meters. In our case we have tested the change in phase due to the absorption of iodine gas over few picometers using a tunable diode laser. Fig. 6.5 a) shows a setup similar to Fig. 6.4 a), where a single-mode laser diode operating near $\lambda = 650.0$ nm was used to perform phase-resolved spectroscopy.

A gas cell of iodine was added in the signal arm and the wavelength was tuned over few picometers across an absorption line of the gas with ramps of current. As for the previous experiment an arbitrary sine phase modulation was created in the reference arm (2000π rad/s, $a = 1.2$ rad) and amplitude and phase were retrieved through the G-LIA operation. The corresponding results are shown in Fig. 6.5 b). The observed magnitude and phase spectra actually reflect the expected variation of the real and imaginary parts of the gas refractive index across a Lorentzian absorption peak slightly convoluted with the source line-width.

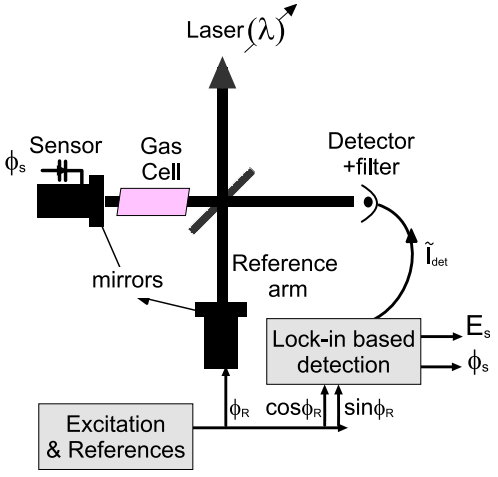

(a) Same setup as Fig. 6.4 a) with a gas cell in the signal arm and a tunable laser diode.

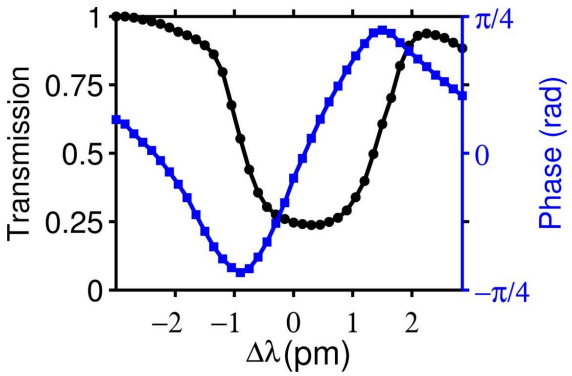

(b) Example of the obtained phase resolved spectroscopy.

Figure 6.5.: Application to phase resolve spectroscopy

6.5. Extension to Amplitude modulated signal

So far we have discussed the case where only the reference arm is being modulated. However in experiments with weak signal, it helps modulating the signal arm as

well. For example, most research groups working with aperture-less NSOM they scan the surface using tapping mode. This mode is chosen not only because it lessens the damage done to the surface and the tip but also because, as mentioned in section 3.2.2.2, it helps filtering out the useful signal from the huge background. So we have to consider such cases, where the signal arm goes under modulation of angular frequency Ω_A that is typically one or few order of magnitudes higher than the characteristic angular frequency Ω of ϕ_R.

This amplitude modulation acts as a frequency carrier and the sidebands shown in Fig. 6.3 will appear on each side of Ω_A (instead of DC frequency). One solution to handle this case is to perform a first "classical" LIA operation at the tip frequency with a very small integration time to shift all the sidebands above and below the DC frequency. Then the standard G-LIA, without amplitude modulation can be performed. However, to avoid this double step, references signals containing also sidebands centered on Ω_A can be used directly. This approach was implemented and is described hereafter.

To simplify the mathematical description, we note $\Omega_A{=}n\Omega$, where n is typically much greater than one. The part of the signal field modulated at Ω_A is then noted to be $E_P(t) = \sqrt{2}E_P \cos(n\Omega t)\cos(\Omega t + \phi_S)$. With this expression, the useful modulated term I_{mod} of relation (6.2) is now:

$$I_{mod} = 2E_R E_P \cos(n\Omega t)\cos(\phi_R - \phi_S), \tag{6.10}$$

that can be expressed as:

$$I_{mod} = E_R E_P \cos(n\Omega t + \phi_R - \phi_S) + E_R E_P \cos(n\Omega t - \phi_R + \phi_S), \tag{6.11}$$

to emphasize the presence of sidebands at frequencies above and below $n\Omega$, and to facilitate the analytical integral calculations. On the other hand, the term I_0 in Eq. (6.2) is:

$$I_0 = \text{const.} + {E_p}^2 \cos^2(n\Omega t) \tag{6.12}$$

As we can see this term carries no information about the needed quantities (E_S and ϕ_S) and exhibits a modulation at the frequency $2n\Omega$ only. Consequently, we can safely ignore I_0 as the reference signals that we will now consider don't have such frequencies in their spectrum. As before, we multiply the detected intensity by the two orthogonal reference signals:

$$C(t) = 2\cos(n\Omega t)\cos\phi_R = \cos(n\Omega t + \phi_R) + \cos(n\Omega t - \phi_R)$$
$$S(t) = 2\cos(n\Omega t)\sin\phi_R = \sin(n\Omega t + \phi_R) - \sin(n\Omega t - \phi_R)$$

These two orthogonal reference signals have the same set of frequencies as I_{det}, upon integration we get:

$$X_{n\Omega t\pm\phi_R}\left(I_{\text{det}}\right) = \frac{1}{\Omega t_{int}}\int_0^{\Omega t_{int}} I_{\text{det}} C(t)\, d(\Omega t) \propto E_S \cos\left(\phi_S\right), \tag{6.13}$$

$$Y_{n\Omega t} \pm \phi_R\left(I_{\text{det}}\right) = \frac{1}{\Omega t_{int}}\int_0^{\Omega t_{int}} I_{\text{det}} S(t)\, d(\Omega t) \propto E_S \sin\left(\phi_S\right). \tag{6.14}$$

For the sinusoidal phase variation case ϕ_R, the two integrals then have simple analytical solutions obtained from the integral representation of n-th Bessel functions:

$$X_{n\Omega t\pm a\sin(\Omega t)}\left(I_{\text{det}}\right) = E_R E_P \cos\phi\left(1 + J_{2n}(2a) + J_0(2a)\right), \tag{6.15}$$

$$Y_{n\Omega t\pm a\sin(\Omega t)}\left(I_{\text{det}}\right) = E_R E_P \sin\phi\left(1 - J_{2n}(2a) - J_0(2a)\right). \tag{6.16}$$

Amplitude and phase are then retrieved directly from these two outputs for any phase modulation amplitude a. We note that $J_{2n}(2a)$ is actually negligible for large values of n and reasonable phase modulation amplitude a (for example for $n = 10$ and $a < \pi$, or $n = 20$ and $a < 6\pi$, in the typical cases $n = 30$ since the natural frequency of a tuning fork about $30\,krad/s$ while the frequency of the signal driving the reference mirror is $1\,krad/s$). It is therefore convenient in this case to choose a modest phase modulation a such that $J_0(2a) = 0$, so that the outputs are again identical to the perfect serrodyne case given by Eqs. (6.4-6.5).

6.5.1. Demonstration Experiment

To experiment and assess the quality and precision of the phase calculation in the case where we have a very weak signal. Such cases where modulating the signal arm field is mandatory. We mounted a tuning fork at the place of the signal mirror in a Michelson interferometry. Fig. 6.6 a) is a schematic of the implemented set up, where the tuning fork was set to vibrate at $\Omega_{TF} = \Omega_A$ and the reference mirror by a sinusoidal one $\phi_R = a\sin(\Omega t)$. In this way the signal intensity $< E_S^2 >$ is sinusoidally modulated and therefore the signal field also presents modulation at the frequency Ω_A and its harmonics. The tuning fork was mounted on a piezoelectric crystal that is moved back and forth in a controlled triangular motion ($\pm 0.80\,\mu$m corresponding to ± 1.0 rad). To recover the corresponding signal phase, the reference phase modulation $\phi_R = a\sin(\Omega t)$ and the tuning fork excitation signal proportional to $\sin(\Omega_A t)$ were used to build the references C(t) and S(t). Fig. 6.6 b) shows the corresponding phase measurement obtained with such an extended G-LIA method, as we can notice again an accurate phase was retrieved proving the validity of the approach.

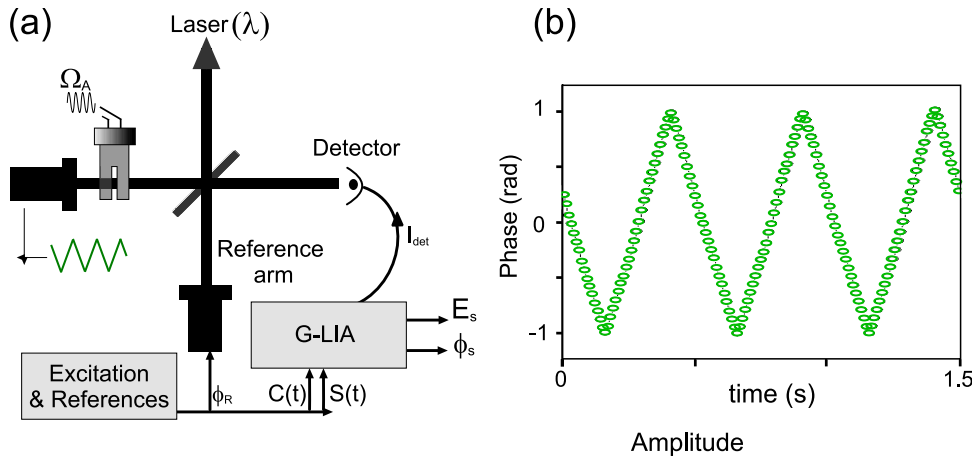

Figure 6.6.: a) Michelson interferometer with double modulation (the reference arm and the signal arm). b) The obtained phase of the movement of a bare tunning fork

The labVIEW interface that corresponds to a typical experiment described in Fig. 6.6 a) is shown in Fig. 6.7. Where in the signal arm we have place a bare tuning fork. The interference pattern (on the top oscilloscope graph) shows both the modulation of the reference mirror as well as that of the tuning fork. Most interestingly is the oscilloscope graph showing the two concentric circles. Actually the circle with bigger radius corresponds to the case of unmodulated signal arm, and that with smaller radius to a modulated one. The circle depicts the constant amplitude and changing phase. The idea of showing it in a circular form: One, to verify the stability of the system. Two, to assure us that we are choosing the correct driving amplitude of the reference arm to have a Bessel's function node in equations (6.15,6.16). Furthermore the other two oscilloscope graphs show the variation of the phase and amplitude, so that we can monitor these variables while doing an experiment.

6.5.2. Background Elimination

Unmodulated background elimination In several cases we have an unwanted electric field signals impinging on our detector. This signal can be comparable or stronger than the modulated signal field $E_P(t) = \sqrt{2}E_P \cos(n\Omega t)\cos(\omega t + \phi_S)$. If we consider having such a coherent background signal, in addition to $E_R(t)$ and $E_P(t)$, we have:

$$E_{Bg}(t) = \sqrt{2}E_{Bg}\cos(\omega t + \phi_{Bg})\,.$$

This constant background field can interfere with $E_P(t)$ and gives an additional "unwanted" intensity term modulated at radial frequencies $n\Omega$:

$$I_{mod}^{Bg} = 2E_{Bg}E_P \cos(n\Omega t)\cos(\phi_{Bg} - \phi_S)\,. \tag{6.17}$$

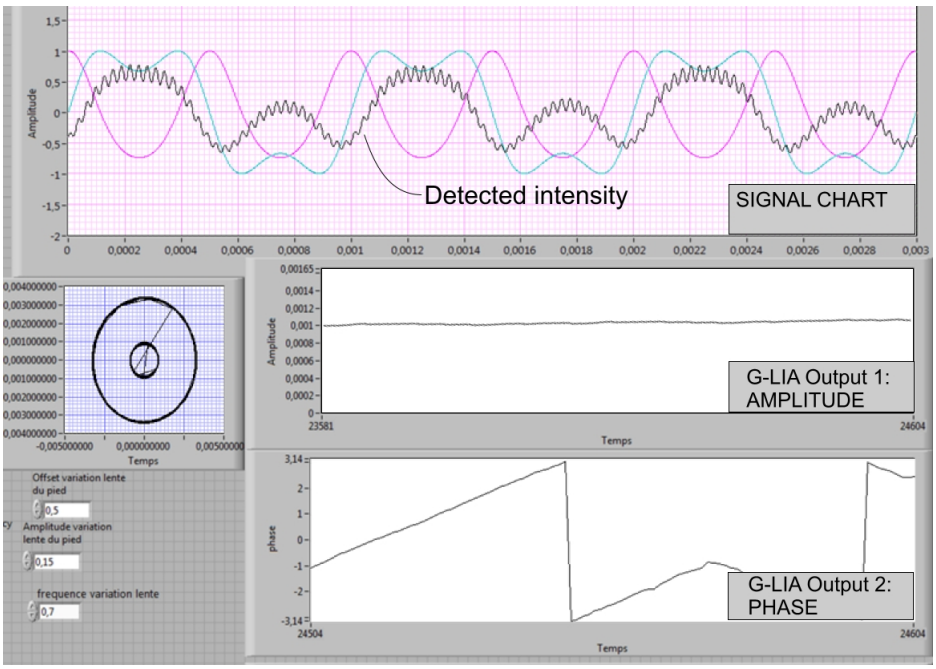

Figure 6.7.: LabVIEW interface developed for amplitude and phase measurement in NSOM. The intensity shown in the signal chart was obtained on the mid-IR NSOM focusing on a bare oscillating tuning fork. Top: Detected intensity (black curve) when reference mirror and the fork are oscillating at about $1kHz$ and $32kHz$ respectively. The LabVIEW generated signals $cos\,(\phi_R)$ (in blue) and $sin\,(\phi_R)$ (in pink) are used in the G-LIA references C(t) and S(t) to provide the amplitude E_S and phase ϕ_S outputs. The circles represent the signal $E_S\,exp\,(i\phi_S)$ in the complex plane as ϕ_S is varied via a sawtooth-type displacement. The large circle is the signal obtained when the fork is not oscillating and that $sin\,(\phi_R)$ and $cos\,(\phi_R)$ are used as references. The small circle is obtained when the fork is oscillating with $C(t)$ and $S(t)$ as references.

Since $C(t)$ and $S(t)$ also have frequency components at $n\Omega$, we have to evaluate the contribution of this term in the extended G-LIA operation:

$$X_{n\Omega t\pm\phi_R}\left(I_{mod}^{Bg}\right) = \frac{1}{\Omega t_{int}}\int_0^{\Omega t_{int}} I_{mod}^{Bg} C\,(t)\;d(\Omega t) \tag{6.18}$$

$$Y_{n\Omega t\pm\phi_R}\left(I_{mod}^{Bg}\right) = \frac{1}{\Omega t_{int}}\int_0^{\Omega t_{int}} I_{mod}^{Bg} S\,(t)\,d(\Omega t). \tag{6.19}$$

The contribution of these two integrals are found to be proportional to $J_{2n}(a)+J_0(a)$. From this result we see that the contribution of the unwanted terms modulated at $n\Omega$ can be canceled out by setting a modulation amplitude a corresponding to a zero of the $0th$ Bessel function, $J_{2n}(a)$ being extremely small for a sufficiently large n.

It is worth noting that the additional unwanted interference term between $E_{Bg}(t)$ and $E_R(t)$, and the self interference term proportional to E_{Bg}^2 are not modulated at $n\Omega$, and are therefore efficiently filtered without special precaution.

Modulated background attenuation Part of the background can be modulated by the tip oscillation. In this case it cannot be fully suppressed, as the principle of background cancellation we have presented is based on the fact that it is not modulated (producing a peak at $\Omega_A = n\Omega$ only, mute for specific a). When the background is modulated at tip frequency, the two fields are not fully distinguishable. However the modulated background can be reduced by:

- using sharp tips with a small body section as we do in our experiment (sharply etched tungsten probe).

- reducing the amplitude of oscillation, e.g. at few nanometers: since the background correspond to radiation mode, its variation is very small over few nanometer is very small. Therefore the interference between background and reference field will not produce noticeable sidebands (any contribution at $\Omega_A = n\Omega$ is still filtered).

- detecting the sidebands centered on higher tip frequency harmonics, i.e at $\Omega_A = k \times \Omega_{tip}$ with k integer. The result is similar to the previous recommandation: since the background has a rather linear variation with the vertical probe position (by opposition to evanescent fields that are highly non linear[4]), its amplitude modulation is mainly sinusoidal. On the other hand, the near-field signal has typically non linear variations able to generate higher harmonics. The G-LIA can be set to operate at higher harmonics without difficulty by increasing n in the reference signals by a factor k.

6.5.3. Double Generalized Lock-in Detection

In our near-field experiment, the-GLIA can be used directly as described in the previous section. However, we have considered that the amplitude modulation due to the tip oscillation at the tip angular frequency $n\Omega$ is proportional to a sinusoidal function like $\cos(n\Omega t)$. In practice, this function typically corresponds to the driving signal fed to the probe. It is clear that, in general, a phase shift exists between the driving signal and the actual probe motion. In the worst case, which is not unlikely, the probe oscillation can be completely out of phase with the driving signal, depending on the type of probe (cantilevered or attach to a tuning fork) and the mechanical sample characteristics. There are several options to solve this issue. The simplest is sometimes to measure the actual probe motion[5] and to use this signal

[4]The extension of the evanescent waves related to the probe are in the order or smaller than the tip diameter)

[5]This is often possible. For example using the so called "A minus B" signal provided by commercial AFM where the oscillation is monitored with a four (or two) quadrant photodiode.

(normalized) instead of the driving signal. Another approach is to perform a *double G-LIA*, first using references with a $cos(n\Omega t)$ amplitude modulation, then using reference with a $sin(n\Omega t)$ amplitude modulation. This improvement is described hereafter.

We consider an amplitude modulated signal field $E_s(t)$ at an angular frequency $n\Omega$, where Ω is still the phase modulation frequency. In general, the amplitude modulation of this field can be phase shifted with respect to the excitation signal. We denote by $E_s(t) = E_s^{\text{full}}(t)\cos(\omega t+\phi_s)$ the full signal field. A quite general expression for the modulated amplitude is $E_s^{\text{full}}(t) = \text{const.} + E_s\cos(n\Omega t+\psi) + \text{harmonics}$. The phase ψ accounts for the eventual phase shift existing between the fundamental term $E_s\cos(n\Omega t+\psi)$ and the driving signal in phase with $\cos(n\Omega t)$. To obtain an optimal determination of the amplitude and phase (E_S, ϕ_S) without knowing ψ, the G-LIA can be applied twice as part of the fundamental term is modulated proportional to $\cos(n\Omega t)$ and the other part proportional to $\sin(n\Omega t)$:

$$X = \int_0^{t_{max}} I_{det}\cos(n\Omega t)\cos(\phi_R)dt \quad \text{and} \quad Y = \int_0^{t_{max}} I_{det}\cos(n\Omega t)\sin(\phi_R)dt$$

$$X' = \int_0^{t_{max}} I_{det}\sin(n\Omega t)\cos(\phi_R)dt \quad \text{and} \quad Y' = \int_0^{t_{max}} I_{det}\sin(n\Omega t)\sin(\phi_R)dt$$

Evaluation of the terms gives:

$$X = k_X E_R E_s\cos(\psi)\cos(\phi_s) \qquad \text{and} \qquad Y = k_Y E_R E_s\cos(\psi)\sin(\phi_s),$$

$$X' = -k_X E_R E_s\sin(\psi)\cos(\phi_s) \qquad \text{and} \qquad Y' = -k_Y E_R E_s\sin(\psi)\sin(\phi_s),$$

where k_X, k_Y are the already known proportionality constants corresponding to a sine phase modulation in Equations (6.15) and (6.16). The amplitude, the phase ϕ_s but also the unknown phase shift ψ are then calculated from these four outputs. This is this "full" G-LIA that has been implemented.

6.5.4. Error, Background suppression and signal to Noise Ratio

In order to compare theoretically G-LIA while operated under sinusoidal signal with M-LIA, parametric simulations were done considering software simulated signals. The Fig. 6.8 presents the results of these analysis:

- Fig. 6.8 a) shows the error on the retrieved phase depending on the value of n (where n is the ratio between the tip and mirror frequencies). The G-LIA method, where we integrate over a integer number of periods, works very well for the quasi integer values of n, or for any large enough real value of n. In practise n is large enough to do not worry about its exact value.
- Fig. 6.8 b) presents the background attenuation depending on the selected value of the phase modulation depth a. As can be seen, the value must quite precisely fixed at one of the zero of the Bessel function.
- Fig. 6.8 c) gives a comparison of the signal level using G-LIA or MLIA on two harmonics. The signal is obviously higher with the G-LIA since all the harmonic contents is used.

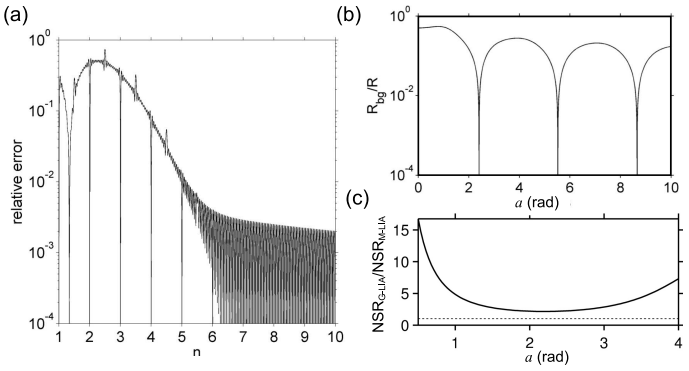

Figure 6.8.: (a) Example of simulated relative error on the phase using G-LIA detection for increasing real values of n. The simulation was made with $\phi_S = \pi/4$, $\Omega t_{int} = 20\pi$, a sampling interval equals to $2\pi/1000$, and $a = 3$. (b) Background field attenuation for increasing values of a and identical background and modulated signal fields values. In this simulation, $n = 30$, $\Omega t_{int} = 20\pi$, and the sampling interval is equal to $2\pi/1000$. The background contribution drops to zero for a corresponding to a zero of $J_0(a)$ and large n. (c) Simulated comparison of the signal level between G-LIA and a M-LIA approach where the two first sideband harmonics are detected ($\Omega_A + \Omega_R$, $\Omega_A + 2 * \Omega_R$)

6.6. Conclusion

In conclusion we have described a modified lock-in detection method to recover amplitude and phase in optical interferometers, where the reference beam can be non linearly modulated in phase or frequency. This method is optimum in the sense that it fully exploits the detailed spectrum of the detected beating between signal and reference, thus providing the highest signal to noise ratio possible. The principle was detailed for sinusoidal and triangular phase modulations and was experimentally tested, showing high stability and reliability. The method was extended to

amplitude-modulated signals in the common case of a sinusoidal phase modulation. This second approach is useful in the the case of very low signal experiments. We will show the results of its application to NSOM in the next chapter. In addition, the conditions to obtain efficient background light suppression in this second approach were derived. Although the tests were made using vibrating mirrors, much faster phase modulation can be achieved, for example using a slight wavelength modulation of the laser source in an unbalanced interferometer.

6.6.1. Summary Table

To summarize the modulation types that were mentioned and the corresponding values of the proportionality constants (k_X, k_Y) and $(\tilde{k}_X, \tilde{k}_Y)$, here we present a compact summary table (Fig. 6.9).

Modulation Functions		References	G-LIA on I_{det}		G-LIA on $\tilde{I}_{det}$
Phase $\phi_R(t)$	Amplitude $f(t)$	(X, Y)	(k_x, k_y)	Condition	$(\tilde{k}_x, \tilde{k}_y)$
Ωt	-	$\cos\phi_R$, $\sin\phi_R$	1, 1	-	1, 1
$a\ \sin(\Omega t)$	-		$1+J_0(2a)$, $1-J_0(2a)$	$J_0^2(a) \approx 0$	$k_x-2J_0^2(a)$ k_y
$a\ Tr(\Omega t)$	-		$1+2\,\mathrm{sinc}(2a)$ $1-2\mathrm{sinc}(2a)$	$\mathrm{sinc}^2(a) \approx 0$	$k_x-\mathrm{sinc}^2(a)$ k_y
other	-		analytic or numeric evaluation	No DC term in the references	analytic or numeric evaluation
Ωt	$\cos(n\Omega t+cte)$	$2f(t)\cos\phi_R$, $2f(t)\sin\phi_R$	1, 1	The contribution of un-modulated background light interfering with the modulated signal is canceled if the references are not modulated at the frequencies of f(t). ($J_o(a)=0$ for a sine modulation)	
$a\ \sin(\Omega t)$	$\cos(n\Omega t+cte)$		$1+J_{2n}(2a)+J_0(2a)$, $1-J_{2n}(2a)-J_0(2a)$		
other	other		analytic or numeric evaluation		
Modulation Functions		References	G-LIA on I_{det}		
Phase $\phi_R(t)$	Amplitude	(X, Y, X', Y')	(k_x, k_y, k_x', k_y')		
$a\ \sin(\Omega t)$	$\cos(n\Omega t+\psi)$ ψ unknown	$\cos(n\Omega t)\cos\phi_R$, $\cos(n\Omega t)\sin\phi_R$, $\sin(n\Omega t)\cos\phi_R$, $\sin(n\Omega t)\sin\phi_R$	$(1+J_{2n}(2a))\cos\psi$, $(1-J_{2n}(2a))\cos\psi$, $-(1+J_{2n}(2a))\sin\psi$, $-(1-J_{2n}(2a))\sin\psi$	The 4 unknowns (Es, ϕ_s, $\cos\psi$, $\sin\psi$) are retrieved inambigously from the 4 outputs X, Y, X', Y'	

Figure 6.9.: Summary table

7. Mid-IR Nanoscopy of LSPR

The interest in investigating surface waves like surface plasmon polariton and surface phonon polariton comes from their potential applications in bio-sensing[18, 138, 8], Surface Enhanced Raman Spectroscopy (SERS)[96, 72], Surface-Enhanced Infrared Absorption Spectroscopy (SEIRA)[7, 6, 23]. These applications are based on the local, intense, interaction between the SPP/SPhP *localized* on the nanostructures and the material to be detected. So determining the local electric field distribution and the local dielectric function is of quite importance. The only optical technique that enables this information is NSOM; since this can only be done through a local interaction with the structures. In this chapter, we will focus on the experimental determination[1] of the field distribution in highly doped InAsSb grating.

First, we introduce the experimental setup and we present results obtained on two "test" samples in order to evaluate the validity of our developed detection method. These samples consist in Cu/Si and polymer/Gold sub-wavelength gratings. Then, we present phase-sensitive near-field imaging on the highly doped semiconductor gratings. A first local spectroscopy study over the available laser range was performed. Electromagnetic simulations are conducted and compared to the experimental ones.

7.1. Experimental Setup

Fig. 7.1 a) is a top view picture of the home-made NSOM mounted on an optical table inside a thermally isolating box. Fig. 7.1 b) depicts schematically the procedure. This set-up is operated in the mid-IR; however for practical reasons the infrared laser was aligned with a He-Ne laser. The used source is a tunable infrared Quantum Cascade Laser [136] with a rather low but highly stable power. The QCL spectral range is 10 to10.5 μm, with maximum power of about 70 mW. The laser polarization was set along the probe axis with an adjustable incident angle, typically ranging from 45° to about 60°. An aberration-corrected and diffraction limited Schwarzschild objective in the signal arm was used to tightly focus the beam on the tip apex[2]. The tip is of typical diameter of 30 nm fabricated by electrochemical etching of tungsten

[1] This chapter is mainly experimental, details about the nature of NSOM signal and how the local field is detected is detailed in appendix.

[2] Focus spot size is about λ^2 as measured by an IR-camera.

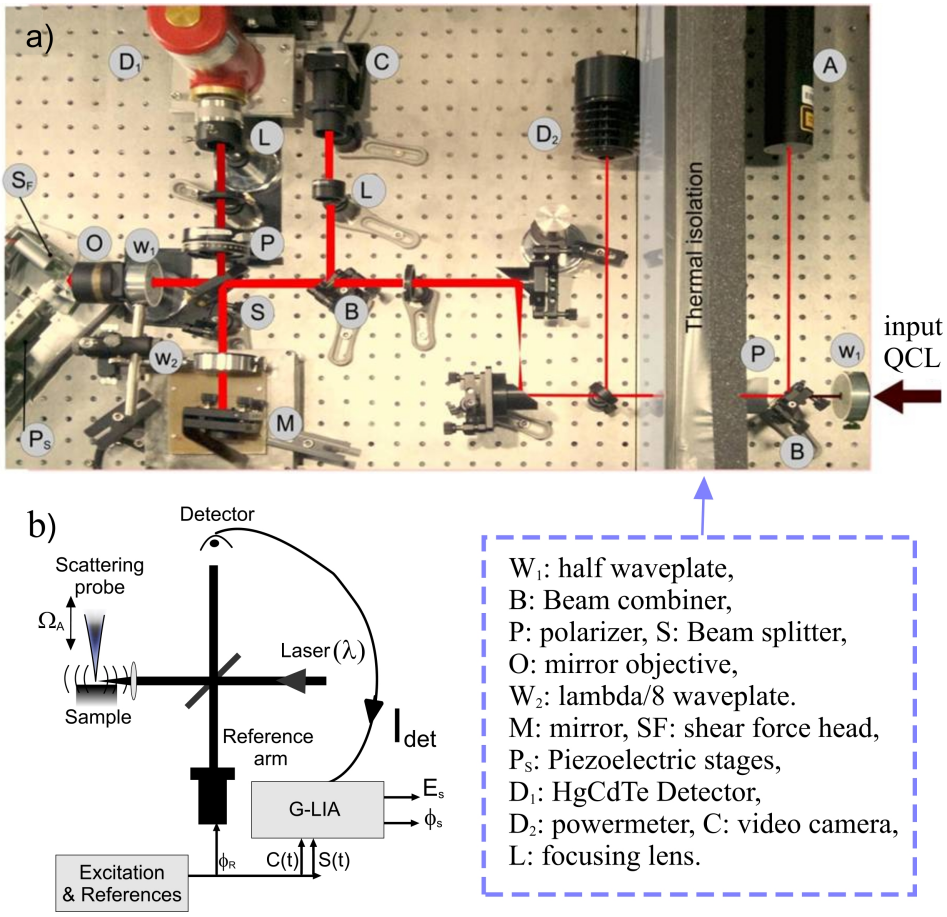

Figure 7.1.: NSOM home-built setup (a) top view picture, (b) Schematic of the procedure.

wire (detailed procedure explained hereafter). The tip is glued on a commercially available tuning forks and the scanning is conducted in tapping mode.

An electric excitation is supplied by a phase-locked loop (from Nanonis) and an additional feedback loop enables to keep a constant amplitude. The sample is scanned by 3D-piezoelectric actuators with respect to the tip which is fixed in the focus point of an objective. The objective is used to collect the back-scattered electric field. A cooled HgCdTe detector (from Teledyne Judson Inc.) is used to detect the signal and send the photocurrent to our acquisition card[3]. The G-LIA detection method was used to retrieve the phase and amplitude of the scattered/collected signal.

[3]the acquisition card featuring high resolution of 22 bit to offer the performance level of a high quality digital LIA. The 22 bit card offers a resolution of 2.38×10^{-7} this is important since in a NSOM experiment we can have a strong signal that verifies slowly.

7.1.1. Probe Fabrication

The idea of electrochemically etched probes using "double lamellae dropoff technique" was inspired from M. Kulawik et al. work [74]. However a parametric study was conducted at LNIO by Z. Sedaghat in order to find the optimum conditions to have the required tip-diameter [114]. The used setup is sketched in Fig. 7.2 a). We started with a 125 μm diameter tungsten wires bought from Goodfellow. The wire was glued to a commercial AFM tuning fork and was partially immersed in NaOH solution. The voltage was used to promote the reaction between the tungsten and the NaOH solution. When the etching process is complete, the tungsten wire is cut and the current goes to zero (due to the open circuit). The capillary effect in liquids made the etching process result in sharply etched probes[4].

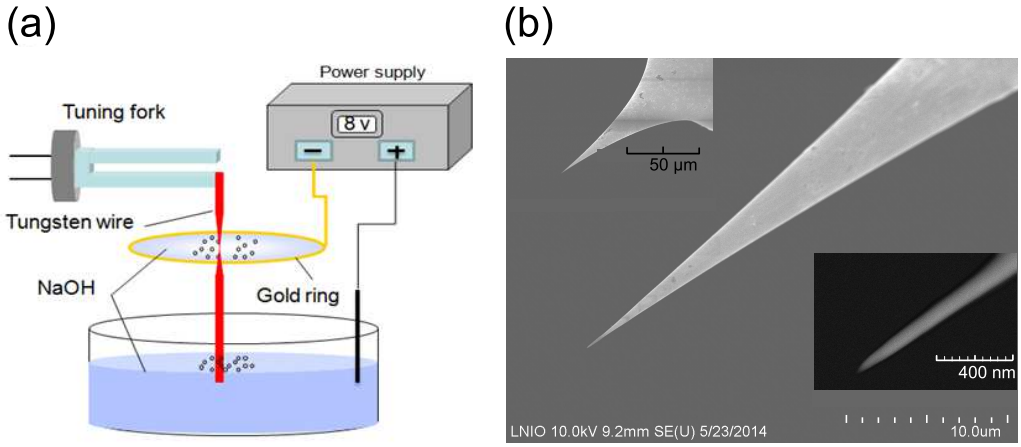

Figure 7.2.: Probe fabrication by electrochemical etching, (a) set-up sketch, (b) SEM images of a typical etched probe.

The used probe fabrication method is quite reproducible, Fig. 7.2 b) shows a SEM of a typical probe. As we can see the tip shape is symmetric with a half angle of about 10° and the tip end diameter, as mentioned, is about 30 nm [5].
We point out here that the small size of the probe body and the absence of cantilever is useful to strongly reduce eventual background light modulation. To filter further the background, ultra-small oscillation amplitude for the probe was used[6]. This unconstrained the necessity to use detection at the probe's higher harmonics[7]

[4]The etching parameters that were used, taken from [114], 3 molar NaOH solution and voltage of 8 V for a gold ring of about one 8 mm in diameter. The etching process typical time is 4 to 5 minutes. Moreover, the effect of using another solution like KOH was also investigated by Z. Sedaghat.

[5]Fluctuations exist from a probe to another but the diameter is typically comprised between 20 nm and 40 nm.

[6]Probe oscillation amplitude typically $\leq$ 5 nm, as measured by interferometry with G-LIA.

[7]As mentioned in the previous chapter, the G-LIA can detect the signal at the k^{th} harmonic of the probe oscillation frequency by setting $\Omega_A = k \times \Omega_{tip}$, i.e. by multiplying the n factor by k. This would be usefull for larger tip oscillation amplitudes.

frequencies [10, 111] often required to suppress modulated background light, the two approaches being actually nearly equivalent [27, 115]. The setup was built to operate in the mid-IR range where the scattering cross-section is essentially low.

7.2. NSOM signal

A detailed introduction to the scattering NSOM signal is given in Appendix B. Here, we shortly highlight the most important features to discuss the observed result in the next sub-section. The basic principle of this nanoscopy is to illuminate a probe with small diameter (small in comparison to the wavelength of the illuminating source), and to closely scan the sample under investigation. The idea is then to collect the scattered electric field, since it results from the near-field interaction between the probe and the sample; thus carrying the needed information about the sample. Being able to resolve the phase and amplitude of the scattered field enables us to fully recover sample's properties.

To investigate the signal collected by NSOM, the electrostatic model has been widely used[8]. The simplest form of this model is when we consider the probe as being an isotropic sphere with radius r and we consider the scattered field E_s as proportional to an effective tip polarizability α^{eff}. Also the simplest case is to assume that the external field E_0 as being the sum of the incident field E_i and its reflection $r_p E_i$, where r_p is the Fresnel reflection coefficient. When we consider the field wich is backscattered from the probe toward the detector, as we do in our experiment, we can obtain the following expression for the scattered intensity (Discussed in detail in (Appendix B), equation (B.14)).

$$I_{\text{scat}}(\theta) \propto \left|\alpha_{\perp}^{\text{eff}}\right|^2 \sin^2(\theta) \left|1 + r_p\right|^2 \left|E_i\right|^2 \tag{7.1}$$

where θ is the scattered field direction, and E_i is the magnitude of the field[9] illuminating the probe, considered along the vertical direction (along the tip axis), direction along which the probe polarizability is higher. The main local near-field interaction is embedded inside the effective probe polarizability along the vertical direction (cf. equation B.11, page 118):

$$\alpha_{\perp}^{\text{eff}} = \frac{\alpha_t}{1 - \frac{\alpha_t \beta}{16\pi(r+z)^3}}$$

which is function of the complex valued probe polarizability[10] α_t and the reflection coefficient in the electrosatic limit β:

$$\beta = \frac{\epsilon_s - 1}{\epsilon_s + 1}$$

[8] Finer analysis naturally requires full electromagnetic simulation of the NSOM experiment.

[9] E_i is sometimes considered as equal to $(1 + r_p)E_o$, where E_o is the forward incident considered in this case as being simply reflected by the surface.

[10] For a small scattering sphere the polarisaility can be expressed as $\alpha_t = 4\pi r^3 \frac{\epsilon_t - 1}{\epsilon_t + 2}$

z is the probe-sample distance, ϵ_s is the permittivity of the sample and ϵ_t the permittivity of the tip. This simple model works well to grasp the fundamental existing phenomena. What we can infer from this model is that a stronger signal is obtained for small value of the denominator $D = 1 - \frac{\alpha_t \beta}{16\pi(r+z)^3}$, i.e for:

- large tip polarizability
- small distance
- large β value

Typically, a stronger signal is obtained on a nearly perfect metal (β is close to unity) compared to dielectrics, and dielectric with high permittivity should also provide a stronger signal. When small D value is obtained due to large β value, we talk about sample-induced resonance. While tip-induced resonances are invoked when a high signal is due a resonance in the tip polarizability. However we should note that, in principle having both high tip polarizability, β value together with a small distance can result in very small denominator value, and eventually sign inversion for α_{eff} and smaller signal. This is illustrated in Fig. B.3.

7.3. Measurement on Oxidized Copper/Silicon Grating

As a first example of phase sensitive nanoscopy measurement, we have studied a sub-wavelength surface grating made of copper lines embedded in silicon as depicted in Fig. 7.3 b).

The grating is made of 240 nm wide Cu lines with 6 μm spacing. Fig. 7.3 b) shows a highly resolved NSOM image, where the two copper lines imaged in the mid-infrared are clearly visible, both in the amplitude (dark lines) and in the phase (bright lines). From equation (7.1) we see an increased effective polarizability of the probe over metals in comparison to dielectric, one could expect the copper lines to appear in bright contrast, as previously reported in literature[5]. This brings back the results that were obtained previously using a homodyne version of our home-built NSOM experiment with CO_2 laser, Fig. 7.3. This figure reports on two cases, one using a scanning probe with a big diameter 100 nm, where the copper lines have their expected contrast. The second case is upon scanning with a very sharp probe (diameter $\leq$ 30 nm). In the second case we see a contrast inversion. Such contrast was only accounted by simulation if very high tip polarizabilies are considered, higher than expected from simulations using the bulk tungsten permittivity. An interpretation of this contrast inversion could be that, given the size of the probe, phonon confinement effects could also play an important role, and could impact the permittivity of the probe and consequently the observed signal [64, 114]. This phonon confinement was proven to have huge effect on the permittivity of Si NW [64] and might be responsible for the increased polarizability over the dielectric. Another

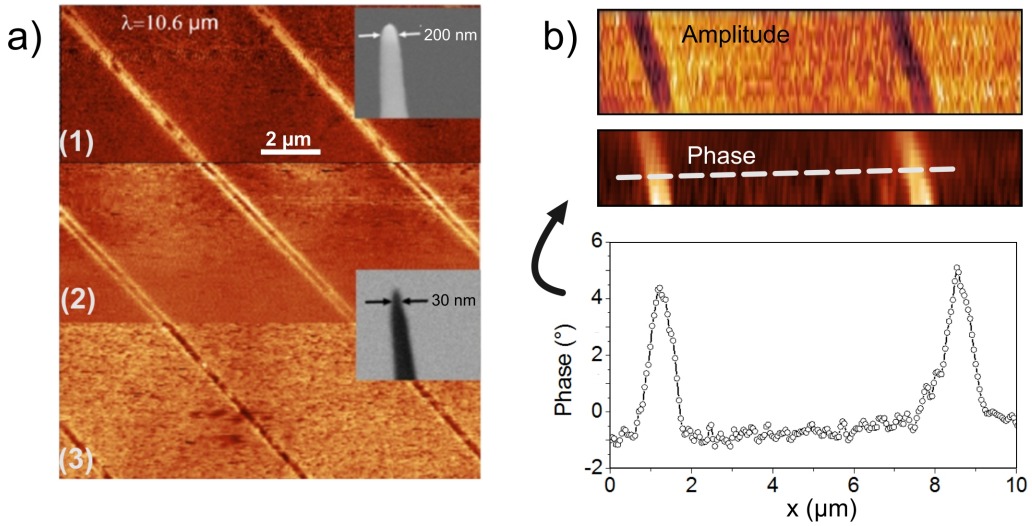

Figure 7.3.: NSOM experiments a) Homodyne NSOM performed with a CO_2 laser for (1) rounded tip (2,3) very sharp probe size (b) G-LIA detection method with QCL NSOM, amplitude and phase of the signal field scattered by the nano-probe on oxidized copper lines embedded in Si (sample 1). The phase profile along the white dashed line is plotted below (raw signal averaged on 5 lines).

possibility is that usually Cu material is easily oxidized and the sample was kept in ambient temperature/pressure conditions. So with no special precaution conditions, the Cu lines in the sample were slightly oxidized (native oxidation). A sharp tip is naturally more sensitive to the permittivity of the first sample nanometers.

7.4. Measurement on a Reference Sample: Gold/polymer Grating

The previous study showed important variations from one probe to another if the diameter is changed. In order to obtain more than qualitative information on a sample, it is important to determine the probe response. If we consider the simple model given by Equation ((7.1)), it means we need to determine the polarizability α_t, which is in principle possible if the complex scattered field is evaluated and if the other parameters are known. In this section, we present a NSOM experiments done on the sample depicted in Fig. 7.4 with the aim to estimate α_t.

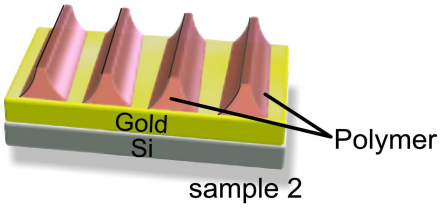

Figure 7.4.: A sketch of the fabricated gold/polymer grating.

Fabrication This sample was fabricated at UTT-LNIO by A. Rumyantseva, where a gold layer (120 nm) was deposited on silicon substrate by thermal evaporation. A layer of a positive photo-resist was then spin coated and an interferential optical lithography was applied. This technique leads to polymer removal at the bright interference fringe and polymer survival at dark interference fringe.

Sample interest A convenient aspect of using such positive resist is that its refractive index [11] in the $10-11\,\mu$m range was found to be very close to unity[12]. In consequence, the sample can be simply modeled as a single gold-air interface[13] where the polymer topography enables the determination of the probe sample response at controlled reproducible distances, without damaging the probe.

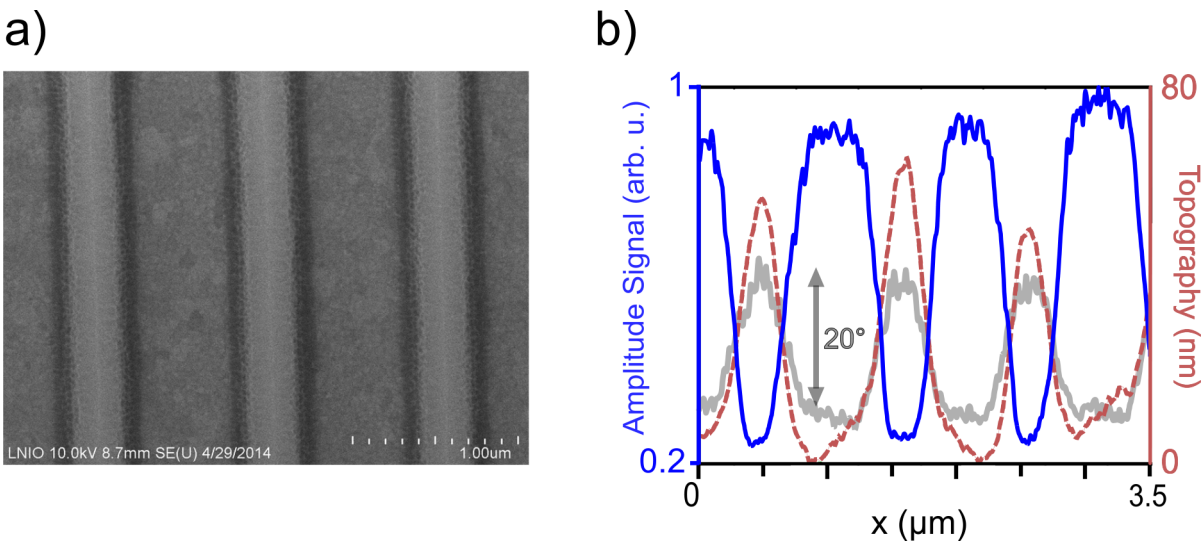

Figure 7.5.: Gold polymer studied grating, a) SEM image of the fabricated sample b) Amplitude (blue), phase (gray) and topography (dashes) profiles obtained across the gold/polymer grating surface (sample 2) showing a fast signal drop when the gold-probe distance increases.

Measurement and tip polarizability estimation Fig. 7.5 a) shows a SEM image of the studied sample. Fig. 7.5 b) are extracted profiles from the simultaneously obtained three images: topography, amplitude and phase. The measurements were

[11] Determined as in section II with far-field spectroscopy and by ellipsometry. Ellipsometric measurement was undertaken on thick bulk pellet at Université de Lorraine, LCP-A2MC, in the Ellipsométrie group.

[12] The best estimate near $\lambda = 10\mu$m was found to be $n = 1.05 + i\,0.02$ with a very small dispersion. Since the refractive index is close to the environment (air), the measurement uncertainty is however rather large (about 0.10).

[13] The probe response is not affected by the underlying Silicon substrate, given the gold layer thickness. Gold can be considered a quasi-perfect metal at these wavelengths.

conducted at a source wavelength of 10.2 μm, as we can notice there is a fast signal drop/increase (on a lateral scan displacement of about 20 nm) when the probe is approaching or lifting the sample.

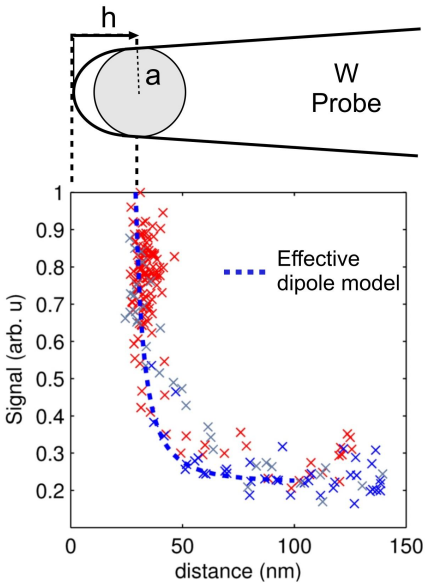

Figure 7.6.: Reconstructed approach curve on polymer/gold grating from profile datapoints (Crosses). The effective dipole model is represented in dashed blue. It considers an effective sphere of radius $a = 20\,nm$, positioned at $h = 1.5\,a$ above the tip apex.

From several similar profiles, we can recover the signal as a function of the probe height as given by the topography. The Fig. 7.6 shows several sample of data points in the vicinity of the polymer bumps. To account for the observed shape the tip polarizability α_t was varied to obtain a correct fit of the data. The fit on the normalized approach curve started with the polarizability of a small W sphere of radius $a = 20\,nm$ described by a known polarizability α_{sphere}^{20nm} as represented on top of Fig. 7.6 (cf. caption for details). A correct estimate seemed to be obtained considering:

$$\alpha_t \simeq \eta \times \alpha_{sphere}^{20nm}\, e^{i\Phi_{\alpha_t}}$$

with

$$\eta = 7 \quad \text{and} \quad \Phi_{\alpha_t} = 15°,$$

where η and Φ_{α_t} are the amplitude and phase modification factor needed to determine the empiric complex valued α_t. The enhancement factor 7 with respect to a

sphere is in the range of expectation considering the lightning rod effect due to the elongated tip shape. The additional phase term Φ_{α_t} strongly impacts the phase of the scattered field upon approaching the tip and needs to be adjusted to recover the observed phase change of about 20°. Finally the sphere had to be positioned about $1.5\,a$ above the tip extremity, to temper the field increase. The approach curve in phase[14] determined with this model is shown in Fig. 7.7.

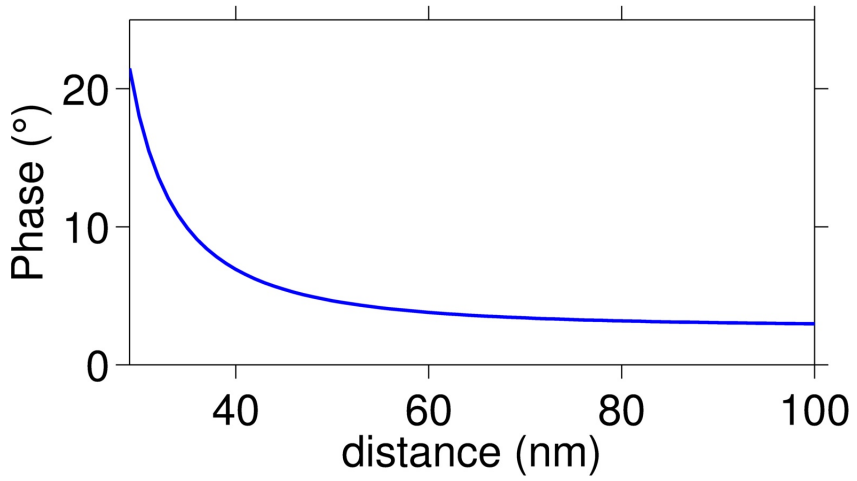

Figure 7.7.: Approach curve in phase on polymer/gold grating using the described effective dipole model with an effective sphere $\eta = 7$ and $\phi_{\alpha_t} = 15°$ of radius $a = 20\,nm$, positioned at $h = 1.5\,a$ above the tip apex.

Discussion In this subsection we have obtained an estimation of the complex vertical tip polarizability, based on the effective dipole model. The evaluation was facilitated by the nature of the selected sample. This "effective probe" approach looks like an interesting way to characterize the fabricated tip response before characterizing a sample. In the near-future, the validity of the approach should be however further tested, e.g with several substrates like Silicon in addition to Gold.

The effect of the lock-in detection was not considered in the signal analysis, but it can be handled without difficulty given the model simplicity. For the considered parameters, we then find that the obtained approach curve in amplitude and phase are actually very similar, except that the amplitude signal is reduced to almost zero for probe-sample distance of few radii a . In our experiment, for distance of few "a" we still have a residual signal corresponding to about 15-20% of the max value. Several reasons can be invoked, but the first one in this experiment is most probably the noise level that subsist when the probe is lift.

[14]Corresponding to the phase shift between reference field and scattered field.

7.5. Investigating Localized Surface Plasmons

NSOM is an adequate characterization technique to study surface waves in general and the localized modes in particular since it is based on the near-field interaction. In this section, we present the study that has been made to investigate the LSPRs in highly doped SC grating. This study is accompanied with preliminary electromagnetic simulations.

7.5.1. Electromagnetic simulations: Near-field electric field versus project far-field

In these simulations, the commercial FDTD solver Lumerical was used. The real and imaginary parts of the highly doped InAsSb material was modeled based on the Drude theory with doping level of $5 \times 10^{19}\text{cm}^{-3}$. The schematic shown in Fig. 4.10 was adopted, again because it gives the most realistic picture of the studied sample. The standard structure shape was modeled based on AFM measurements. It is a trapezoidal shape, with rounded top edge, while the average width varies from 436 nm base to 130 nm top. Fig. 7.8 shows the reflectivity of these structures at normal incident plane wave source with illumination region of 20 μm. Two cases were considered, the first one, where the reflectivity was calculated over a region of a number of periods (55 period), the second using periodic boundary conditions at the axis perpendicular to the substrate.

As it can be noticed from Fig. 7.8, for the case with periodic boundary conditions, which is equivalent to infinite periods, we have more intense peak with higher selectivity. This clearly shows the effect of coupling between the structures. The experimental FTIR spectrum shows wider resonance peak than both cases, that could be related to the inhomogeneities of the sample. In the subsequent study we will consider the resonance wavelength of 13.6 μm. The configuration with 50 periods was considered; since our goal is to simulate a NSOM profile and this can't be realized using periodic boundary conditions. We limited the simulations to 55 periods to keep acceptable required memory. Also all of these simulations can be done in 2D as long as only the grating structure is considered. When the scattering probe is inserted, 3D simulation should be considered in principle, but for memory space consideration 2D simulations were mostly considered.

Fig. 7.9 presents a near-field image of the enhanced intensity along with its profile. We notice that the maximum field enhancement is localized at the bottom of the structures, at the interface between the highly doped SC and SC. Regarding the

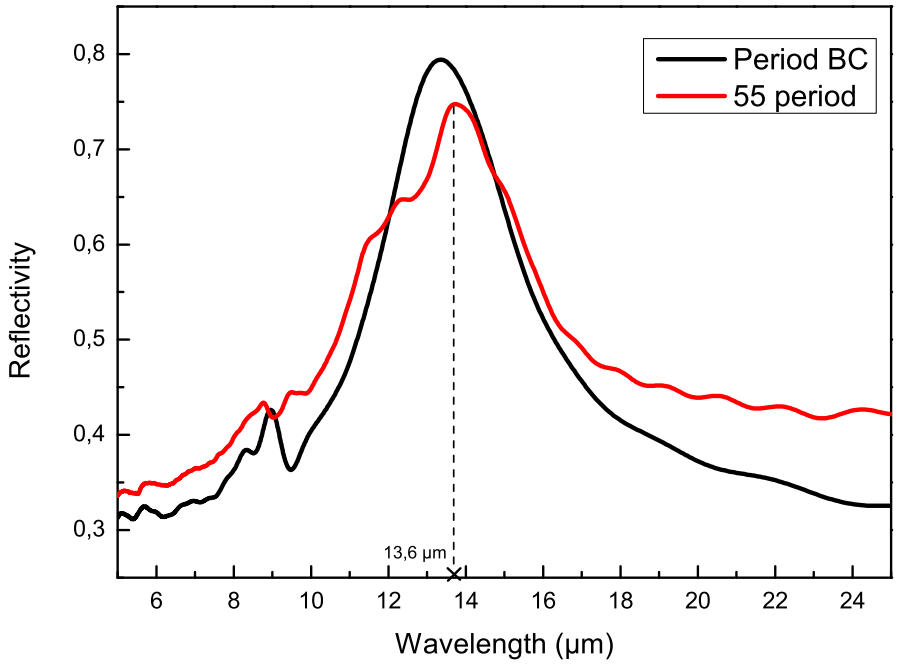

Figure 7.8.: reflectivity of a system of highly doped InAsSb structures over GaSb substrate in case of considering 55 period along with the case of setting periodic Boundary Conditions (BC).

profile of the enhanced field we notice two weak pumps at the top rounded angles of the structures. The contrast measured on the intensity profile is about of 93%[15].

Experimentally, we are unable to measure directly the previously shown near-field profile of Fig. 7.9. Actually, we need a scatterer closely interacting with the surface to transform this near-field information in the far-field and obtain point by point a "detectable" far-field image.

For simulation purpose, a vertical dipole source was set to contour the structure at a distance of 15 nm. The dipole field was recorded with a spatial monitor projected in far-field, squared and integrated over $2\pi\, sr$ to obtain for each position a value proportional to the total scattered power. Fig. 7.10 shows the obtained profile over half a period[16]. As it might be noticed, in this ideal case we were able to reproduce the same profile tendency as the near-field picture however with a contrast of about 80 %.

A dipole source picture is unrealistic, because in practice we have a tip with specific material that is interacting with the sample under investigation. By putting an

[15]The contrast is $\frac{A-B}{A+B}$ with A is the maximum intensity and B the one.
[16]The other half of the profile is symmetric in this case.

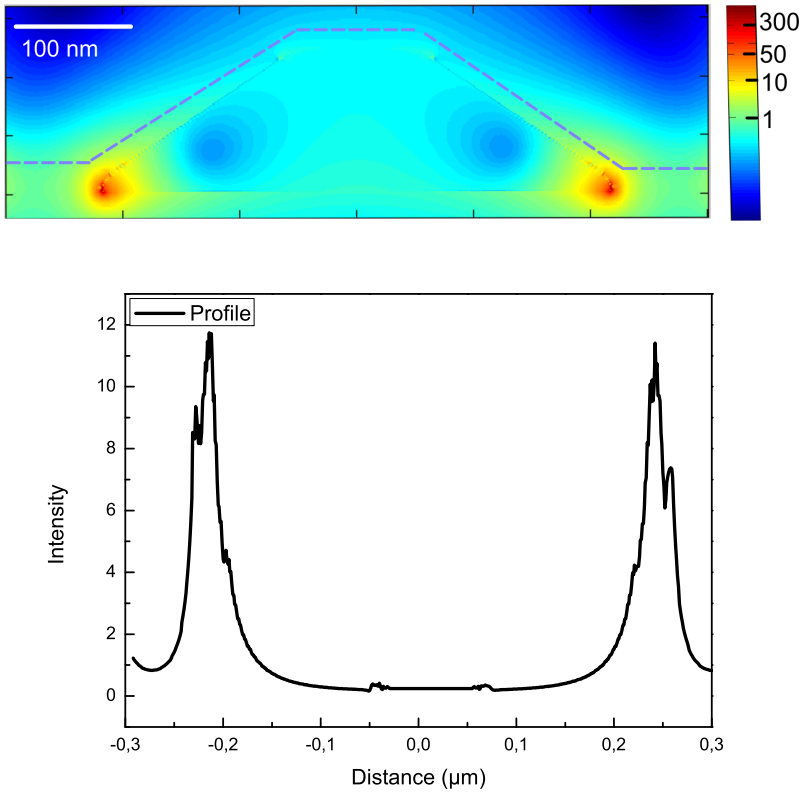

Figure 7.9.: Intensity image at resonance (wavelength of 13.6 μm) of the total field scattered by structure, along with a profile taken along the dashed line which about 15 nm from the sample surface.

elongated probe instead of dipole we expect to be more sensitive to the vertical field component, but the intensity profile for this component is similar to that of the intensity. Fig. 7.11 shows the profile obtained by the same setup, however instead of a dipole source we set a tungsten tip with plane wave illumination. The illumination was incident at an angle of 45 ^{o}, then the background effect was removed. The tungsten tip has a rounded tip cone shape, truncated at length of 16 µm, with a tip radius of 20 nm and sharpness angle of 10°. We can see a huge modification on the profile upon the introduction of the tip, related to an enhanced probe sample interaction [17]. However the 2D configuration can notably modify the real profile (here the contrast in only 5%), full 3D simulations as those described at the end of appendix are currently under progress.

To evaluate the pure effect of the probe sample interaction, a tip was placed at a distance of 15 nm close to a semi-infinite slab of GaSb. Then the results were compared to the case where we have highly doped InAsSb semi-infinite slab. The far-field intensity was calculated in both cases upon side plane wave illumination

[17]We can point out that Fig. 7.11 is kind of symmetric, however off-resonance the asymmetry increases significantly.

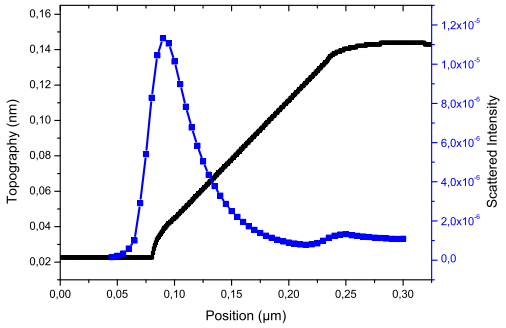

Figure 7.10.: Profile collected in the far-field in case of a dipole source, over half a period.

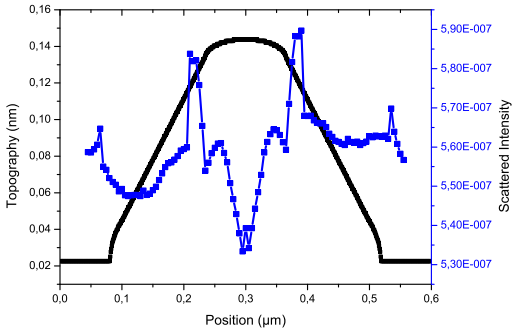

Figure 7.11.: Profile collected in the far-field of the tungsten-sample interaction, after removing the background, over a period.

at 45 ^{o} angle of incidence. After removing the background we have found that the far-field intensity in the case of highly doped InAsSb is 4 times more than that on GaSb. As already discussed, this is a non-new phenomena where the previously reported NSOM images always showed a bright contrast on metals in comparison to dielectric [53, 73]. It means that, in principle, the far-field recorded intensity above the InAsSb overestimates the local intensity (this is the case for the dipole profile too). Since we are mainly interested in the local field distribution rather the local permittivity which is fairly known, this information could be used to correct the far-field intensity profile from this probe-sample interaction effect.

7.5.2. NSOM Detecting LSPR

We have investigated the sample described in (sec. 5.2.1), using the developed method GLIA applied to NSOM featuring a QCL (setup described in (sec. 7.1)). Fig. 7.12 shows the simultaneously obtained 3 images, topography, amplitude and phase of the scattered field, along with their extracted profiles. The shown images are scanned under wavelength of 10.4 μm. We clearly see that the LSP are localized on the top corner of the ribbons, with a contrast of about 40%. Having a closer look on the profile of the amplitude of the scattered intensity we can clearly see some analogy with the numerically calculated one in Fig. 7.11, some of the discrepancy coming the current 2D nature of the simulation.

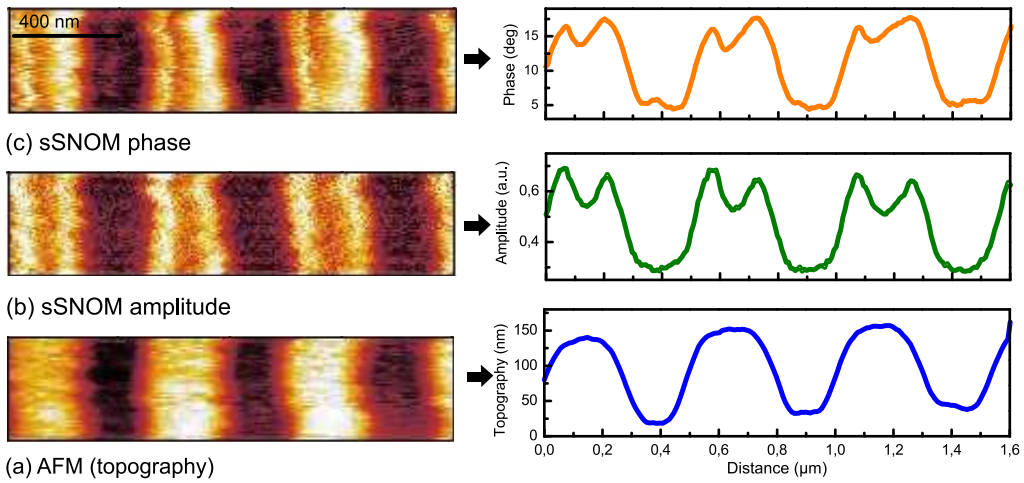

Figure 7.12.: Highly doped Sc grating (a) Topography image, (b) s-NSOM amplitude image, (c) sSNOM Phase image. The corresponding along extracted profiles averaged over 5 lines are shown to the right of each image

7.5.3. Spectroscopic Study

A spectroscopic study was made over the available spectral range of the mounted QCL (10-10.5 μm). Five highly resolved images were recorded, allowing us to determine the contrast and phase shift for each wavelength. Fig. 7.13 shows a contrast evolution ranging from 3 to 5 %, and a corresponding phase shift ranging from 3 to 14 degrees. This contrast is obtained by comparing the maximum signal with the minimum signal. The maximum contrast corresponds to the maximum intensity as well occurring at wavelength of 10.4 μm. Comparing this maximum to that obtained in the far-field interaction at 9.7 μm, we obtain a shift of 0.7μm between the far-field interaction and near-field interaction.

7.6. Conclusion

In conclusion we were able to successfully apply a new signal extraction method on NSOM. This method provided highly resolved images in phase and amplitude of the scattered field. The system was tested on several samples and a polymer/gold grating structure was proposed as an interesting approach to characterize tip polarizabilities. We were also able to investigate the occurrence of the LSP in a highly doped semiconductor grating. Electromagnetic simulations were conducted on a simulated version experimental NSOM setup. Although some similar features were observed in both cases, our simulated NSOM experiment must still be improved to model the experiment in order to help in determining quantitative information such as quality factor of the resonance and the field enhancement.

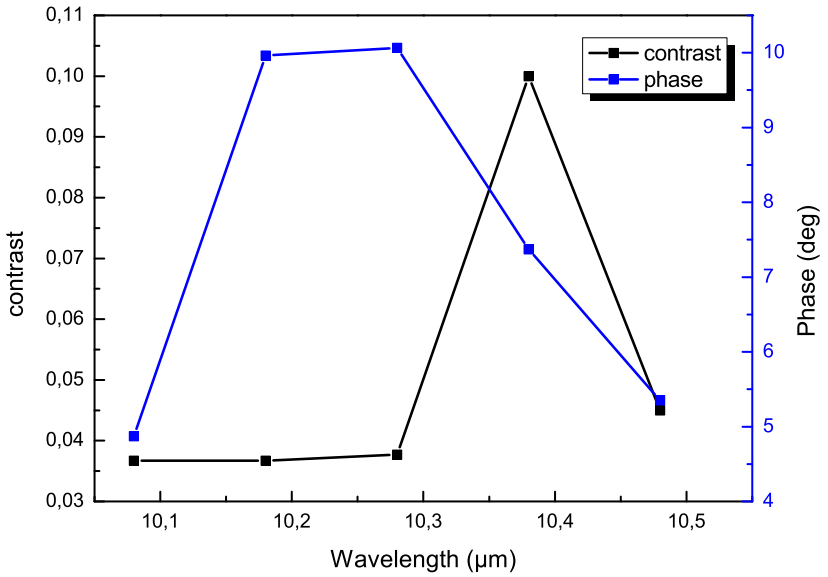

Figure 7.13.: Spectroscopy contrast and phase shift between highly doped InAsSb structures and the GaSb substrate.

8. Conclusion and Perspectives

This work combines the theoretical description as well as the experimental examination of IR surface modes with emphasis on the experimental methodology. It was conducted in the farfield regime in order to have a global image; a complementary study was done in the near-field regime with the aim to have a local one.

In the farfield, the theoretical part consists of using two analytical models, and developing a third one. These analytical models were tested and compared to numerical simulations. Then, the analytical models were applied to the experimental measurements enabling retrieving full information about our studied sample. Moreover on the theoretical part, simulations were conducted to characterize the surface modes in thin surfaces as well as structured ones. We have illustrated that the surface modes for a single interface are accounted by the effective permitivity of a single damped Lorentzian oscillator; the surface is creating the restoring force responsible for such a behavior. Realistic nano-structures were numerically simulated in order to examine their resonance frequencies, field enhancement, far-field intensity. These structures were made of highly doped semiconductor ($5\times10^{19}\text{cm}^{-3}$ same as the real sample) as well as SiC.

Regarding the analytical models, the first one used is based on the Kramers-Kronig relations, known to be applied to farfield spectroscopy, where they enable the determination of reflection coefficient phase knowing its amplitude. The second related model is developed based on solving boundary continuity conditions of Maxwell's equations for the propagation of electromagnetic waves in a layered medium. This model was used in the case where the surface structuration is pronounced enough to be considered as an effective layer (nanostructures + air). Another case that was dealt with, is when nanostructures are too small to form a marked effective layer but in the same time they impact the underlying substrate. For the latter case a model based on modified Lorentz damped oscillator was applied.

We were able to determine experimentally the resonance frequencies in a highly doped SC grating; accurate results were manifested through the back calculation of the experimental reflectivity. The nature of the resonance frequencies were pointed out using the LO and TO loss functions. Regarding the slightly structured surfaces, we studied the case of SiC nanopillars introduced on the surface of a SiC substrate. We have noticed a significant increase in the phonon scattering rate. A valid justification could be due to creation of new phonon decay channels; via the hybridization with underlying phonon branches.

In the nearfield regime, we have developed an innovative detection method offering an optimum signal to noise ratio for amplitude and phase extraction. We have implemented this technique in our home-built NSOM coupled with a QCL. The new detection technique is based a generalized lock-in detection method to recover amplitude and phase in optical interferometers. It is a highly achromatic, since it is based vibrating mirrors. It is versatile in the sense that any signal modulation could be applied to excite the reference mirror. The conditions to obtain efficient background light suppression were derived and successfully applied. This technique proved to be stable and reliable.

Highly resolved NSOM images were obtained on a gold/polymer grating. This sample was chosen so that analytical comparison with an approach curve is possible; the topography of the polymer lines will serve to control the sample-tip distance. Spectroscopic images were obtained of the highly doped SC/SC grating. Where we have demonstrated the occurrence of LSP at the interface between highly doped SC/ SC. In order to have better understanding of the experimental images, numerical profiles of same structures were simulated.

In the near future, we plan to study the SiC nanostructures with different sizes; either smaller so that we can perceive phonon confinement effects or bigger so that we can have stronger field enhancement. The former can lead us to see new effects as well as determining the phonon mean free path. The latter can lead to new applications based on phonon resonances. In addition, it would be interesting to perform angle-dependent measurement on LSPR or LSPhR samples in order to determine the angle dependence of the effective permittivity. Such study was undertaken numerically with success during this thesis and should be confronted with experimental data. In particular, it should show that in general the nanostructured material can not be simply accounted for by a tensor permittivity corresponding to a uniaxial or biaxial medium, given the complexity of the electromagnetic modes in the thin layer.

Additionally, we have started examining more rigorously NSOM images through comparing them to 3D numerical simulations. We are working on combining the FDTD simulations with Green's far field projections; having the experimental local complex dielectric function should be soon reported. This is important since in a lot of applications we have the analyte sticking on the surface of our device and seeing the local physical properties. Moreover, this is solid step towards quantifying the existing shift between the far-field and the near-field resonances. Also, during this thesis an attempt was made to detect the electromagnetic field distribution via the optical force induced by the nano-structures on the near-field probe. We did not obtained enough signal but recent results in the domain seem to show that this exciting approach should be pursued too.

Finally, on a more technological point of view, the flexibility and simplicity of the G-LIA technique make it interesting for many interferometric applications beside near-field optics such as digital holography or interferometric biosensors as very compact, low-cost phase modulators are compatible with this approach.

Acknowledgments

First and foremost I would like to offer my sincerest gratitude to my supervisor Prof. Aurelien Bruyant. He has been a tremendous mentor for me. He was able to always put me back on the right track whenever I drifted. He has taught me, both consciously and un-consciously, how good scientific research is done. I appreciate his time, ideas and faith to make my Ph.D. experience productive and stimulating. The passion and enthusiasm he has for research were contagious and motivational for me, especially during tough times in the Ph.D. pursuit. His advice on both research as well as career has been invaluable.

Second, a very special thanks to Prof. Michel Kazan, my journey with him started during my Master's degree studies at AUB, where he has put his trust in me to pursue this PhD thesis project. Since then he has been no less than a supervisor. His support, keen eye, availability and optimism have made a lot of this work enjoyable and achievable.

I would like to extend my gratitude and appreciation to the president of the jury, Prof. Alexandre Bouhelier, his presence meant a lot to me and added a special touch on the discussion and the general execution of the thesis defense. Deep thanks go to the rapporteurs Prof. Thierry Taliercio and Prof. Malek Tabbal for accepting the mission of evaluating my thesis work. Their attention to details and physical insight have truly enriched my thesis. I'm grateful as well to the thesis examiner Prof. Ziad Herro for his valuable comments.

I'm intellectually indebted and grateful to the engineer, Julien Vaillant, who gave me gentle help every time I had hardship communicating with the machines (especially labVIEW). I would like to thank, as well, Dr. Zohreh Sedaghat, the former PhD student, for providing me so much help at the initial stages of this thesis as well as being a close real friend.

This thesis took place in a joint program between the University of Technology of Troyes, the Lebanese University and the American University of Beirut. I was lucky to have access to all the facilities provided by these three institutions of higher education. However sometimes I had hard time doing the administrative work, luckily many amazing people were there to facilitate the process, namely: Mme Pascal Denis and Mme Therese Kazarian at UTT; Mme Zainab Ibrahim and Mme Maha Sidani at UL; Mme Joumana Abi Fallah at AUB. More over I'd love to point out that my supervisor at the Lebanese University, Prof. Antonio Khoury, has retired during my thesis however he was always available to reply promptly upon any inquiry.

The majority of the thesis work was done at the Laboratory of Nanotechnology, Optics and Instrumentation (LNIO). I'd love to thank the laboratory director Prof. Renauld Bachelot. Special thanks to Prof. Gilles Lerondel and Prof. Safi Jradi for the fruitful discussions, Prof. Sylvain Blaize for couple of interesting simulations. Moreover I'd love to thank the engineer Serguei Kochtcheev and Dr. Anna Rumyantseva for preparing some of the samples. I really appreciate all LNIO members permanents and impermanent for creating such a friendly, lovely and stimulating environment that added joy to coming each day to work.

To my insanely awesome friends, Dr. Irene Izquierdo, Dr. André Santos, Yi Huang, Dr. Wassim Kassem, Sahar Deeb and Ghaydaa Assi: Thanks for being my family in France.

To my amazing family, my super-parents, and my adorable siblings: Thank you for the unconditional, continuous love, care and support. Your love was always the light that lit my way!

Finally I want to thank my man, my friend, my love, my husband, Machal El Dib. Your presence in my life made everything nice and simple. Thanks for all the things you have given me. I will love you till the end of time.

A. Transfer Matrix Model

A.1. Overview

Since we are measuring the reflectivity we are interested in finding an expression for the reflectance of our film. We will briefly review the boundary conditions for Maxwell's equations to model the infrared reflectance of light by a single film and properly apply the boundary conditions. The derivation could be easily extended to the case of multilayer system as the product of individual layer matrices. Starting with Maxwell's equations for a medium with no space-charge:

$$\begin{aligned} \nabla \times \mathbf{E} &= -j\omega\mu\mathbf{H} \\ \nabla.\mathbf{E} &= 0 \\ \nabla \times \mathbf{H} &= \sigma\mathbf{E} + j\omega\epsilon\mathbf{E} \\ \nabla.\mathbf{H} &= 0 \end{aligned}$$

Where symbols have their usual meanings. The general form of a plane wave solution of Maxwell's equations for the electric and magnetic fields are of the form:

$$\begin{aligned} E(r,t) &= E_0 e^{j(\omega t \pm k.r)} \\ H(r,t) &= H_0 e^{j(\omega t \pm k.r)} \end{aligned}$$

We neglect the time term since we are recording an average of reflected and transmitted beams over many cycles. However, the expressions for the electric vectors of the incident, reflected, and transmitted waves at the interface between medium (n_0) and medium (n_1) include additional geometric phase factors of the form:

$$\begin{aligned} & e^{j(\omega t - \frac{2\pi n_0 x \sin\theta_0}{\lambda} - \frac{2\pi n_0 \cos\theta_0}{\lambda})} && \text{(incident)} \\ & e^{j(\omega t - \frac{2\pi n_0 x \sin\theta_0}{\lambda} + \frac{2\pi n_0 \cos\theta_0}{\lambda})} && \text{(reflected)} \\ & e^{j(\omega t - \frac{2\pi n_1 x \sin\theta_1}{\lambda} - \frac{2\pi n_1 \cos\theta_1}{\lambda})} && \text{(transmitted)} \end{aligned}$$

Here we follow the notation used in [51]. We denoted the positive and negative light traveling direction. The subscripts 0, l, 2 denote light propagation in medium 0

with index of refraction n_0, medium 1 with $n_l = n + jk$, medium 2 with complex index of refraction n_t respectively. Fresnel reflectivity and transmission coefficients are denoted by r and t respectively. Applying the boundary conditions that the tangential component of both the electric and magnetic fields is continuous at every boundary. We take $\mu = 1$, and J the surface current density, to be negligible (in case of non-metallic layer). We get:

- First boundary (at x=0):

$$\begin{aligned}(E_{0p}^{+} + E_{0p}^{-})\cos\theta_0 &= (E_{1p}^{+} + E_{1p}^{-})\cos\theta_1,\\ (E_{0p}^{+} - E_{0p}^{-})n_0 &= (E_{1p}^{+} - E_{1p}^{-})n_1,\\ E_{0s}^{+} + E_{0s}^{-} &= E_{1s}^{+} + E_{1s}^{-},\\ (-E_{0s}^{+} + E_{0s}^{-})n_0\cos\theta_0 &= (-E_{1s}^{+} + E_{1s}^{-})n_1\cos\theta_1.\end{aligned} \tag{A.1}$$

- Second boundary (at x=d_1):

$$\begin{aligned}(E_{1p}^{+}e^{-jx_1d_1} + E_{1p}^{-}e^{+jx_1d_1})\cos\theta_1 &= E_{2p}^{+}e^{-jxd_1}\cos\theta_2,\\ (E_{1p}^{+}e^{-jx_1d_1} - E_{1p}^{-}e^{+jx_1d_1})n_1 &= E_{2p}^{+}e^{-jxd_1}n_2,\\ E_{1s}^{+}e^{-jx_1d_1} + E_{1s}^{-}e^{+jx_1d_1} &= E_{2s}^{+}e^{-jx_2d_1},\\ (-E_{1s}^{+}e^{-jx_1d_1} + E_{1s}^{-}e^{+ijxd_1})n_1\cos\theta_1 &= E_{2s}^{+}e^{-jx_2d_1}n_2\cos\theta_2.\end{aligned} \tag{A.2}$$

These can be rewritten in terms of Fresnel coefficients as:

$$\begin{aligned}E_{i-1}^{+} &= \frac{E_i^{+}e^{ij\delta} + r_i E_i^{-}e^{j\delta_{i-1}}}{t_n},\\ E_{i-1}^{-} &= \frac{E_n^{+}e^{-j\delta_{i-1}} + E_i^{-}e^{-j\delta_{i-1}}}{t_i},\end{aligned} \tag{A.3}$$

where $\delta_i = 2\pi n_i d_i \cos\theta_i/\lambda$ is the phase change as the light traverses interface i. It is important to point out that the dependence on the wave polarization in equation (A.3) is impeded in Fresnel coefficients:

$$\begin{aligned}r_{i\perp} &= \frac{n_{i-1}\cos\theta_{i-1} - n_i\cos\theta_i}{n_{i-1}\cos\theta_{i-1} + n_i\cos\theta_i},\\ r_{i\parallel} &= \frac{n_i\cos\theta_{i-1} - n_{i-1}\cos\theta_i}{n_i\cos\theta_{i-1} + n_{i-1}\cos\theta_i},\\ t_{i\perp} &= \frac{2n_{i-1}\cos\theta_{i-1}}{n_{i-1}\cos\theta_{i-1} + n_i\cos\theta_i},\\ t_{i\parallel} &= \frac{2n_{i-1}\cos\theta_{i-1}}{n_i\cos\theta_{i-1} + n_{i-1}\cos\theta_i}.\end{aligned} \tag{A.4}$$

It is more convenient to express equation (A.3) in a matrix form, that gives:

$$\begin{pmatrix}E_{i-1}^{+}\\ E_{i-1}^{-}\end{pmatrix} = \frac{1}{t_i}C(i)\begin{pmatrix}E_i^{+}\\ E_i^{-}\end{pmatrix}$$

where:

$$C(i) = \begin{pmatrix}e^{j\delta_{i-1}} & r_i e^{j\delta_{i-1}}\\ r_i e^{-j\delta_{i-1}} & e^{-j\delta_{i-1}}\end{pmatrix}$$

represents the characteristic matrix of the i^{th} layer. For the case of single film deposited on a substrate, figure (Fig. 4.5) , we have:

$$\begin{pmatrix} E_0^+ \\ E_0^- \end{pmatrix} = \frac{1}{t_1 t_2} C(1)C(2) \begin{pmatrix} E_2^+ \\ E_2^- \end{pmatrix}$$

upon considering an infinite substrate there is no back reflected wave in medium 2, so $E_2^- = 0$, thus if we represent:

$$C(1)C(2) = \begin{pmatrix} a & b \\ c & d \end{pmatrix}$$

the effective Fresnel reflection coefficient:

$$r = \frac{E_0^+}{E_0^-} = \frac{c}{a} = A + jB \tag{A.5}$$

B. Nature of the NSOM signal

B.1. Overview

NSOM characterization technique main asset is the ability to transform the information of a given system from near-field to far-field. This happens through the probe sample interaction; while the probe is placed in the vicinity of the sample. In order to qualitatively understand the phenomena, a lot of numerical methods have been followed to solve the electromagnetic equations. However an analytical model, based on the dipole approximation is quite instructive and helps understanding this coupled interaction.

Most of this appendix follow derivations presented extensively in the PhD work of Z. Sedaghat [114] under the supervision of Prof. A. Bruyant at UTT. However, recalling this information with few additional comments should help in understanding the obtained NSOM results in the last chapter of this thesis. For this purpose, the analytical NSOM model is presented based on dipole approximation and a numeric generalization to arbitrarily shaped probes is given.

B.2. Dipole approximation

In this approximation, we model our probe as a small polarizable sphere and the sample is large compared to the probe as to be regarded as semi-infinite.

B.2.1. Dipole in free space

Lets recall first the electric field of a dipole in free space, in both cases: electrostatic dipole and oscillating dipole.

B.2.1.1. Electrostatic dipole

We consider an arbitrarily oriented static dipole moment[1] $\mathbf{p}$ at a position $\mathbf{r_1}$ in a homogeneous medium ϵ_m. The electrostatic electric field, at a position $\mathbf{r_2}$, is given by the column vector:

[1] All the vectors $\mathbf{v}$ are considered as column vectors, unless we consider the transposed vector $\mathbf{v'}$.

$$\mathbf{E^{stat}}(\mathbf{r}) = -\mathbf{grad}(V(r)), \qquad with \qquad V(r) = K_c \frac{\mathbf{p}.\mathbf{u_r}}{r^2}$$

with:
$K_c = \frac{1}{4\pi\epsilon_o\epsilon_m}$ the Coulomb constant
$\mathbf{r} = \mathbf{r_2} - \mathbf{r_1}$, $\mathbf{u_r} = \mathbf{r}/r$, and $r = |\mathbf{r}|$
The dipole field can be expressed as:

$$\mathbf{E^{stat}}(\mathbf{r}) = \frac{K_c}{r^3}\left\{3(\mathbf{p}.\mathbf{u}_r)\mathbf{u}_r - \mathbf{p}\right\}, \tag{B.1}$$

To find the dyadic link S^{stat} between $\mathbf{E_{stat}}$ and $\mathbf{p}$, we factorize by $\mathbf{p}$:

$$\mathbf{E^{stat}}(\mathbf{r}) = S^{stat}(\mathbf{r_2},\mathbf{r_1})\mathbf{p} \qquad \rightarrow S^{stat} = K_c\left\{3\mathbf{u_r}\mathbf{u'_r} - \mathbf{Id}\right\}$$

where the dyadic tensor[2] S^{stat} accounting for the propagation from $\mathbf{r_1}$ to $\mathbf{r_2}$ is usually introduced using Green formalism [98]. S^{stat} is the dyadic Green function for an electrostatic dipole in a medium ϵ_m.

B.2.1.2. Oscillating dipole

It is quite instructive to present the case of an oscillating dipole, $\mathbf{p} = pe^{i\omega t}\mathbf{u_p}$, at a frequency of ω in a homogeneous medium ϵ_m . The complex field radiated in $\mathbf{r}$ is[60]:

$$\mathbf{E}(\mathbf{r}) = K(r)\left\{\frac{k^2}{r}(\mathbf{u_r}\times\mathbf{p})\times\mathbf{u_r} - \frac{ik}{r^2}[3\mathbf{u_r}(\mathbf{u_r}.\mathbf{p}) - \mathbf{p}] + \frac{1}{r^3}[3\mathbf{u_r}(\mathbf{u_r}.\mathbf{p}) - \mathbf{p}]\right\} \tag{B.2}$$

where $K(r) = K_c e^{ikr}$, and $k = \sqrt{\epsilon_m}k_o$ is the wavevector in the medium. Again, the Green function can be obtained by factorizing :

$$\mathbf{E}(\mathbf{r}) = S(\mathbf{r_2},\mathbf{r_1})\,\mathbf{p}, \tag{B.3}$$

with:

$$S(\mathbf{r_2},\mathbf{r_1}) = S^{ff} + S^{if} + S^{nf}, \tag{B.4}$$

where the Green dyadics accounting for the propagation from $\mathbf{r_1}$ to $\mathbf{r_2}$ are:

[2] A dyadic is a second rank tensor, obtained through the inner product of a column vector by a line (transposed) vector .

- $S^{ff} = K(r)\,\frac{k_o^2}{r}\,[(\mathbf{u_r}'\mathbf{u_r})\,\mathbf{Id} - \mathbf{u_r}\mathbf{u_r}']$, dominant for $r \gg \lambda$ (far field zone)
- $S^{if} = K(r)\,\frac{ik_o}{r^2}\,[\mathbf{Id} - 3\mathbf{u_r}\mathbf{u_r}'] = -rS^{stat}$, dominant for $r \approx \lambda$ (intermediate zone).
- $S^{nf} = K\,\frac{1}{r^3}\left[3\mathbf{u_r}\mathbf{u_r}' - \mathbf{Id}\right] = S^{stat}$, dominant for $r \ll \lambda$ (near-field zone)[3]

The dipole near-field decreases as r^{-3} and has radial polarization component. In this zone, it is *quasi-static*: i.e. identical to a static dipole with an harmonic phase variation.

In far-field, the radiation field is transverse with the expected r^{-1} variation. The radiated or scattered far-field $\mathbf{E}_{scat}$ is proportional to the local dipole: $\mathbf{E}_{scat} = S^{ff}\mathbf{p}$. Figure Fig. B.1 shows the far-field pattern $|E(\theta,\phi)|$ of a vertical dipole obtained via S^{ff} , together with the far-field patterns for the three components. As can be seen by comparing the left and right part of the figure, the far field mostly keep the polarization of source dipole.

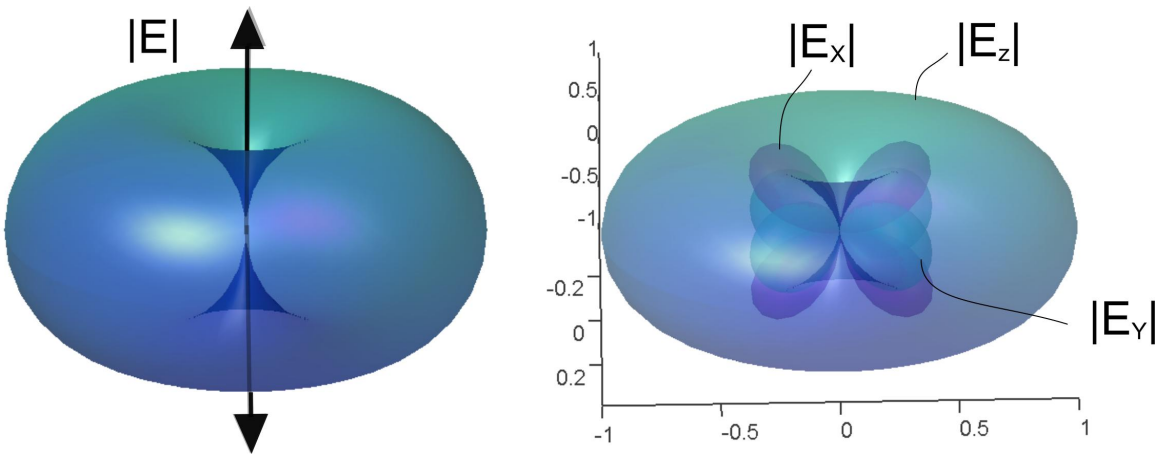

Figure B.1.: Left: far-field pattern $|E(\theta,\phi)|$ of a vertical dipole obtained via S^{ff}. Right: Similar far-field patterns for each field component (transparent textures).

B.2.2. Dipole near a Surface: Effective Polarizability

In order to model a typical NSOM experiment, we have to take into consideration the case of a dipole induced by an external electric field illumination $\mathbf{E_i}$:

$$\mathbf{p} = \alpha\mathbf{E_i}$$

[3]In the near-field, $K(r)$ tends to the Coulomb's constant K ($kr \ll 1$)

where α is the "dressed" polarizability of the considered particle which is a complex number for small sphere. Alternately the induced dipole can be expressed as being proportional to the internal field inside the dipole element via the "bare" polarizability. The two polarizabilities have slightly different expressions and can have a tensor form to account for anisotropic polarizability.

When $\mathbf{p}$ is brought near a surface, the source dipole interacts with its image through the surface. In consequence, there is a "self-field" modifying the dipole source moment. This phenomena is represented in figure (Fig. B.2) via the circular arrow.

From the method of image charges, the image dipole moment created by influence is[4] expressed considering that all the dipole evanescent waves are reflected in phase, resulting in a simple expression:

$$\mathbf{p_{im}} = M\mathbf{p} = \beta \begin{pmatrix} -1 & 0 & 0 \\ 0 & -1 & 0 \\ 0 & 0 & 1 \end{pmatrix} \mathbf{p} \text{ with } \beta = \frac{\varepsilon_s - \varepsilon_m}{\varepsilon_s + \varepsilon_m}, \tag{B.5}$$

where β is the Fresnel reflection coefficient in the electrostatic limit[5] for the p polarized light, and ε_s is the dielectric function of the sample [6].

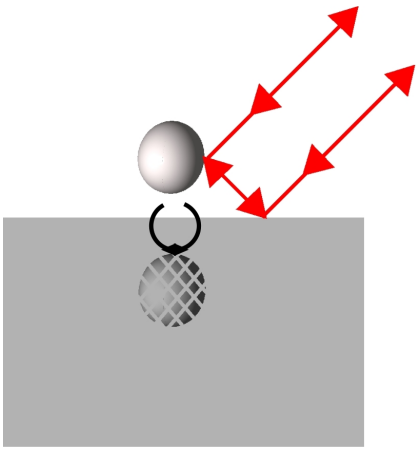

Figure B.2.: Dipole and image dipole, considered for one angle of illumination and detection. The point-dipole is illuminated by a direct field $\mathbf{E_0}$ and a reflected field $r_p\mathbf{E_o}$. The expression given for the back-scattered field includes also a direct and an indirect (reflected) contribution. The reflected contribution is said to be coming from the image dipole . The image dipole also modify the moment of the source dipole via the effective polarizability α_{eff}.

[4] In the case a small polarizable sphere, we assume the diameter very small compared to the wavelength and that the distance to the surface is in the order of the probe diameter.
[5] i.e. considering large parallel wavevectors, related to evanescent waves (non-propagating field) .
[6] Derivation of equation (B.5) is found in [119, 69].

Quasi-Static Self-Field The self-field can now be expressed considering the field created by the image dipole on the primary dipole, :

$$\mathbf{E}_{self} = S^{nf}(\mathbf{r_p}, \mathbf{r_{im}})\mathbf{p_{im}}, \tag{B.6}$$

where $\mathbf{r_{im}}$ and $\mathbf{r_p}$ are the position of $\mathbf{p_{im}}$ and $\mathbf{p}$ respectively. Using S^{stat} of the equation (B.4) and the expression for $\mathbf{p_{im}}$ we find:

$$\mathbf{E}_{self} = K_c\beta \begin{pmatrix} -1/8h^3 & 0 & 0 \\ 0 & -1/8h^3 & 0 \\ 0 & 0 & -2/4h^3 \end{pmatrix} \mathbf{p} = S^{nf}_{surf}(\mathbf{r_p}, \mathbf{r_p})\mathbf{p}, \tag{B.7}$$

Where h is the dipole-sample distance and the near-field propagator S^{nf}_{surf} accounts for the reflected fields from the surface only when $\mathbf{p}$ is close to the surface[7].

Effective Polarizability Due to the surface proximity, the external field at the probe dipole is now:

$$\mathbf{E}_{local} = \mathbf{E}_i + \mathbf{E}_{self} = \mathbf{E}_i + S^{nf}_{surf}(\mathbf{r_p}, \mathbf{r_p})\mathbf{p} \quad , \tag{B.8}$$

$$\text{and} \quad \mathbf{p} = \alpha\mathbf{E}_{local} \tag{B.9}$$

From which we deduce the "effective polarizability" α_{eff} defined as the ratio between the actual dipole moment $\mathbf{p}$ and $\mathbf{E_i}$, the initial field:

$$\mathbf{p} = \alpha_{eff}\mathbf{E_i} \text{ with } \alpha_{eff} = \frac{\alpha}{1 - \alpha S^{nf}_{surf}(\mathbf{r_p}, \mathbf{r_p})}, \tag{B.10}$$

Substituting S^{nf}_{surf}, the obtained tensor α_{eff} has two distinct components:

$$\alpha_{eff} = \begin{pmatrix} \alpha_{eff\parallel} & 0 & 0 \\ 0 & \alpha_{eff\parallel} & 0 \\ 0 & 0 & \alpha_{eff\perp} \end{pmatrix} \text{ with } \alpha_{eff\parallel} = \frac{\alpha}{1 - \frac{\alpha\beta K_c}{8h^3}} = \text{ and } \alpha_{eff\perp} = \frac{\alpha}{1 - \frac{\alpha\beta K_c}{4h^3}}$$

[7] In the near-field region, the total field $\mathbf{E^{nf}}(\mathbf{r})$ created by the dipole ($\mathbf{p}$, $\mathbf{r_p}$) at a given point $\mathbf{r}_{obs}$ has two contributions, a direct one and an indirect (reflected) one:
$\mathbf{E^{nf}}(\mathbf{r}) = \mathscr{S}(\mathbf{r_{obs}}, \mathbf{r_p})\,\mathbf{p}$, with: $\mathscr{S}(\mathbf{r_{obs}}, \mathbf{r_p}) = S^{nf}_{surf}(\mathbf{r_{obs}}, \mathbf{r_p}) + S^{nf}(\mathbf{r_{obs}}, \mathbf{r_p})$,
where $S^{nf}_{surf}(\mathbf{r_{obs}}, \mathbf{r_p}) = MS^{nf}(\mathbf{r_{obs}}, \mathbf{r_{im}})$ and $\mathbf{r}_{im} = \bar{\mathbf{r}}_p = (x_p, y_p, -z_p)$.

(B.11)

as h decreases a strong maximum in $\sigma_\perp$ can be obtained near $\Re(\alpha_t \beta K_c) = 4h^3$. Neglecting the imaginary parts of α_t and β , the pole is reached for:

$$\beta\tilde{\alpha_t} = 4\tilde{h^3} \quad with \;\; \tilde{h} = h/a \tag{B.12}$$

Hence, for tip having high enough polarizability, the maximum can be found before the contact, i.e for $h > a$. The resonance is then termed as *tip-induced* resonance, it is obtained for tip permittivity close to -2 for a sphere. Equivalently a resonance can be found for very large electrostatic reflection coefficient β. The resonance is termed *sample-induced* resonance, which occurs for sample permittivity close to -1.

Fig. B.3 shows the resonance of $\sigma_\perp \propto |\tilde{\alpha}_{eff\perp}|^2$ as a function[8] of probe and tip permittivities at different distances h. These resonances however are not obtained for many materials as permittivities are rather large for most of the materials, so that the ratios β and $\tilde{\alpha}_t$ are close to one. However real sharp probes exhibit higher polarizability than a sphere so that tip-induced resonances are more likely to occur in some experiments.

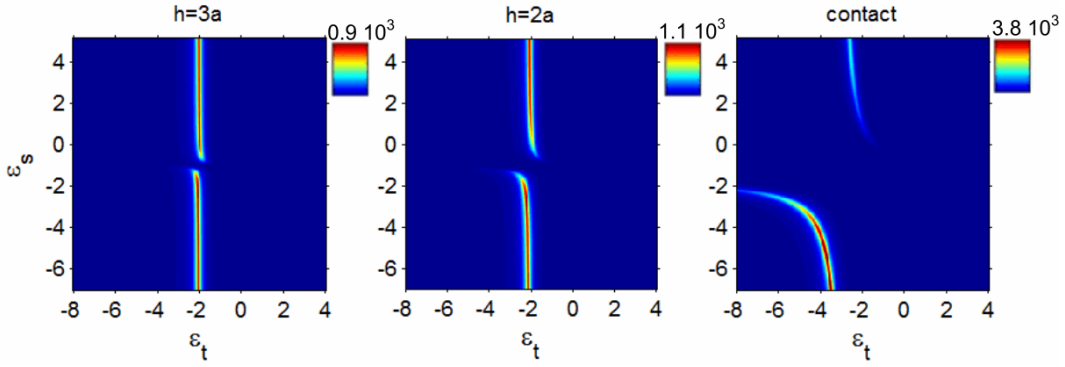

Figure B.3.: Plot of the squared dimensionless effective polarizability $|\tilde{\alpha}_{eff\perp}|^2$ showing the resonances in the scattering cross-section $\sigma_\perp$. An imaginary part of 0.1 was taken for both ε_s and ε_t.

B.2.3. Radiation of a surface-coupled dipole

We are interested in the far-field radiation $\mathbf{E}_{scat}(\theta, \varphi)$ of a surface-coupled dipole in a direction (θ, φ) above the surface:

$\mathbf{E}_{scat}(\theta, \varphi) = \mathbf{E}_D(\theta, \varphi) + \mathbf{E}_R(\theta, \varphi)$,

[8]Like for the dimensionless polarizability of the tip $\tilde{\alpha_t} = \frac{K_c}{a^3}\alpha_t$, the dimensionless effective polarizability is $\tilde{\alpha}_{eff} = \frac{K_c}{a^3}\alpha_{eff}$.

As shown in figure (Fig. B.2), there is a direct contribution $\mathbf{E_D}$ and the reflected part $\mathbf{E_R}$ involving polarization and angle dependent Fresnel coefficients (image contribution). In NSOM the probe polarization is typically parallel to the tip long axis (along $\mathbf{u_z}$) to benefit from the lightning rod enhancement. If the polarization is not purely vertical, it is still often assumed that only the the vertical component of the field has to be considered as the vertical polarizability is stronger for elongated tip.

For a vertically oriented dipole[9], the field has a simple expression:

$$\mathbf{E}_D(\theta,\varphi) = \mathbf{E}_D(\theta) = K(r)\,\frac{k^2}{r} e^{ikr} p_z\,\sin(\theta)\,\mathbf{u}_\theta \tag{B.13}$$

Since the far-field of a vertical dipole is only p-polarized (i.e along $\mathbf{u}_\theta$) , the reflected contribution is $\mathbf{E}_R = r_p \mathbf{E}_D$ at small probe-sample distance. Finally:

$$\mathbf{E}_{scat}(\theta,\varphi) = \mathbf{E}_{scat}(\theta) = K(r)\,\frac{k^2}{r} p_z\,\sin(\theta)\,(1 + r_p(\theta))\,\mathbf{u}_\theta \tag{B.14}$$

with $\mathbf{p} = \alpha_{eff}\mathbf{E_i}$.

Considering now the configuration depicted in figure (Fig. B.2), the incident external field $\mathbf{E_i}$ is the sum of the directly incident field $\mathbf{E_o}$ at a large angle θ_o and its reflection on the sample. Considering that the angle of incidence is indeed large and that mainly the vertical component of the field matters for the probe excitation. The following, qualitative, approximation can be made:

$$\mathbf{E_i} \approx (1 + r_p(\theta_o)) E_o \mathbf{u_z} \tag{B.15}$$

In the same configuration we detect the field back-scattered at the same angle θ_o :

$$\mathbf{E}_{scat}(\theta_o) \approx E_o K(r)\, e^{i\omega t}\,\sin(\theta_o)\,\alpha_{eff\perp}(1 + r_p(\theta_o))^2\,\mathbf{u}_\theta \tag{B.16}$$

Differential Scattering Cross-sections: Radiation Patterns The power scattered in a small solid angle $d\Omega$ is obtained via the average pointing vector $< S >$ times the surface dA:

$$dP_{scat}(\theta,\varphi) =< S_{scat}(\theta,\varphi) > dA \tag{B.17}$$

[9] In practice, a more realistic probe is not a single probe dipole but can be considered as the sum of many dipoles accounting for the tip shape.

with

$< S_{scat} >= {}^1\!/_2\sqrt{{}^{\varepsilon_o\varepsilon}\!/_{\mu_o\mu}}|\mathbf{E_{scat}}|^2$ and $dA = r^2 d\Omega$

To obtain the scattered differential scattering cross-section, we normalize by the incident power flux$< S_i >= {}^1\!/_2\sqrt{{}^{\varepsilon_o\varepsilon}\!/_{\mu_o\mu}}|\mathbf{E_i}|^2$:

$$\frac{d\sigma(\theta,\varphi)}{d\Omega} = \frac{dP_{scat}(\theta,\varphi)}{< S_i >}$$

For a vertical dipole at a small distance h we insert the obtained expression for E_{scat}:

$$\frac{d\sigma_\perp(\theta,\varphi)}{d\Omega} = \frac{k_o^4\left|\alpha_{eff\perp}\right|^2}{16\pi^2\varepsilon_o^2} * \sin^2\theta\left|1 + r_p(\theta)\right|^2 \tag{B.18}$$

For an horizontal dipole:

$$\frac{d\sigma_\parallel(\theta,\varphi)}{d\Omega} = \frac{k_o^4\left|\alpha_{eff\parallel}\right|^2}{16\pi^2\varepsilon_o^2} * \left(\left|1 - r_p\left(\theta\right)\right|^2\cos^2\theta\cos^2\varphi + \left|1 + r_s\left(\theta\right)\right|^2\sin^2\varphi\right) \tag{B.19}$$

And the corresponding scattering cross section:

$$\sigma_\perp = \int_{2\pi} d\sigma_\perp \qquad \sigma_\parallel = \int_{2\pi} d\sigma_\parallel, \tag{B.20}$$

where $d\sigma_\perp$ and $d\sigma_\parallel$ given by equation (B.18) and equation (B.19) are respectively proportional to $\alpha_{eff\perp}^2$ and $\alpha_{eff\parallel}^2$.

B.3. Beyond the probe-dipole approximation

In a real NSOM experiment we have a tip that is scanning the surface, so it is important to know how this can impact the obtained results. In practice a needle-shaped probe has a larger vertical polarizability than the polarizability of a sphere. Several improvements can be made such as considering the polarizability of small elongated shape (ellipsoid), but an analytic expression for the fabricated used do not exist. In addition, in contrast with a simple scattering dipole the field scattered by scattering NSOM probe do not have either analytical expression.

In consequence for more precise investigation, numeric methods should be considered. An annoying point is that common electromagnetic solvers such as FDTD

often fail in determining the scattered far-field very precisely and do not provide a lot of physical insights on the probe-sample interaction without parametric studies.

An interesting approach to solve this issue is to consider the scatterer as the sum of many dipoles for which the far-field propagator has an analytic expression. From equation (B.3), if the field scattered in $\mathbf{r_{obs}}$ by a single dipole is:

$$\mathbf{E_{scat}}(\mathbf{r}) = S(\mathbf{r_{obs}}, \mathbf{r_P})\,\mathbf{p}. \tag{B.21}$$

then, if we consider now larger object such as a probe, we use the polarization density $\mathbf{P}$ to generalize this result:

$$\mathbf{E_{scat}}(\mathbf{r}) = \int S(\mathbf{r_{obs}}, \mathbf{r_p})\,\mathbf{P}\,(\mathbf{r_p}) dV_{\mathbf{r_p}} \tag{B.22}$$

where the sum runs over all the object(s) cells defined by their volume $dV_{\mathbf{r_p}}$, positions $\mathbf{r_p}$ and polarization density $\mathbf{P}$:

$$\mathbf{P}(\mathbf{r_p}) = \varepsilon_o \chi \mathbf{E}(\mathbf{r_p}), \quad and \quad \chi = \Delta\varepsilon(\mathbf{r_p}), \tag{B.23}$$

where$\Delta\varepsilon$ is the contrast between the material and the external medium and $\mathbf{E}(\mathbf{r_p})$ is the internal field inside the object that can be determined through any electromagnetic simulation code such as FDTD. In our case we consider the far-field radiation of structures or probe just above a surface. Therefore the equation (B.22), in our case becomes:

$$\mathbf{E_{scat}}(\mathbf{r}) = \int \mathscr{S}(\mathbf{r_{obs}}, \mathbf{r_p})\,\mathbf{P}\,(\mathbf{r_p})\,\mathbf{dV}_{\mathbf{r_p}}, \tag{B.24}$$

with the far-field propagator: $\mathscr{S} = S^{ff} + S^{ff}_{surf}$,

where S^{ff} corresponds to the direct, free space, radiation term given in the previous subsection. It can be re-expressed explicitly as a function of $\mathbf{r_{obs}} = (x,\, y,\, z)$ and $\mathbf{r_p} = (x_p,\, y_p,\, z_p)$:

$$S^{ff}\,(\mathbf{r_{obs}}, \mathbf{r_p}) = \frac{K(r)k^2}{r} e^{[-ik(\frac{x_p x}{r} + \frac{y_p y}{r} + \frac{z_p z}{r})]} \times \begin{bmatrix} (1 - \frac{x^2}{r^2}) & -\frac{xy}{r^2} & -\frac{xz}{r^2} \\ -\frac{xy}{r^2} & (1 - \frac{y^2}{r^2}) & -\frac{yz}{r^2} \\ -\frac{xz}{r^2} & -\frac{yz}{r^2} & (1 - \frac{z^2}{r^2}) \end{bmatrix}, \tag{B.25}$$

and the surface-related propagator S^{ff}_{surf} function of the Fresnel coefficients r_p and r_s can be found in [98]:

$$S^{ff}_{surf}\left(\mathbf{r_{obs}}, \mathbf{r_p}\right) = \frac{K(r)k^2}{r} e^{[-ik(\frac{xp\,x}{r}+\frac{yp\,y}{r}+\frac{zp\,z}{r}]} \times \begin{bmatrix} \frac{x^2}{\rho^2}\frac{z^2}{r^2}f_2 + \frac{y^2}{\rho^2}f_3 & \frac{xy}{\rho^2}\frac{z^2}{r^2}f_2 + \frac{xy}{\rho^2}f_3 & -\frac{xz}{r^2}f_1 \\ \frac{xy}{\rho^2}\frac{z^2}{r^2}f_2 + \frac{xy}{\rho^2}f_3 & \frac{y^2}{\rho^2}\frac{z^2}{r^2}f_2 + \frac{x^2}{\rho^2}f_3 & -\frac{yz}{r^2}f_1 \\ -\frac{xz}{r^2}f_2 & -\frac{yz}{r^2}f_2 & (1-\frac{z^2}{r^2})f_1 \end{bmatrix} \tag{B.26}$$

with $f_1 = r_p(k_\parallel)$, $f_2 = -r_p(k_\parallel)$ and $f_3 = r_s(k_\parallel)$. $k_\parallel$ is parallel wavevector given by $k_\parallel = k\frac{\rho}{r}$, where ρ is the radial coordinate of $\mathbf{r}$ in a cylindrical basis $(\mathbf{u}_\rho, \mathbf{u}_\varphi, \mathbf{u_z})$. A similar expression involving transmission Fresnel coefficients can be found in [98] to calculate the far-field scattered through the surface.

The image Fig. B.4 shows an example of far-field radiation pattern calculated in this way for a vertically polarized sphere above a glass substrate (cf. caption for details).

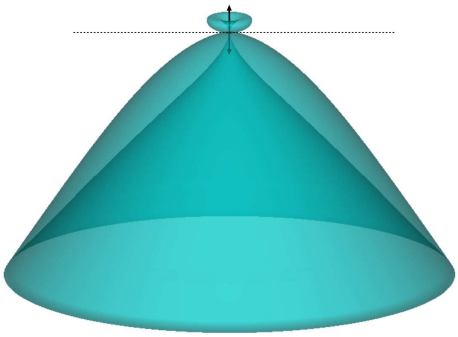

Figure B.4.: Example of 3D radiation pattern (transparent texture) obtained for a small vertically polarized dielectric sphere made of a number of dipoles above a glass surface (20 nm in diameter at $\lambda = 1\mu m$). The pattern is calculated using $\frac{d\sigma_\perp(\theta,\varphi)}{d\Omega}$ in which the scattered field is given by $\mathbf{E_{scat}}(\mathbf{r}) = \int \mathscr{S}(\mathbf{r_{obs}}, \mathbf{r_p})\,\mathbf{P}\,(\mathbf{r_p}) dV_{\mathbf{r_p}}$, where $\mathbf{P}$ was set equal to $\mathbf{P}(\mathbf{r_p})=\varepsilon_o\chi\mathbf{e_z}$, $\mathbf{e_z}$ being an arbitrary vertical unit field.

C. Résumé étendu

Nous donnons ici un résumé étendu en français de ce travail. Ce résumé reprend succinctement les différents travaux réalisés, principalement au sein des parties II et III qui constituent le cœur de cette thèse. Pour plus détails, il convient de se rapporter au manuscrit de thèse proprement dit.

C.1. Introduction

L'objet initial de cette thèse est l'étude des propriétés infrarouges au sein de semi-conducteurs nanostructurés présentant des résonances liées à des phonons-polaritons ou des plasmons-polaritons. L'infrarouge moyen permet de sonder les interactions photon-phonon dans les cristaux polaires mais aussi les interactions photon-plasmon dans les semi-conducteurs fortement dopés. Cette sensibilité autorise, par exemple, une reconnaissance chimique et une analyse physique des nanomatériaux, mise en évidence de contraintes, etc. En dehors d'échantillons « tests », deux échantillons ont principalement été étudiés, chacun présentant a priori des résonances aux longueurs d'ondes d'analyse.

- Un substrat de SiC nano-structuré par lithographie électronique étendue (environ 2 mm par 2 mm), présentant des phonons-polaritons.
- Un échantillon de InAsSb fortement dopé sur GaSb, et présentant des plasmons-polaritons de surface localisés (LSPR pour Localized Surface Plasmon Resonance).

Pour réaliser ces études, nous nous sommes concentrés sur deux méthodes expérimentales distinctes (1 et 2), faisant l'objet de deux parties dans ce manuscrit.

(1) Une caractérisation en champ lointain

Mise en œuvre par spectroscopie à transformée de Fourier en réflexion sur de large assemblées de nanostructures. Les mesures de réflectivité offrent une évaluation quantitative des modifications de permittivité moyenne, à partir de théories et modèles relativement simples, nécessitant néanmoins de déterminer la phase du coefficient de réflexion.

(2) Une caractérisation en champ proche

L'analyse est effectuée à l'aide d'un microscope de champ proche optique fonctionnant dans l'infrarouge moyen possédant une résolution spatiale déca-nanométrique.

Cette méthode peut permettre de recueillir des informations locales sur la permittivité mais aussi d'imager la distribution de champ en surface des nanostructures et ainsi de renseigner sur les modes localisés excités.

Au cours de ce travail, notre attention s'est portée sur le développement de ces deux méthodes d'analyses. En particulier, une méthode novatrice d'extraction de l'amplitude et de la phase au sein de microscope de champ proche optique est proposée.

C.2. Caractérisation en champ lointain et analyse

La Figure C.1 présente schématiquement les deux méthodes mises en œuvre dans cette partie pour remonter à la fonction diélectrique effective des échantillons étudiés. Dans les deux cas, une analyse préalable à l'aide des relations de Kramers-Kronig est nécessaire.

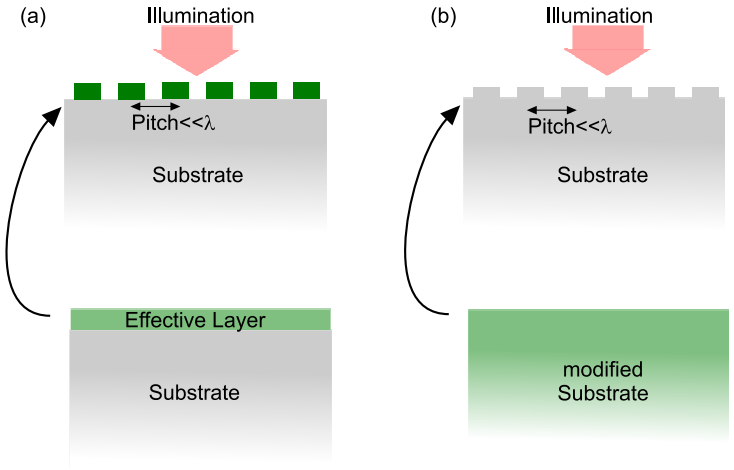

Figure C.1. : Détermination de la réponse infrarouge de nanostructures suivant deux approches : (a) par matrices de transfert, (b) à l'aide d'un modèle paramétrique pour la permittivité et l'utilisation d'une méthode des moindres carrés (fit).

C.2.1. Modèles développés et appliqués

C.2.1.1. Relations de Kramers-Kronig

Pour les deux types de modélisation représentés sur la Figure C.1, on doit utiliser la réflectivité complexe. En effet, considérons tout d'abord la réflectivité pour un échantillon semi-infini. On a la relation bien connue $R = \frac{n-1}{n+1}$, liant le coefficient de réflexion en énergie et l'indice n. Néanmoins, même dans ce cas simple, il n'est pas possible en général d'obtenir l'indice de l'échantillon $n = \sqrt{\epsilon}$, car celui est

complexe et la phase du coefficient de réflexion peut difficilement être déterminer expérimentalement. Néanmoins les relations de Kramers-Kronig (KK) permettent de résoudre cette difficulté.

Les relations de Kramers–Kronig nous donnent la partie imaginaire d'une fonction connaissant sa partie réelle, si cette fonction satisfait certaine conditions. Étant donnée une fonction $\alpha(\omega) = \alpha_1(\omega) + i\alpha_2(\omega)$, alors nous pouvons écrire cette relation entre la partie réelle et la partie complexe :

$$\alpha_2(\omega) = -\frac{2\omega}{\pi} P \int_o^\infty \frac{(\alpha_1(s))}{(s^2 - \omega^2)} ds$$

Où P est la partie principale. Le coefficient de réflexion peut s'écrire :

$$ln\left(r(\omega)\right) = \underbrace{ln\rho(\omega)}_{\alpha_1} + \underbrace{i\theta(\omega)}_{\alpha_2}$$

On peut alors calculer θ en utilisant la réflectivité R via :

$$\theta(\omega) = -\frac{2\omega}{\pi} P \int_o^\infty \frac{ln\rho(s)}{(s^2 - \omega^2)} ds$$

Démonstration numérique En pratique, l'application de ces relations pose certaines difficultés, car la relation intégrale présente des limites allant 0 à l'infini et, naturellement, il n'est pas possible en pratique de réaliser des spectres sur une telle étendue. Il faut donc se contenter d'une intégration sur un domaine borné. Cette approche marche assez bien lorsque la fonction diélectrique de l'échantillon présente des résonances Lorentziennes localisées spectralement, mais fonctionne moins bien lorsque la fonction diélectrique diverge avec ω, ce qui est le cas si l'on modélise la permittivité d'un métal ou d'un semiconducteur fortement dopé avec un modèle de Drude. Dans tous les cas, les spectres bornés obtenus doivent être extrapolés de part et d'autre.

L'approche sur matériau décrit par un modèle de Drude a été tout d'abord testée numériquement, en simulant les spectres de réflectivité sur la plage de longueur d'onde disponible expérimentalement. Les spectres numériques ont ensuite été extrapolés à l'aide d'une somme de Lorentziennes. Figure C.2 et Figure C.3 montrent les parties réelle et imaginaire de l'indice du matériau (semiconducteur fortement dopé) déterminé via l'analyse de KK et leur valeur véritable. Un bon accord est obtenu compte tenu des limites de la méthode.

C.2.1.2. Méthode « TMM »

De même que pour un milieu semi-infini, on peut connaitre les propriétés d'une fine couche superficielle en résolvant les équations de Maxwell avec les bonnes conditions

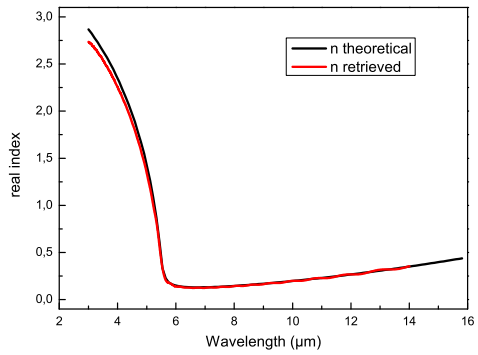

Figure C.2. : Partie réelle de l'indice de réfraction déterminé via KK et valeur vraie.

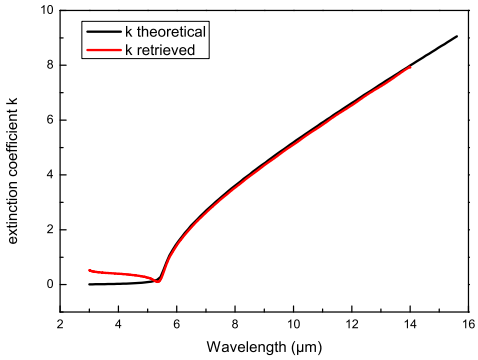

Figure C.3. : Partie imaginaire de l'indice de réfraction déterminé via KK et valeur vrai.

limites, si le substrat est bien connu (par exemple via une première analyse de KK) et que la réflectivité complexe multicouche a été déterminée. Par ailleurs, en considérant notre couche fine comme une mélange largement sub-longueur d'onde de InAsSb fortement dopé et d'air on peut, théoriquement, in fine, utiliser la théorie du milieu effectif pour récupérer la permittivité des nanostructures (qui est ici connue).

Pour déterminer la fonction diélectrique inconnue de la couche nanostructurée, le problème direct a été résolu : la réflectivité complexe du multicouche (substrat - couche structurée - superstrat) est calculée, à l'aide de la méthode des matrices de transfert (TMM pour Transfer Matrix Method), pour un ensemble d'indices complexes jusqu'à obtenir avec une bonne précision la réflectivité complexe obtenue par analyse de KK.

Démonstration Numérique Figure C.4 et Figure C.5 montrent la validité de l'approche proposée dans le cas d'une couche homogène d'InAsSb sur un substrat de GaSb.

C.2.2. Modèle « substrat effectif »

Ce modèle part de l'analyse du champ électrique non polarisé réfléchit, et prend en compte, pour le calcul de la permittivité du substrat, le caractère harmonique et anharmoniques des forces inter-atomiques. Le champ électrique réfléchi est considéré comme étant la somme de deux composantes individuelles, parallèle et perpendiculaire au plan défini par le vecteur d'onde de la lumière incidente et l'axe optique du matériau. Le coefficient de réflectivité de Fresnel se divise alors en deux composantes :

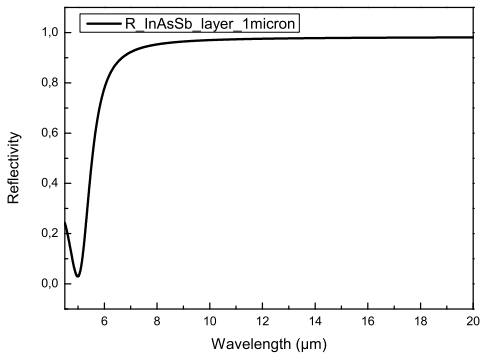

Figure C.4. : Réflectivité du système constitué d'une couche de un micron d'InAsSb sur GaSb . (numérique)

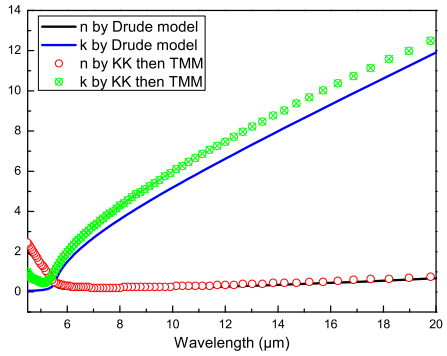

Figure C.5. : Constantes optiques déterminées via l'analyse de KK et l'utilisation de la méthode matricielle.

$$r = \frac{E_{(r,u)}}{E_i} + \frac{E_{(r,v)}}{E_i}$$

où les indices u et v représentent respectivement les composantes parallèle et perpendiculaire du champ électrique. En notant ϕ l'angle entre le champ électrique et le plan parallèle, le coefficient de Fresnel s'écrit comme $r = (\frac{E_r}{E_i})cos\phi\mathbf{u} + (\frac{E_r}{E_i})sin\phi\mathbf{v}$, et la réflectivité totale est égale à ce coefficient multiplié par son conjugué complexe :

$$R = R_u \cos^2(\phi) + R_v sin^2(\phi)$$

D'un autre côté la réflectivité dépend de la permittivité selon :

$$R_{(u,(v))} = |\frac{(\sqrt{\epsilon_{u,(v)}} - 1)}{(\sqrt{\epsilon_{u,(v)}} + 1)}|^2$$

$\epsilon_{u(v)}$ est la permittivité complexe dans le plan anisotrope (isotrope). Pour un substrat de SiC 6H, un semi-conducteur sans défauts ponctuels, il convient de prendre en considération seulement le rôle des phonons couplés avec 6 oscillateurs. La permittivité peut alors s'écrire :

$$\epsilon = \epsilon_\infty + \epsilon_1 + \epsilon_2 + \epsilon_3 + \epsilon_4 + \epsilon_5 + \epsilon_6$$

où $\epsilon(\infty)$ est la contribution des électrons fortement liées, et $\varepsilon_i(\omega)$ est décrit par un modèle d'oscillateurs de Lorentz amortis couplés (DCLO : Damped Coupled Lorentz Oscillators), où

$$\epsilon_1 = \sum_{j=1}^{6} \frac{4\pi z_1^2 + i4\pi z_1 z_j \omega \Gamma_{1,,j}/[\omega_{TO,j}^2 - \omega^2 + i\omega(\Gamma_j + \Gamma_{1,j})]}{\omega_{TO,1}^2 + \omega^2 + i\omega(\Gamma_1 + \Gamma_{1,j}) + \omega^2\Gamma_{1,j}^2/[\omega_{TO,j}^2 - \omega^2 + i\omega(\Gamma_j + \Gamma_{1,j})]}$$

et :

$$\epsilon_2 = \sum_{j=1}^{6} \frac{4\pi z_2^2 + i4\pi z_2 z_j \omega \Gamma_{2,,j}/[\omega_{TO,j}^2 - \omega^2 + i\omega(\Gamma_j + \Gamma_{2,j})]}{\omega_{TO,2}^2 + \omega^2 + i\omega(\Gamma_2 + \Gamma_{2,j}) + \omega^2 \Gamma_{2,j}^2/[\omega_{TO,j}^2 - \omega^2 + i\omega(\Gamma_j + \Gamma_{2,j})]}$$

Le paramètre S_{Tj} est la force d'oscillation de la $j^{ème}$ branche transverse optique, ω_{Tj} est sa fréquence et Γ_{Tj} son atténuation. Dans ce modèle, cette atténuation considérée auparavant comme une constante est maintenant considérée comme une fonction de la fréquence et de la température. L'atténuation tient aussi compte de l'anharmonicité. Pour cela, une méthode de perturbation de la forme cubique et quadratique de l'Hamiltonien anharmonique a été utilisé pour calculer τ_3 et τ_4 : les taux de décroissance dans les processus à trois et quatre phonons pour les différentes branches de phonon optique. Le taux d'amortissement s'écrit alors :

$$\Gamma_{(j(intrinsic))} = (C_3)_j(\tau_3^{-1})_j + (C_4)_j(\tau_4^{-1})_j$$

où C_3 et C_4 sont définis comme paramètres constants libres. En supposant une densité de Debye des états de phonons et à partir des mesures expérimentales, le taux d'amortissement total, qui inclut les défauts est :

$$\Gamma_{tot} = D\omega^{(1/2)}\Gamma_{intrinsic}^{(1/2)}$$

C.2.3. Résultat

C.2.3.1. Détection des résonances dans des caillebotis semiconducteurs fortement dopés

La Figure C.6 est une image MEB pour l'échantillon étudié, cet échantillon à été fabriqué à l'Institut d'Électronique et des Système, Universit*é* de Montpellier, dans le groupe Nanomir. La couche d'InAsSb est dopée n avec une concentration de $5 \times 10^{19}\text{cm}^{-3}$. Elle est déposée par épitaxie par jet moléculaire sur un substrat de GaSb nettement moins dopé avec du Te ($2 \times 10^{18}\text{cm}^{-3}$). Le réseau est réalisé par holographie via l'exposition d'une résine positive, suivi d'une gravure chimique réactive.

Les mesures de réflectivité IR sont obtenues par FTIR pour un angle quasi-normal.

La Figure C.7 montre la permittivité complexe *effective*, obtenues par application de relations de KK et de la méthode TMM. La permittivité complexe obtenues permet d'expliquer avec une bonne précision le spectre complexe expérimentalement déterminé. La Figure C.8 montre la réflectivité mesurée et la réflectivité retrouvée à l'aide de la permittivité complexe. Ces résultats sont discutés au sein du manuscrit dans le contexte de résonances quasi-Lorentziennes observées dans des échantillons

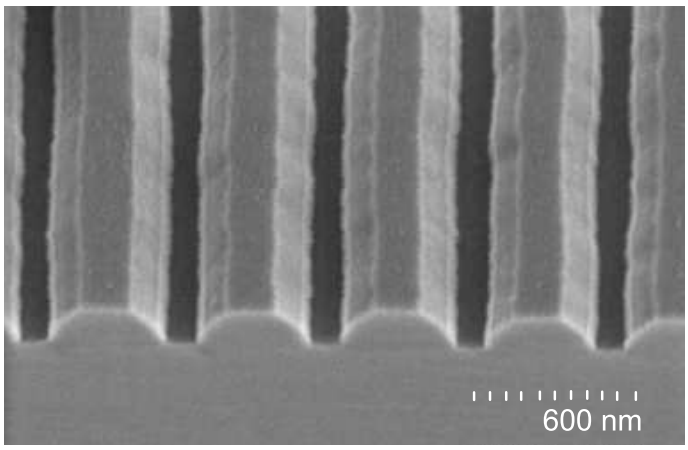

Figure C.6. : Image MEB de l'échantillon d'InAsSb étudié. La forme obtenue est trapézoïdale avec une base de 420 nm, une hauteur de 140 nm environ et une largeur au sommet d'environ 120 nm. La période est de 520 nm.

présentant des résonances de type plasmoniques ou phononiques. Nous démontrons ainsi que la permittivité effective de modes SPR et dans des cas particuliers, certains modes LSPR, peut s'écrire comme une Lorentzienne de type phononique, dont il est possible de déterminer les fréquences optiques de résonance, transverse et longitudinale, ainsi que la force d'oscillateur et l'atténuation.

Les erreurs résiduelles observées expérimentalement sont principalement attribuées aux imprécisions inhérentes à la méthode dans le cas d'un spectre borné.

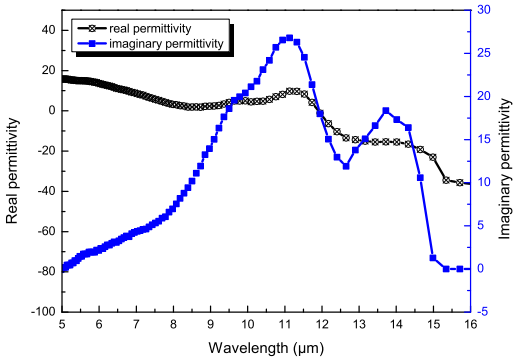

Figure C.7. : Parties réelle et imaginaires de la fonction diélectrique effective de la couche nanostructurée.

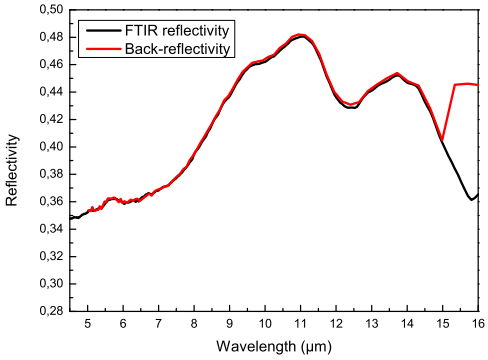

Figure C.8. : Réflectivité initiale (FTIR) et réflectivité reconstruite à partir de la permittivité complexe effective.

Pour déterminer précisément les fréquences effectives de résonance de ces quasi-Lorentziennes, nous traçons, à partir de la permittivité complexe effective, les fonc-

tions de pertes d'énergies dites « transverse optique » TO, et « longitudinale optique » LO sur la Figure C.9.

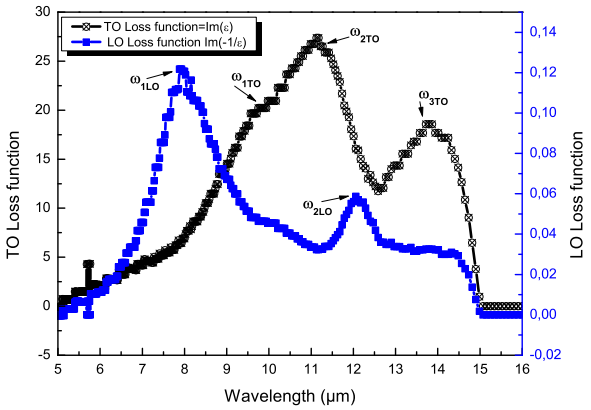

Figure C.9. : Fonctions de perte d'énergie TO et LO pour l'échantillon considéré. On obtient : $\omega_{1TO} \approx 9.7\mu$m, $\omega_{2TO} \approx 11.1\mu$m, et $\omega_{3TO} \approx 13.8\mu$m; et pour les fréquences longitudinales $\omega_{1LO} \approx 7.9\mu$m et $\omega_{2LO} \approx 12\mu$m.

On note l'existence de *plusieurs* résonances marquées, ce qui n'est pas le cas pour une structure rectangulaire non trapézoïdale (levée de dégénérescence liée à la réduction de symétrie).

C.2.4. Cas du SiC nanostructuré

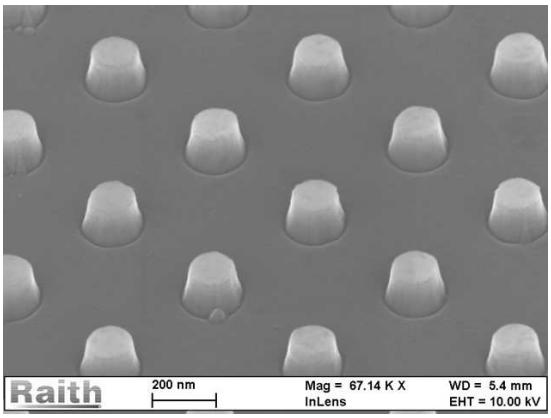

Figure C.10. : Image MEB des nanostructures de SiC sur SiC.

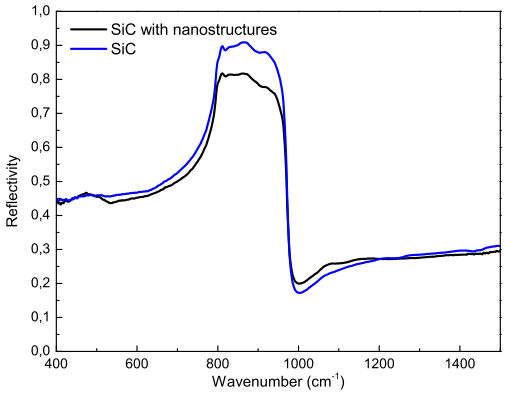

Figure C.11. : Mesure de réflectivité quasi-normale sur le SiC nanostructuré.

La Figure C.10 montre les structures de SiC fabriquées à l'UTT, par S. Kostcheev,

présentant des diamètres allant de 70 à 100 nm. Pour ce type de structure, la méthode TMM s'est révélée inopérante. La raison invoquée est que la structuration doit modifier la réponse du substrat qui alors n'est plus connue. La méthode « substrat effectif » est donc utilisée afin de déterminer, à l'aide d'une permittivité paramétrées par des DCLO, les modifications engendrées par ces structures et principalement la réduction du temps de vie des phonons.

Les spectres FTIR pour le substrat intact et le substrat structuré sont représentés sur la Figure C.11. La différence ne peut être expliquée par l'existence d'ordres de diffraction compte tenu de la nature largement sub-longueur d'onde de ces réseaux. Les composantes isotrope et anisotrope de la permittivité ϵ sont déterminées pour ces deux échantillon selon :

$$\epsilon = \epsilon_{\text{iso}} \cos\phi + \epsilon_{\text{aniso}} \sin\phi$$

Où ϵ_{iso} et ϵ_{aniso} sont modélisées par une somme de six DCLO comprenant chacun une fréquence de résonance (connue pour ce matériau mais laissée légèrement ajustable), une force d'oscillateur, et deux coefficients d'amortissement pour le processus à 3 et 4 phonons. L'angle ϕ entre le champ électrique totale et le plan anisotropique est librement ajustable.

Ces paramètres sont ajustés pour rendre compte de la réflectivité complexe. Les figures (Figure C.12 et Figure C.13) montrent les résultats obtenus, pour le SiC nu et nanostructuré. Les points expérimentaux (symboles) correspondant aux parties réelles et imaginaires sont donc « fittés » simultanément par la partie réelle et imaginaire de ϵ ainsi décrite par des DCLO (lignes pleines).

Les DCLO les plus intenses correspondent aux modes phononiques résonant à 805 cm^{-1} et 820 cm^{-1} pour la permittivité extraordinaire et résonant à 800 cm^{-1} pour la permittivité ordinaire ($\perp$). Le meilleur fit est affecté de façon déterminante par le processus à 3 phonons, montrant qu'il s'agit, à température ambiante, du mécanisme dominant pour le temps de vie. En revanche les fréquences d'oscillateurs ne sont pas affectées.

Une différence remarquable entre les permittivités est observée, due à l'introduction des nanostructures qui impactent largement le coefficient d'amortissement des phonons. La Figure C.14 compare ces coefficients pour les deux échantillons en fonction de la fréquence. L'amortissement est augmenté d'un facteur allant de 6 à un ordre de grandeur et principalement pour les hautes fréquences. Comme les deux échantillons proviennent de la même couche épitaxiale, nous pouvons logiquement attribuer l'augmentation du taux de diffusion à des collisions entre les phonons de surface et les nano-structures. En d'autre termes, les nanostructures engendrent des résonances locales qui se couplent (s'hybrident) avec les dispersions phononiques du substrat. Se couplage augmente drastiquement le taux de diffusion par l'augmentation des canaux de désintégration phononiques. En conséquence, la conductivité thermique du matériau doit s'en trouver notablement diminuée. La figure de mé-

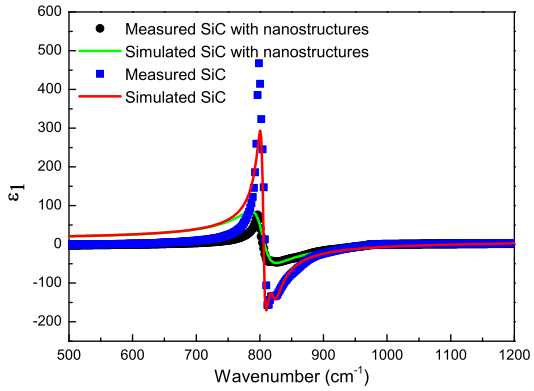

Figure C.12. : Partie réelle de la fonction diélectrique pour le SiC (bleu), et le SiC nanostructuré (noir). Les symboles correspondent au mesures, les lignes pleines aux fits.

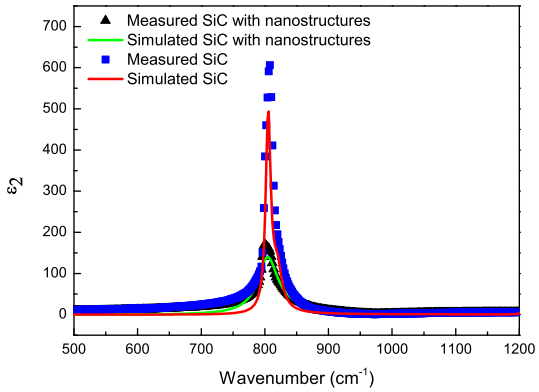

Figure C.13. : Partie imaginaire de la fonction diélectrique pour le SiC (bleu), et le SiC nanostructuré (noir). Les symboles correspondent au mesures, les lignes pleines aux fits.

rite thermoélectrique ZT, doit être augmentée dans la mesure où la conductivité électrique n'est pas, quand à elle, raisonnablement affectée par ces processus.

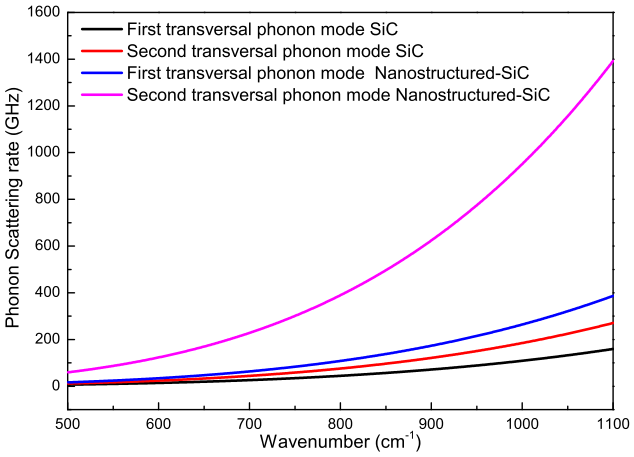

Figure C.14. : Spectre du taux de diffusion phononique calculé à partir du fit expérimental.

C.3. Caractérisation champ proche et analyse

De même qu'en champ lointain, une analyse fine en champ proche requiert généralement une mesure en amplitude et en phase. L'analyse par KK ne peut pas dans

ce cas être appliquée de la même manière pour déterminer la phase du signal. A ce jour, le microscope de champ proche optique (NSOM) ne permet pas, de toute façons, de réaliser des spectres aussi larges que ceux fournit à travers les lampes blanches des FTIR. Pour déterminer la phase du signal champ proche, le NSOM est donc placé dans un interféromètre et des sources cohérentes, accordables sont utilisées pour réaliser des études spectroscopiques.

Au cours de cette thèse, nous avons mis en œuvre une technique novatrice pour extraire de façon simple et optimale l'amplitude et la phase lorsque des modulateurs de phase relativement arbitraires sont utilisés. Cette approche est décrite pour partie ci-après. Elle est ensuite appliquée à la mesure d'échantillon tests et de l'échantillon présentant des résonances plasmoniques (réseau d'InAsSb fortement dopés).

C.3.1. Modèle Développé

Nous détaillons ici la méthode de détection interférométrique mise en place. Une telle détection interférométrique est fondamentale pour trois raisons : (i) amplifier le très faible signal issu de la sonde, (ii) éliminer les effets indésirables d'un champ électromagnétique parasite (lié à la diffusion de l'échantillon), dit "background", (iii) obtenir une information de phase mettant plus facilement en évidence les résonances phononiques, et leur éventuelles modifications.
Le NSOM est placé dans un interféromètre de Michelson, dans le bras "signal". Ce signal interfère avec un faisceau de référence, directement réfléchit sur un miroir , le signal détecté est :

$$I_{det} \propto < E_s(t) + E_R(t) >^2$$

où $E_s(t) = \sqrt{2}E_s\cos(\omega t + \phi_s)$, est le signal recherché avec E_s et ϕ_s inconnus, et $E_R(t) = \sqrt{2}E_R\cos(\omega t + \phi_R)$ est la référence d'amplitude constante et dont la phase est modulée périodiquement en fonction de temps.

Dans une première procédure expérimentale mise en place, nous excitons le miroir par un signal en dent de scie. La modulation de phase peut alors considérée comme linéaire, pour une amplitude de 2π. La valeur moyenne vu par le détecteur sur une période de temps suffisante s'écrit :

$$I_{\text{det}} \propto E_s^2 + E_R^2 + 2E_sE_R\cos(\phi_s - \phi_R)$$

La phase ϕ_R de la référence varie à une vitesse beaucoup plus grandes que celle de ϕ_s et E_s, par conséquent l'intensité détectée se décompose en deux termes : une constante I_o et un terme modulé :

$$I_{\text{mod}} = 2E_sE_R[\cos(\phi_s)\cos(\phi_R) + \sin(\phi_s)\sin(\phi_R)]$$

Une méthode idéale pour obtenir amplitude et phase, en cas de très faible signal, est alors d'utiliser une détection synchrone, dont les deux sorties X et Y donnent :

$$X_{\Omega}(I_{\text{det}}) = \frac{1}{\Omega t_{int}} \int I_{\text{det}} \cos(\Omega t)\, d(\Omega t) = E_s E_R \cos(\phi_s)$$
$$Y_{\Omega}(I_{\text{det}}) = \frac{1}{\Omega t_{int}} \int I_{\text{det}} \sin(\Omega t)\, d(\Omega t) = E_s E_R \sin(\phi_s)$$

Avec t_{int}, le temps d'intégration et $\phi_R = \Omega t$ la modulation de phase de la référence. En pratique, nous tenons compte aussi d'une modulation de signal liée à l'oscillation de la nano-sonde diffusante (asservie en mode contact intermittent avec la surface). En prenant en compte cette oscillation de pointe, des images NSOM sont alors obtenues.

Afin d'améliorer le signal obtenu et d'augmenter la vitesse d'acquisition, une seconde technique interférométrique, plus évoluée, a donc été mise en place. Nous utilisons alors typiquement un signal sinusoïdal pour exciter le miroir de référence beaucoup plus rapidement qu'une modulation en dent de scie[1]. Donc $\phi_R = a \sin(\Omega t)$, où "a" est l'amplitude de modulation. Mais dans ce cas, nous ne pouvons plus utiliser directement une détection synchrone qui ne fonctionne que pour des modulations de phase linéaires. Pour y remédier, nous avons développé une détection synchrone modifiée, réalisée sous LabVIEW via une carte d'acquisition performante (22bits). Dans ce cas, le signal est multiplié par deux références orthogonales ayant directement le même ensemble de fréquences harmoniques que celle générées par la référence, nommément $\cos(\phi_R)$ et $\sin(\phi_R)$.

Dans le cas de notre modulation sinusoïdale $\phi_R = a \sin(\Omega t)$, les deux intégrales :

$$X_{\Omega}(I_{\text{det}}) = \frac{1}{\Omega t_{int}} \int I_{\text{det}} \cos(\phi_R)\, d(\Omega t)$$
$$Y_{\Omega}(I_{\text{det}}) = \frac{1}{\Omega t_{int}} \int I_{\text{det}} \sin(\phi_R)\, d(\Omega t)$$

calculées numériquement sous LabVIEW ont des solutions analytiques obtenues grâce à la représentation intégrale des fonctions de Bessel. En négligeant pour l'instant la contribution de l'intensité I_o terme constant, c'est à dire en considérant qu'il peut être soustrait, nous avons :

$$X_{a\sin(\Omega t)}(I_{\text{mod}}) = E_s E_R (1 + J_o(2a)) \cos(\phi_s)$$
$$Y_{a\sin(\Omega t)}(I_{\text{mod}}) = E_s E_R (1 + J_o(2a)) \sin(\phi_s)$$

à partir de ces expressions, amplitude et phase sont déterminées directement. En prenant à nouveau en compte l'effet de la modulation lié à la vibration de la pointe (ce qui modifie légèrement les équations), on arrive de la même manière à déterminer amplitude et phase, tout en supprimant l'effet d'un éventuel champ parasite

[1] Et surtout sans le bruit associé à une modulation en dent de scie qui est liée au temps de "retour" du miroir de référence, en bout de course.

(background). L'approche complète est détaillée dans la section 3 de ce manuscrit avec des exemples de réalisations simples (mesure de déplacement, mesure spectroscopique résolue en phase). La technique, par la suite, est citée via son acronyme anglais G-LIA pour Generalized Lock-In Amplifier.

C.3.2. Étude d'échantillons

Nous présentons ici l'implémentation de la méthode décrite ci-dessus au sein d'un microscope de champ proche optique à sonde diffusante fonctionnant dans l'infrarouge moyen grâce à l'utilisation d'optiques achromatiques et d'un laser à cascade quantique accordable entre 10 et 10.5 μm. Dans le manuscrit, le dispositif complet est détaillé dans le second chapitre de la partie III.

Comme mentionné, la technique est testée d'abord sur des échantillons « tests » avant d'être employée sur l'échantillon plasmonique étudié précédemment en champ lointain.

C.3.2.1. Premier échantillon test : réseau Cu/Si

La Figure C.15(b), représente des images NSOM réalisées sur un échantillon sub-longueur d'onde de cuivre et de silicium issu de STMicroelectronics. La méthode G-LIA permet de mesure simultanément l'amplitude et la phase du champ, ici à l'aide d'un miroir pouvant vibrer à jusqu'à des fréquences de l'ordre de 1kHz.

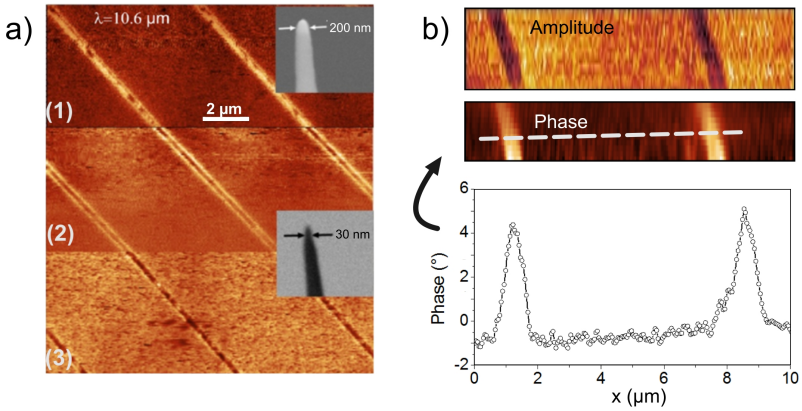

Figure C.15. : Cartographie NSOM autour de $\lambda = 10\mu m$ sur un échantillon sub-λ de fines tranchées de cuivre dans du silicium, pour différentes tailles de sondes (a) La méthode G-LIA permet d'extraire amplitude et phase.

L'analyse de cet échantillon est détaillé dans le travail de thèse de Z. Sedaghat [114]. Une inversion de contraste est observée pour des pointes très fines, ce qui peut s'expliquer par une polarisabilité de sonde particulièrement élevée mais aussi par la sensibilité accrue à l'éventuelle fine couche d'oxyde en surface du cuivre[2].

[2]Les sondes fines sont plus sensibles aux couches superficielles

Notre approche a permis d'obtenir les même contrastes avec l'obtention de la phase de manière plus simple et optimum.

C.3.2.2. Second échantillon : réseau or / polymère

Ici des lignes de polymère ont été réalisées, à l'UTT, sur une couche d'or relativement épaisse. Ces lignes sont réalisées par l'exposition d'une résine positive à l'aide de deux faisceaux. L'intérêt de la résine considérée est de présenter un indice de réfraction très proche de 1 dans notre domaine spectral d'analyse. En conséquence l'échantillon peut être correctement modélisé comme étant constitué d'une simple interface or/air. En revanche, le polymère permet d'enregistrer le signal NSOM pour différentes distances sonde-échantillon de manière reproductible et contrôlée sans dégrader la sonde, comme cela peut être le cas si l'on procède à des courbes « approche-retrait ». Ce type d'approche nous semble donc intéressante pour « calibrer » la réponse d'une pointe sans l'endommager, avant l'expérience proprement dite. Une telle calibration a ainsi été testée dans ce travail à partir de profils NSOM résolus en amplitude et en phase tels que ceux représentés sur la Figure C.16. Cette approche que nous ne reprenons pas dans ce résumé, est détaillée dans le dernier chapitre du manuscrit. Elle permet de déterminer une polarisabilité effective *complexe* pour la sonde NSOM employée, grâce au fait que le champ complexe est déterminé.

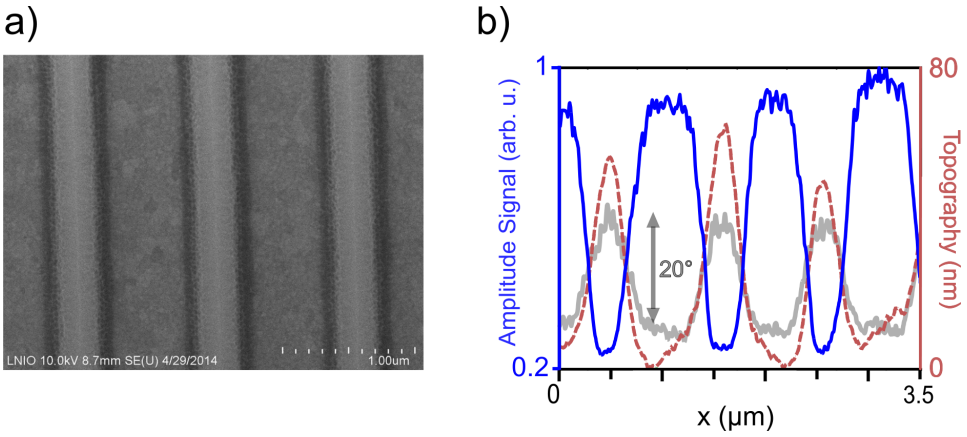

Figure C.16. : Réseau polymère/or étudié (image MEB) et profil de champ complexe obtenu par NSOM et G-LIA. Le signal varie de manière reproductible en fonction de la topographie.

C.3.2.3. Echantillon semiconducteur fortement dopé

Les réseaux d'InAsSb fortement dopés ont été imagés à l'aide la technique NSOM+G-LIA et les images obtenues on pu être comparées à des simulations électromagnétiques. La forme exacte de la structure est déterminée à partir des profils topographiques AFM au cours de mesures NSOM.

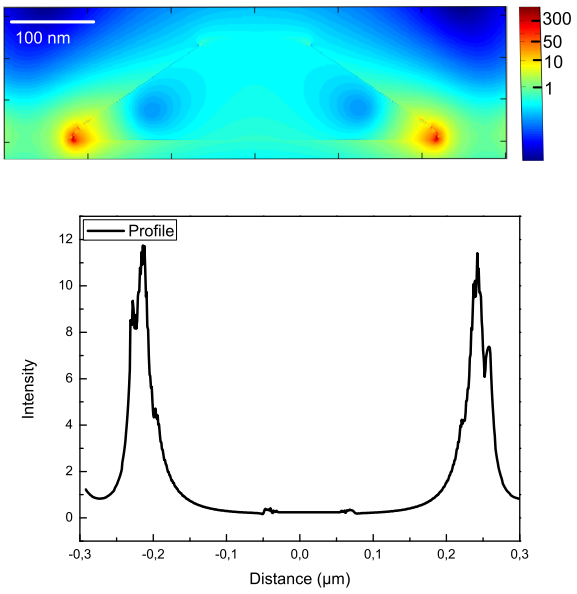

Figure C.17. : Cartographie du champ diffusé par la structure à la résonance et profil d'intensité le long des pointillés (représentant le parcours idéal de la pointe NSOM)

La Figure C.17 présente une simulation électromagnétique (FDTD) de l'intensité diffusée par la structure pour une longueur d'onde correspondant à la résonance plasmonique étudiée. Comme on peut le voir, l'intensité du champ est piquée au niveau des coins inférieurs à proximité du substrat haut indice qui tend à confiner le champ.

Idéalement, le microscope peut déterminer le profil de champ en surface de ces structures. La Figure C.17 représente le profil d'intensité le long du parcours de la sonde (en pointillé). En pratique cependant, l'interaction sonde-échantillon modifie nécessairement ce profil idéal que produirait une sonde complètement passive. Une description de l'interaction sonde-échantillon est rapportée en annexe de ce manuscrit.

La Figure C.18 représente une image NSOM expérimentale, résolue en phase et déterminée au maximum de signal vers 10.4μm, le profile (d'amplitude) diffère sensiblement de celui obtenu par des simulations ne prenant aucun compte de la sonde. Des profils similaires ont pu être enregistrés à différentes longueurs d'ondes autours de cette résonance avec des contrastes plus faibles.

Outre l'approche analytique simplifiée d'un dipôle diffusant, un modèle plus poussé couplant FDTD et fonction de Green Dyadique est suggéré et amorcé pour rendre

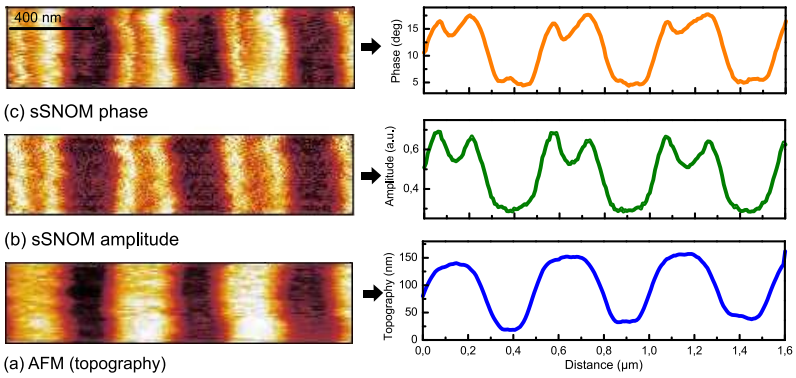

Figure C.18. : (a) Topographie, (b) Amplitude du signal s-NSOM (c) Phase du signal s-NSOM. Les profils correspondant sont indiqués à droite de l'image.

compte des résultats expérimentaux et déterminer des informations quantitatives sur la distribution du champ et la détermination des facteurs d'exaltation locaux.

Bibliography

[1] Ernst Abbe. Beiträge zur theorie des mikroskops und der mikroskopischen wahrnehmung. *Archiv für mikroskopische Anatomie*, 9(1):413–418, 1873.

[2] Sadao Adachi. Model dielectric constants of gap, gaas, gasb, inp, inas, and insb. *Physical review B*, 35(14):7454, 1987.

[3] A Al Mohtar, A Bruyant, S Kostcheev, J Vaillant, A Khoury, and M Kazan. Measurement of phonon damping by nanostructures. In *IOP Conference Series: Materials Science and Engineering*, volume 68, page 012001. IOP Publishing, 2014.

[4] A Al Mohtar, J Vaillant, Z Sedaghat, M Kazan, L Joly, C Stoeffler, J Cousin, A Khoury, and A Bruyant. Generalized lock-in detection for interferometry: application to phase sensitive spectroscopy and near-field nanoscopy. *Optics express*, 22(18):22232–22245, 2014.

[5] S Amarie and F Keilmann. Broadband-infrared assessment of phonon resonance in scattering-type near-field microscopy. *Physical Review B*, 83(4):045404, 2011.

[6] Mark S Anderson. Enhanced infrared absorption with dielectric nanoparticles. *Applied physics letters*, 83(14):2964–2966, 2003.

[7] Mark S Anderson. Surface enhanced infrared absorption by coupling phonon and plasma resonance. *Applied Physics Letters*, 87(14):144102, 2005.

[8] Jeffrey N Anker, W Paige Hall, Olga Lyandres, Nilam C Shah, Jing Zhao, and Richard P Van Duyne. Biosensing with plasmonic nanosensors. *Nature materials*, 7(6):442–453, 2008.

[9] Jeffrey N Anker, W Paige Hall, Olga Lyandres, Nilam C Shah, Jing Zhao, and Richard P Van Duyne. Biosensing with plasmonic nanosensors. *Nature materials*, 7(6):442–453, 2008.

[10] Aniello Apuzzo, Mickael Février, Rafael Salas-Montiel, Aurélien Bruyant, Alexei Chelnokov, Gilles Lérondel, Béatrice Dagens, and Sylvain Blaize. Observation of near-field dipolar interactions involved in a metal nanoparticle chain waveguide. *Nano letters*, 13(3):1000–1006, 2013.

[11] Laurent Arnaud, Aurélien Bruyant, Mikael Renault, Yassine Hadjar, Rafael Salas-Montiel, Aniello Apuzzo, Gilles Lérondel, Alain Morand, Pierre Benech, Etienne Le Coarer, et al. Waveguide-coupled nanowire as an optical antenna. *JOSA A*, 30(11):2347–2355, 2013.

[12] EA Ash and G Nicholls. *Super-resolution aperture scanning microscope*. Nature Publishing Group, 1972.

[13] Neil W Ashcroft and N David Mermin. Solid state physics (holt, rinehart and winston, new york, 1976). *There is no corresponding record for this reference*, 2005.

[14] R Bachelot, G Wurtz, and P Royer. An application of the apertureless scanning near-field optical microscopy: Imaging a gaalas laser diode in operation. *Applied physics letters*, 73(23):3333–3335, 1998.

[15] Renaud Bachelot, Gilles Lerondel, Sylvain Blaize, Sebastien Aubert, Aurelien Bruyant, and Pascal Royer. Probing photonic and optoelectronic structures by apertureless scanning near-field optical microscopy. *Microscopy research and technique*, 64(5-6):441–452, 2004.

[16] A. S. Barker and J. J. Hopfield. Coupled-optical-phonon-mode theory of the infrared dispersion in batio$_3$, srtio$_3$, and ktao$_3$. *Phys. Rev.*, 135:A1732–A1737, Sep 1964.

[17] William L Barnes. Surface plasmon–polariton length scales: a route to sub-wavelength optics. *Journal of optics A: pure and applied optics*, 8(4):S87, 2006.

[18] William L Barnes, Alain Dereux, and Thomas W Ebbesen. Surface plasmon subwavelength optics. *Nature*, 424(6950):824–830, 2003.

[19] E Betzig, M Isaacson, and A Lewis. Collection mode near-field scanning optical microscopy. *Applied physics letters*, 51(25):2088–2090, 1987.

[20] Eric Betzig and Jay K. Trautman. Near-field optics: Microscopy, spectroscopy, and surface modification beyond the diffraction limit. *Science*, 257(5067):189–195, 1992.

[21] Gerd Binnig, Calvin F Quate, and Ch Gerber. Atomic force microscope. *Physical review letters*, 56(9):930, 1986.

[22] Gerd Binnig, Heinrich Rohrer, Ch Gerber, and E Weibel. Surface studies by scanning tunneling microscopy. *Physical review letters*, 49(1):57, 1982.

[23] Amy E Bjerke and Peter R Griffiths. Surface-enhanced infrared absorption spectroscopy of< i> p</i>-nitrothiophenol on vapor-deposited platinum films. *Applied spectroscopy*, 56(10):1275–1280, 2002.

[24] Craig F Bohren and Donald R Huffman. *Absorption and scattering of light by small particles*. John Wiley & Sons, 2008.

[25] Craig F Bohren and Donald R Huffman. *Absorption and scattering of light by small particles*. John Wiley & Sons, 2008.

[26] Sergey I Bozhevolnyi, Valentyn S Volkov, Eloise Devaux, Jean-Yves Laluet, and Thomas W Ebbesen. Channel plasmon subwavelength waveguide components including interferometers and ring resonators. *Nature*, 440(7083):508–511, 2006.

[27] A. Bruyant. *Etude de structures photoniques en champ proche par microscopie optique á sonde diffusante*. PhD thesis, University of Technology of Troyes, Troyes, France, 2004.

[28] D Michael Byler and Heino Susi. Examination of the secondary structure of proteins by deconvolved ftir spectra. *Biopolymers*, 25(3):469–487, 1986.

[29] Nicolas Chateau and Jean-Paul Hugonin. Algorithm for the rigorous coupled-wave analysis of grating diffraction. *JOSA A*, 11(4):1321–1331, 1994.

[30] Yiguo Chen, Yan Francescato, Joshua D Caldwell, Vincenzo Giannini, Tobias WW Maß, Orest J Glembocki, Francisco J Bezares, Thomas Taubner, Richard Kasica, Minghui Hong, et al. Spectral tuning of localized surface phonon polariton resonators for low-loss mid-ir applications. *ACS Photonics*, 1(8):718–724, 2014.

[31] Tuck C Choy. Effective medium theory. 1999.

[32] A. T. Collins, E. C. Lightowlers, and P. J. Dean. Lattice vibration spectra of aluminum nitride. *Phys. Rev.*, 158:833–838, 1967.

[33] G. Conforti, M. Brenci, A. Mencaglia, and A. G. Mignani. Fiber optic vibration sensor for remote monitoring in high power electric machines. *Appl. Opt.*, 28(23):5158–5161, Dec 1989.

[34] Bruce L Davis and Mahmoud I Hussein. Nanophononic metamaterial: Thermal conductivity reduction by local resonance. *Physical review letters*, 112(5):055505, 2014.

[35] R. Debdulal, S.H. Leong, and M.E. Welland. Dielectric contrast imaging using apertureless scanning near-field optical microscopy in the reflection mode. *Journal of the Korean Physical Society*, 47(2):140–146, August 2005.

[36] Nicholas E Dickenson, Kevin P Armendariz, Heath A Huckabay, Philip W Livanec, and Robert C Dunn. Near-field scanning optical microscopy: a tool for nanometric exploration of biological membranes. *Analytical and bioanalytical chemistry*, 396(1):31–43, 2010.

[37] JA Dionne, LA Sweatlock, HA Atwater, and A Polman. Planar metal plasmon waveguides: frequency-dependent dispersion, propagation, localization, and loss beyond the free electron model. *Physical Review B*, 72(7):075405, 2005.

[38] T. W. Ebbesen, H. J. Lezec, H. F. Ghaemi, T. Thio, and P. A. Wolff. Extraordinary optical transmission through sub-wavelength hole arrays. *Nature*, 391:667–669, 1998.

[39] C. Elliott, V. Vijayakumar, W. Zink, and R. Hansen. National instruments labview: A programming environment for laboratory automation and measurement, 2007.

[40] Nicholas Fang, Hyesog Lee, Cheng Sun, and Xiang Zhang. Sub–diffraction-limited optical imaging with a silver superlens. *Science*, 308(5721):534–537, 2005.

[41] M. Fleischer. Near-field scanning optical microscopy nanoprobes. *Nanotechnology Reviews*, 1(4):299–386, 2012.

[42] Herbert Fröhlich. *Theory of dielectrics*. Clarendon Press, 1949.

[43] François Gervais and Bernard Piriou. Temperature dependence of transverse- and longitudinal-optic modes in ti o 2 (rutile). *Physical Review B*, 10(4):1642, 1974.

[44] Bare GH., Alben JO., and Bromberg PA. Sulfhydryl groups in hemoglobin. a new molecular probe at the alpha1 beta 1 interface studied by fourier transform infrared spectroscopy. *Biochemistry*, 14(8):1578–1583, 1975.

[45] Omicron Nanotechnology GmbH. www.omicron-instruments.com, 2007. Taunusstein, Germany.

[46] Witec GmbH. www.witec.de, 2007. Ulm, Germany.

[47] Jean-Jacques Greffet, Rémi Carminati, Karl Joulain, Jean-Philippe Mulet, Stéphane Mainguy, and Yong Chen. Coherent emission of light by thermal sources. *Nature*, 416(6876):61–64, 2002.

[48] VN'Tsame Guilengui, L Cerutti, J-B Rodriguez, E Tournié, and T Taliercio. Localized surface plasmon resonances in highly doped semiconductors nanostructures. *Applied Physics Letters*, 101(16):161113, 2012.

[49] Atwater H. The promise of plasmonics. Scientific American, 2007.

[50] Susan C Hagness and Allen Taflove. Computational electrodynamics: The finite-difference time-domain method. *Norwood, MA: Artech House*, 2000.

[51] OS Heavens. Optical properties of thin films. *Reports on Progress in Physics*, 23(1):1, 1960.

[52] Bielefeldt Hecht, H Bielefeldt, Y Inouye, DW Pohl, and L Novotny. Facts and artifacts in near-field optical microscopy. *Journal of Applied Physics*, 81(6):2492–2498, 1997.

[53] R. Hillenbrand and F. Keilmann. Complex optical constants on a subwavelength scale. *Phys. Rev. Lett.*, 85:3029–3032, Oct 2000.

[54] R. HillenbRand, B. Knoll, and F. Keilmann. Pure optical contrast in scattering-type scanning near-field microscopy. *Journal of Microscopy*, 202(1):77–83, 2001.

[55] R Hillenbrand, T Taubner, and F Keilmann. Phonon-enhanced light–matter interaction at the nanometre scale. *Nature*, 418(6894):159–162, 2002.

[56] Paul S. Ho and Arthur L. Ruoff. Pressure dependence of the elastic constants for aluminum from 77 ^{o}k; to 300 ^{o}k. *Journal of Applied Physics*, 40(8):3151–3156, Jul 1969.

[57] N Hosaka and T Saiki. Near-field fluorescence imaging of single molecules with a resolution in the range of 10 nm. *Journal of microscopy*, 202(2):362–364, 2001.

[58] Yasushi Inouye and Satoshi Kawata. Near-field scanning optical microscope with a metallic probe tip. *Optics letters*, 19(3):159–161, 1994.

[59] D.A. Jackson, A.D. Kersey, M. Corke, and J.D.C. Jones. Pseudoheterodyne detection scheme for optical interferometers. *Electronics Letters*, 18:1081–1083(2), December 1982.

[60] John David Jackson and John D Jackson. *Classical electrodynamics*, volume 3. Wiley New York etc., 1962.

[61] H. O. Jacobs, P. Leuchtmann, O. J. Homan, and A. Stemmer. Resolution and contrast in kelvin probe force microscopy. *Journal of Applied Physics*, 84(3):1168–1173, 1998.

[62] JR Jasperse, A Kahan, JN Plendl, and SS Mitra. Temperature dependence of infrared dispersion in ionic crystals lif and mgo. *Physical Review*, 146(2):526, 1966.

[63] M Kazan, A Bruyant, Z Sedaghat, L Arnaud, S Blaize, and P Royer. Temperature and directional dependences of the infrared dielectric function of free standing silicon nanowire. *physica status solidi (c)*, 8(3):1006–1011, 2011.

[64] M Kazan, G Guisbiers, S Pereira, MR Correia, P Masri, A Bruyant, S Volz, and P Royer. Thermal conductivity of silicon bulk and nanowires: Effects of isotopic composition, phonon confinement, and surface roughness. *Journal of Applied Physics*, 107(8):083503, 2010.

[65] M Kazan, L Ottaviani, E Moussaed, R Nader, and P Masri. Effect of introducing gettering sites and subsequent au diffusion on the thermal conductivity and the free carrier concentration in n-type 4h-sic. *Journal of Applied Physics*, 103(5):053707, 2008.

[66] M Kazan, S Pereira, J Coutinho, MR Correia, and P Masri. Role of optical phonon in ge thermal conductivity. *Applied Physics Letters*, 92(21):211903–211903, 2008.

[67] M. Kazan and S. Volz. Calculation of the lattice thermal conductivity in granular crystals. *Journal of Applied Physics*, 115(7), 2014.

[68] F. Keilmann. Surface-polariton propagation for scanning near-field optical microscopy application. *Journal of Microscopy*, 194(2–3):567–570, 1999.

[69] Ole Keller, Mufei Xiao, and Sergey Bozhevolnyi. Configurational resonances in optical near-field microscopy: a rigorous point-dipole approach. *Surface science*, 280(1):217–230, 1993.

[70] AD Kersey, AC Lewin, and DA Jackson. Pseudo-heterodyne detection scheme for the fibre gyroscope. *Electronics Letters*, 20(9):368–370, 1984.

[71] Charles Kittel and Donald F Holcomb. Introduction to solid state physics. *American Journal of Physics*, 35(6):547–548, 1967.

[72] Katrin Kneipp, Yang Wang, Harald Kneipp, Lev T Perelman, Irving Itzkan, Ramachandra R Dasari, and Michael S Feld. Single molecule detection using surface-enhanced raman scattering (sers). *Physical review letters*, 78(9):1667, 1997.

[73] Bernhard Knoll and Fritz Keilmann. Enhanced dielectric contrast in scattering-type scanning near-field optical microscopy. *Optics Communications*, 182(4):321–328, 2000.

[74] M Kulawik, M Nowicki, G Thielsch, L Cramer, H-P Rust, H-J Freund, TP Pearl, and PS Weiss. A double lamellae dropoff etching procedure for tungsten tips attached to tuning fork atomic force microscopy/scanning tunneling microscopy sensors. *Review of scientific instruments*, 74(2):1027–1030, 2003.

[75] Manvir S Kushwaha, P Halevi, L Dobrzynski, and B Djafari-Rouhani. Acoustic band structure of periodic elastic composites. *Physical Review Letters*, 71(13):2022, 1993.

[76] A. Lahrech, R. Bachelot, P. Gleyzes, and A. C. Boccara. Infrared-reflection-mode near-field microscopy using an apertureless probe with a resolution of $\lambda/600$. *Opt. Lett.*, 21(17):1315–1317, Sep 1996.

[77] Surbhi Lal, Stephan Link, Halas, and Naomi J. Nano-optics from sensing to waveguiding. *Nat Photon*, 1:641–648, 2007.

[78] Rolf Landauer. Electrical conductivity in inhomogeneous media. In *Electrical transport and optical properties of inhomogeneous media*, volume 40, pages 2–45. AIP Publishing, 1978.

[79] S Law, DC Adams, AM Taylor, and D Wasserman. Mid-infrared designer metals. *Optics express*, 20(11):12155–12165, 2012.

[80] AMAA Lewis, M Isaacson, A Harootunian, and A Muray. Development of a 500 Å spatial resolution light microscope: I. light is efficiently transmitted through $\lambda/16$ diameter apertures. *Ultramicroscopy*, 13(3):227–231, 1984.

[81] Debin Li and CZ Ning. All-semiconductor active plasmonic system in mid-infrared wavelengths. *Optics express*, 19(15):14594–14603, 2011.

[82] Z-F Li, W Lu, H-J Ye, Z-H Chen, X-Z Yuan, H-F Dou, S-C Shen, G Li, and SJ Chua. Carrier concentration and mobility in gan epilayers on sapphire substrate studied by infrared reflection spectroscopy. *Journal of applied physics*, 86(5):2691–2695, 1999.

[83] Stephan Link and Mostafa A El-Sayed. Spectral properties and relaxation dynamics of surface plasmon electronic oscillations in gold and silver nanodots and nanorods. *The Journal of Physical Chemistry B*, 103(40):8410–8426, 1999.

[84] Nanonics Imaging Ltd. www.nanonics.co.il, 2007. Jerusalem, Israel.

[85] Valerio Lucarini. *Kramers-Kronig relations in optical materials research*, volume 110. Springer Science & Business Media, 2005.

[86] FDTD Lumerical. Solution, fdtd solutions 6.5.

[87] Hans Lüth. *Solid surfaces, interfaces and thin films*, volume 4. Springer, 2001.

[88] MP Madan. Anharmonic effects and thermodynamic properties of crystals. *Physica B+ C*, 124(1):35–42, 1984.

[89] N Maghelli, M Labardi, S Patanè, F Irrera, and M Allegrini. Optical near-field harmonic demodulation in apertureless microscopy. *Journal of microscopy*, 202(1):84–93, 2001.

[90] Stefan A. Maier, Pieter G. Kik, and Harry A. Atwater. Optical pulse propagation in metal nanoparticle chain waveguides. *Phys. Rev. B*, 67:205402, May 2003.

[91] Takuya Matsumoto, Tsutomu Ichimura, Takashi Yatsui, Motonobu Kourogi, Toshiharu Saiki, and Motoichi Ohtsu. Fabrication of a near-field optical fiber probe with a nanometric metallized protrusion. *Optical review*, 5(6):369–373, 1998.

[92] J. A. Matteo, D. P. Fromm, Y. Yuen, P. J. Schuck, W. E. Moerner, and L. Hesselink. Spectral analysis of strongly enhanced visible light transmission through single c-shaped nanoapertures. *Applied Physics Letters*, 85(4):648–650, 2004.

[93] M Essone Mezeme, S Lasquellec, and C Brosseau. Dielectric resonances at optical frequencies using metal nanoshells. *Journal of Physics D: Applied Physics*, 42(13):135420, 2009.

[94] Xiaoyu Miao, Benjamin K. Wilson, and Lih Y. Lin. Localized surface plasmon assisted microfluidic mixing. *Applied Physics Letters*, 92(12), 2008.

[95] Hiroshi Muramatsu, Norio Chiba, Katsunori Homma, Kunio Nakajima, Tatsuaki Ataka, Satoko Ohta, Akihiro Kusumi, and Masamichi Fujihira. Near-field optical microscopy in liquids. *Applied physics letters*, 66(24):3245–3247, 1995.

[96] Shuming Nie and Steven R Emory. Probing single molecules and single nanoparticles by surface-enhanced raman scattering. *science*, 275(5303):1102–1106, 1997.

[97] L. Novotny, D. W. Pohl, and B. Hecht. Scanning near-field optical probe with ultrasmall spot size. *Opt. Lett.*, 20(9):970–972, May 1995.

[98] Lukas Novotny and Bert Hecht. *Principles of nano-optics*. Cambridge university press, 2012.

[99] V. Ntsame Guilengui. *Technologie et étude de résonateurs plasmoniques á base d'InAsSb : vers une plasmonique tout semi-conducteur*. PhD thesis, Université Montpellier 2, 2013.

[100] N Ocelic and R Hillenbrand. Subwavelength-scale tailoring of surface phonon polaritons by focused ion-beam implantation. *Nature Materials*, 3(9):606–609, 2004.

[101] N. Ocelic, A. Huber, and R. Hillenbrand. Pseudoheterodyne detection for background-free near-field spectroscopy. *Applied Physics Letters*, 89(10), 2006.

[102] WC Overton Jr. Properties of the quartic anharmonic contribution to the specific heat of a face-centered cubic lattice. *The Journal of Chemical Physics*, 44(3):934–939, 1966.

[103] Jorge Pérez-Juste, Isabel Pastoriza-Santos, Luis M Liz-Marzán, and Paul Mulvaney. Gold nanorods: synthesis, characterization and applications. *Coordination Chemistry Reviews*, 249(17):1870–1901, 2005.

[104] Cyril Petibois. Imaging methods for elemental, chemical, molecular, and morphological analyses of single cells. *Analytical and bioanalytical chemistry*, 397(6):2051–2065, 2010.

[105] DW Pohl, W Denk, and M Lanz. Optical stethoscopy: Image recording with resolution $\lambda/20$. *Applied physics letters*, 44(7):651–653, 1984.

[106] Joyce Poon and Bruce Francis. Kramers-kronig relations for lossless media.

[107] ZV Popović, G Stanišić, D Stojanović, and R Kostić. Infrared and raman spectra of cdo. *physica status solidi (b)*, 165(2):K109–K112, 1991.

[108] Ilya P. Radko, Sergey I. Bozhevolnyi, and Niels Gregersen. Transfer function and near-field detection of evanescent waves. *Appl. Opt.*, 45(17):4054–4061, Jun 2006.

[109] N. Rahbany, M. Kazan, M. Tabbal, R. Tauk, J. Jabbour, J. Brault, B. Damilano, and J. Massies. Measurement of the effect of plasmon gas oscillation on the dielectric properties of p- and n-doped $Al_xGa_{1-x}N$ films using infrared spectroscopy. *Journal of Applied Physics*, 114(5), 2013.

[110] Maurizioand Righini, Anna S. Zelenina, Christian Girard, and Romain Quidant. Parallel and selective trapping in a patterned plasmonic landscape. *Nat Phys*, 3:477–480, 2007.

[111] Rafael Salas-Montiel, Aniello Apuzzo, Cécile Delacour, Zohreh Sedaghat, Aurélien Bruyant, Philippe Grosse, Alexei Chelnokov, Gilles Lerondel, and Sylvain Blaize. Quantitative analysis and near-field observation of strong coupling between plasmonic nanogap and silicon waveguides. *Applied Physics Letters*, 100(23):231109, 2012.

[112] Y. Sasaki and H. Sasaki. Heterodyne detection for the extraction of the probe-scattering signal in scattering-type scanning near-field optical microscope. *Japanese Journal of Applied Physics*, 39(2):321, April 2000.

[113] M Schnell, A Garcia-Etxarri, AJ Huber, K Crozier, J Aizpurua, and R Hillenbrand. Controlling the near-field oscillations of loaded plasmonic nanoantennas. *Nature Photonics*, 3(5):287–291, 2009.

[114] Z. Sedaghat. *A near-field study of the probe-sample interaction in near and mid-infrared nanoscopy*. PhD thesis, University of Technology of Troyes, Troyes, France, 2012.

[115] Zohreh Sedaghat, Aurelien Bruyant, Michel Kazan, Julien Vaillant, Sylvain Blaize, Névine Rochat, Nicolas Chevalier, Enric Garcia-Caurel, Pierre Morin, and Pascal Royer. Development of a polarization resolved mid-ir near-field microscope. In *SPIE OPTO*, pages 79461N–79461N. International Society for Optics and Photonics, 2011.

[116] Zohreh Sedaghat, Anna Rumyantseva, Aurélien Bruyant, Sergei Kostcheev, Sylvain Blaize, Safi Jradi, Renaud Bachelot, and Antoine Monmayrant. Near-field optical imaging with a nanotip grown on fibered polymer microlens. *Applied Physics Letters*, 100(3):033107, 2012.

[117] M Shamseddine, M Kazan, and M Tabbal. Model for the unpolarized infrared reflectivity from uniaxial polar materials: Effects of anisotropy, free carriers, and defects. *Infrared Physics & Technology*, 55(1):112–121, 2012.

[118] M Sigalas and EN Economou. Band structure of elastic waves in two dimensional systems. *Solid State Communications*, 86(3):141–143, 1993.

[119] JE Sipe, Jeff F Young, JS Preston, and HM Van Driel. Laser-induced periodic surface structure. i. theory. *Physical Review B*, 27(2):1141, 1983.

[120] DR Smith, S Schultz, P Markoš, and CM Soukoulis. Determination of effective permittivity and permeability of metamaterials from reflection and transmission coefficients. *Physical Review B*, 65(19):195104, 2002.

[121] Laszlo Solymar and Ekaterina Shamonina. *Waves in metamaterials*. Oxford University Press, 2009.

[122] Richard Soref, Robert E Peale, and Walter Buchwald. Longwave plasmonics on doped silicon and silicides. *Optics express*, 16(9):6507–6514, 2008.

[123] Raoul M Stöckle, Yung Doug Suh, Volker Deckert, and Renato Zenobi. Nanoscale chemical analysis by tip-enhanced raman spectroscopy. *Chemical Physics Letters*, 318(1):131–136, 2000.

[124] E.H. Synge. A suggested method for extending microscopic resolution into the ultra-microscopic region. *Philosophical Magazine Series 7*, 6(35):356–362, 1928.

[125] Allen Taflove and Susan C Hagness. *Computational electrodynamics*. Artech house, 2005.

[126] LM Thomas and J Shanker. Temperature dependence of elastic constants and thermal expansion coefficient for nacl crystals. *physica status solidi (b)*, 195(2):361–366, 1996.

[127] Valeri P Tolstoy, Irina V Chernyshova, and Valeri A Skryshevsky. *Index*. Wiley Online Library, 2003.

[128] Molecular Vista. http://www.molecularvista.com/, 2011. California, USA.

[129] Liang Wang, Sreemanth M. Uppuluri, Eric X. Jin, and Xianfan Xu. Nanolithography using high transmission nanoscale bowtie apertures. *Nano Letters*, 6(3):361–364, 2006.

[130] H. J. Weber, L. Ruby, and G. B. Arfken. *Mathematical methods for physicists*. Harcourt/Academic, 5 edition, 2000.

[131] Eric W. Weisstein. Jacobi-anger expansion. from mathworld–a wolfram web resource.

[132] John Wessel. Surface-enhanced optical microscopy. *JOSA B*, 2(9):1538–1541, 1985.

[133] Katherine A. Willets and Richard P. Van Duyne. Localized surface plasmon resonance spectroscopy and sensing. *Annual Review of Physical Chemistry*, 58(1):267–297, 2007.

[134] Katherine A Willets and Richard P Van Duyne. Localized surface plasmon resonance spectroscopy and sensing. *Annu. Rev. Phys. Chem.*, 58:267–297, 2007.

[135] C Wood. Materials for thermoelectric energy conversion. *Reports on progress in physics*, 51(4):459, 1988.

[136] Y. Yao, A.J. Hoffman, and C.F. Gmachl. Mid-infrared quantum cascade lasers. *NATURE PHOTONICS*, 6:432–439, 2012.

[137] Pochi Yeh. *Optical waves in layered media*, volume 95. Wiley New York, 1988.

[138] Anatoly V Zayats, Igor I Smolyaninov, and Alexei A Maradudin. Nano-optics of surface plasmon polaritons. *Physics reports*, 408(3):131–314, 2005.

[139] F Zenhausern, MP O'boyle, and HK Wickramasinghe. Apertureless near-field optical microscope. *Applied Physics Letters*, 65(13):1623–1625, 1994.

[140] Yin Zhiqiang and GL Harding. Optical properties of dc reactively sputtered thin films. *Thin Solid Films*, 120(2):81–108, 1984.

Abeer AL MOHTAR

Doctorat : Optique et Nanotechnologies

Année 2015

Etude de modes de surface localisés phononiques et plasmoniques par spectroscopie-IR et champ proche optique

Longtemps cantonnées au visible et au proche IR, des nanostructures résonantes sont à présent réalisées dans l'IR, notamment en vue d'applications spectroscopiques. Pour étudier la réponse de ces nanostructures des moyens de caractérisation spécifiques doivent être mise en œuvre. Nous considérons la réponse IR de nano-structures et développons des outils à même de les caractériser. Nous nous sommes intéressés à des échantillons pouvant présenter des modes localisés de surface associés à des Plasmons Polaritons au sein de semiconducteurs fortement dopés ou des Phonons Polaritons dans des matériaux semiconducteurs polaires comme SiC. Cette étude a été menée d'abord en champ lointain (Spectroscopie à Transformée de Fourier et analyse Kramers-Kronig) pour étudier la réponse collective des nanostructures. Nous montrons que la fonction diélectrique de l'échantillon structuré peut être représentée par un oscillateur de Lorentz amortit modifié. Une permittivité effective est aussi déterminée par l'emploi de matrices de transfert pour rendre compte de la réflectivité complexe. L'étude en champ proche permet ensuite d'obtenir une réponse individuelle des structures. Nous développons ici une méthode d'extraction novatrice de l'amplitude et de la phase du signal avec un rapport signal à bruit optimum. Après avoir théoriquement et expérimentalement démontré la pertinence de l'approche, la signature de SPP localisés a pu être observée par des cartographies de champ complexe en fonction de la longueur d'onde. Les images obtenues sont confrontées à des simulations électromagnétiques et discutées.

Mots clés : interféromètres - optique en champ proche - spectroscopie infrarouge – plasmons.

Localized Surface plasmon and phonon polaritons investigated by mid-infrared spectroscopy and near-field nanoscopy

We studied the response of a nano-structured material to an IR electromagnetic excitation. For a given geometry, this response is dictated by the dielectric function to which phonons and free carriers contribute. In case of defect-free semiconductors the phonon response is the dominant term; however when we consider doped semi-conductors the plasmon response plays a major role. In both case, the permittivity functions can be negative with small losses which permits a resonant coupling between the surface modes and the electromagnetic excitation. Our work focuses on the development of experimental tools to analyze both SPP and SPhP. This study was conducted in the far-field regime to see a collective response and in the near-field regime to study nano-structures individually. In far-field, the experimental spectroscopic response of the material was conducted by Fourier Transform Infrared Reflectivity and Kramers-Kronig analysis. Quantitative information on the dielectric function was extracted using a modified Lorentz damped oscillator to fit the reflectivity. An effective permittivity is also retrieved using a transfer matrix method. The near-field study was done in a two-step procedure. The first step was the development of an innovative detection technique with optimum signal to noise ratio. The second step was the implementation of this technique to NSOM after proving its success. LSPP were detected using the developed NSOM. A spectroscopic study was performed as well. Experimental results were compared to theoretical ones obtained with electromagnetic simulations.

Keywords: interferometers - near-field microscopy - infrared spectroscopy - plasmons (physics).

Thèse réalisée en partenariat entre :

Université Libanaise
École Doctorale Sciences et Technologies

utt
université de technologie
Troyes

Ecole Doctorale "Sciences et Technologies"